

Auto-calibration for efficient diesel engines with a waste heat recovery system

Citation for published version (APA):

Feru, E. (2015). *Auto-calibration for efficient diesel engines with a waste heat recovery system*. [Phd Thesis 1 (Research TU/e / Graduation TU/e), Mechanical Engineering]. Technische Universiteit Eindhoven.

Document status and date:

Published: 01/01/2015

Document Version:

Publisher's PDF, also known as Version of Record (includes final page, issue and volume numbers)

Please check the document version of this publication:

- A submitted manuscript is the version of the article upon submission and before peer-review. There can be important differences between the submitted version and the official published version of record. People interested in the research are advised to contact the author for the final version of the publication, or visit the DOI to the publisher's website.
- The final author version and the galley proof are versions of the publication after peer review.
- The final published version features the final layout of the paper including the volume, issue and page numbers.

[Link to publication](#)

General rights

Copyright and moral rights for the publications made accessible in the public portal are retained by the authors and/or other copyright owners and it is a condition of accessing publications that users recognise and abide by the legal requirements associated with these rights.

- Users may download and print one copy of any publication from the public portal for the purpose of private study or research.
- You may not further distribute the material or use it for any profit-making activity or commercial gain
- You may freely distribute the URL identifying the publication in the public portal.

If the publication is distributed under the terms of Article 25fa of the Dutch Copyright Act, indicated by the "Taverne" license above, please follow below link for the End User Agreement:

www.tue.nl/taverne

Take down policy

If you believe that this document breaches copyright please contact us at:

openaccess@tue.nl

providing details and we will investigate your claim.

Auto-calibration for Efficient Diesel Engines with a Waste Heat Recovery System



EMANUEL FERU



The research reported in this thesis is part of the research program of the Dutch Institute of Systems and Control (DISC). The author has successfully completed the educational program of the Graduate School DISC.

This research was financially supported by TNO Automotive, Helmond, The Netherlands.

A catalogue record is available from the Eindhoven University of Technology Library. ISBN: 978-90-386-3917-8

Typeset by the author with the pdf L^AT_EX documentation system.

Cover design: Emanuel Feru.

Reproduction: CPI Koninklijke Wöhrmann B.V., Zutphen, The Netherlands.

Copyright ©2015 by Emanuel Feru. All rights reserved.

PROEFSCHRIFT

ter verkrijging van de graad van doctor aan de
Technische Universiteit Eindhoven, op gezag van de
rector magnificus, prof.dr.ir. F.P.T. Baaijens, voor een
commissie aangewezen door het College voor
Promoties, in het openbaar te verdedigen
op dinsdag 29 september 2015 om 16.00 uur

door

Emanuel Feru

geboren te Onești, Roemenië

Dit proefschrift is goedgekeurd door de promotoren en de samenstelling van de promotiecommissie is als volgt:

voorzitter:	prof.dr. L.P.H. de Goey
promotor:	prof.dr.ir. M. Steinbuch
1 ^e copromotor:	dr.ir. F. Willems
2 ^e copromotor:	dr.ir. B. de Jager
leden:	prof.dr.ir. L. del Re (Johannes Kepler University, Austria) prof.dr.ir. D.M.J. Smeulders prof.dr.ir. Z. Filipi (Clemson University, USA)
adviseur:	dr.ir. V. Lemort (University of Liege, Belgium)

Contents

Societal summary	ix
Acronyms	xi
1 Introduction	1
1.1 Drivers & challenges for diesel trucks	1
1.2 State-of-the-art in waste heat recovery	3
1.2.1 The Rankine Cycle	4
1.3 Problem statement	7
1.3.1 Dynamic WHR system modeling	8
1.3.2 Low-level control design	10
1.3.3 Integrated powertrain control approach	12
1.3.4 System architecture	13
1.3.5 Business case	14
1.4 Outline of this thesis	14
1.5 List of publications	15
2 Two-phase plate-fin heat exchanger modeling	19
2.1 Introduction	20
2.2 System description	22
2.3 Heat exchanger modeling approach	24
2.3.1 Mass and energy conservation	25
2.3.2 Heat transfer	27
2.3.3 Non-dimensional analysis	29
2.4 Model discretization	31
2.4.1 Phase-change detection	33
2.4.2 Model verification	34
2.5 Experimental validation	37

2.6	Conclusions	45
3	Modeling and control of a parallel waste heat recovery system	47
3.1	Introduction	48
3.2	Experimental Set-Up	49
3.3	Waste Heat Recovery System Modeling	51
3.3.1	Pump	51
3.3.2	Valve	52
3.3.3	Evaporator and Condenser	53
3.3.4	Mixing Junction	55
3.3.5	Expander	56
3.3.6	Experimental Validation	57
3.4	Control Design	61
3.4.1	Control Objective	61
3.4.2	Model for Control Design	62
3.4.3	Linear Model Predictive Control	64
3.4.4	Nonlinear Model Predictive Control	65
3.5	Simulation Results and Discussion	66
3.5.1	Stepwise Cycle	67
3.5.2	World Harmonized Transient Cycle	69
3.6	Conclusions and Future Research	72
4	Control of a Waste Heat Recovery System with Decoupled Expander	73
4.1	Introduction	73
4.2	System description	75
4.3	Problem formulation	76
4.4	System analysis	78
4.5	Control design	80
4.5.1	Control objective	80
4.5.2	Switching mechanism	81
4.5.3	State estimator	82
4.5.4	Optimizer	82
4.6	Simulation results	83
4.6.1	Steady-state results	84
4.6.2	Transient results	85
4.7	Conclusions	88

5	Integrated Powertrain Control	89
5.1	Introduction	89
5.2	System description	91
5.3	Simulation model	93
5.3.1	Engine	93
5.3.2	Aftertreatment system	94
5.3.3	Waste Heat Recovery system	94
5.3.4	Electric system	96
5.4	Control model	97
5.5	Control strategy	99
5.5.1	Low-level SCR control	100
5.5.2	Low-level WHR control	100
5.5.3	Optimal IPC strategy	100
5.5.4	Real-time IPC strategy	103
5.5.5	Battery bounds	105
5.5.6	Baseline strategy	106
5.6	Simulation results	106
5.6.1	Stationary conditions	106
5.6.2	World Harmonized Transient Cycle	108
5.7	Conclusions	113
6	Discussion, conclusions and recommendations	115
6.1	Discussion	115
6.1.1	WHR system modeling	115
6.1.2	Control	116
6.2	Conclusions	117
6.3	Recommendations for future research	119
A	Fluid properties	123
A.1	Working fluid properties	123
B	Battery management	127
B.1	Rule-based battery management	127
	Summary	139
	Acknowledgements	143
	Curriculum Vitae	145

Societal summary

Auto-calibration for Efficient Diesel Engines with a Waste Heat Recovery System

With the growing needs for mobility, automotive industry is experiencing one of the greatest challenge in car history: stringent CO₂ emissions and pollutants limits on a global level. While the production of electric vehicles is growing, most of the vehicles still rely on internal combustion engines. These engines have low efficiencies in most of their operating regions. To a large extent, the low engine efficiency comes from the combustion process, characterized by high-temperature exhaust gases which are currently dumped into the environment. Using a Waste Heat Recovery (WHR) system, the high-temperature exhaust can be used to boil and superheat a fluid to run a turbine and thus increase the engine efficiency. However, there are many challenges to realize the exhaust gas heat recovery in a safe manner while satisfying the emissions constraints set by legislation.

In this PhD thesis, models and control techniques are developed to enable exhaust gas heat recovery from highly dynamic heat sources such as the internal combustion engines. The models are used to understand the interactions between subsystems and design control algorithms. At a higher level, an integrated control approach is presented that optimizes the complete vehicle powertrain performance. The developed method can be used to improve the fuel economy of future vehicles with a Waste Heat Recovery system, while complying with the up-coming emission regulations.

Acronyms

ACEA	European Automobile Manufacturer's Association
AMOX	Ammonia Oxidation catalyst
CAC	Charge Air Cooling
DOC	Diesel Oxidation Catalyst
DPF	Diesel Particulate Filter
ECU	Engine Control Unit
EGR	Exhaust Gas Recirculation
FD	finite difference
FV	finite volume
HEV	hybrid electric vehicle
HVAC	heating, ventilation, and air conditioning
MB	moving boundary
MPC	Model Predictive Control
ORC	Organic Rankine Cycle
PI	proportional-integral control
PM	Particulate Matter
RC	Rankine Cycle
SCR	Selective Catalytic Reduction
VTG	Variable Turbine Geometry
WHR	Waste Heat Recovery

CHAPTER 1

Introduction

Abstract This work focuses on auto-calibration of diesel engines with Waste Heat Recovery systems. Using an integrated control fashion, the objective is to optimize on-line the complete powertrain by minimizing the total operational costs, associated with fuel and AdBlue consumption, for minimum CO₂ emissions. This chapter gives an overview of the challenges and state-of-the-art in automotive Waste Heat Recovery systems. Furthermore, it presents the main contributions and methodologies used in this thesis.

1.1 Drivers & challenges for diesel trucks

Despite diminishing fossil fuel resources and rising environmental impacts, the global energy consumption is still growing [1]. This brings challenges to the society, since the unwanted byproducts from industrial processes, such as greenhouse gases, lead to global warming and climate change. Fig. 1.1 shows the world energy consumption over the last 25 years. Consumption increased for all fuels, reaching record levels for every fuel type except nuclear power. As the world population continues to grow, the demand for energy and their environmental impacts will grow consequently.

According to the International Energy Agency (IEA), the transportation sector accounts for 27% of energy use worldwide. Around 94% of that energy comes from oil, from which the largest part is used in road transport, *i.e.*, 60% by light vehicles (gross vehicle weight of not more than 3.5 tonnes) and 22% by trucks.

Around 6% of the global CO₂ emissions are coming from trucks [2]. At the same time, the CO₂ emissions are in strong connection with the fuel consumption, which accounts for over one-third of the total truck operational costs. Although modern trucks

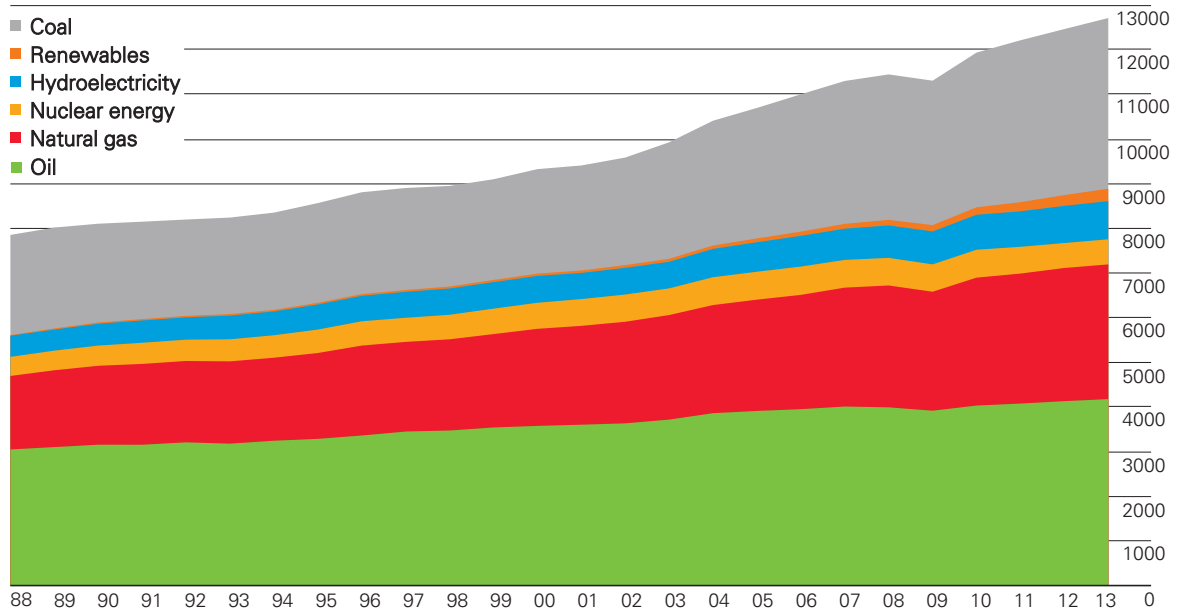


Figure 1.1: World energy consumption in million tonnes oil equivalent [1].

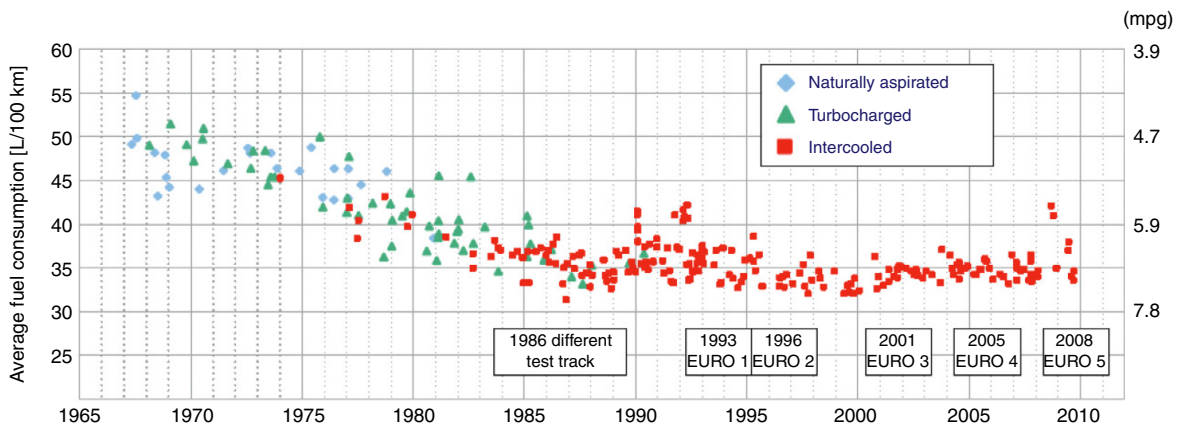


Figure 1.2: Historic fuel consumption for 40 tonne trucks (adapted from [2]).

have been equipped with technologies like common rail injection, automated gearboxes, turbo-charging and intercooling, the fuel economy has been stagnating for the last two decades (see Fig. 1.2). Therefore, fuel economy is a top priority for transport companies who buy buses and trucks.

The transportation sector is a focus point for CO₂ reduction, since the emissions from this sector are still growing due to the increasing demand for transport and mobility. According to ACEA (European Automobile Manufacturer's Association), for trucks the goal is a 20% absolute CO₂ reduction by 2020 [3], compared to current trucks CO₂ emissions. Moreover, in Europe, USA and Japan, a number of measures to reduce

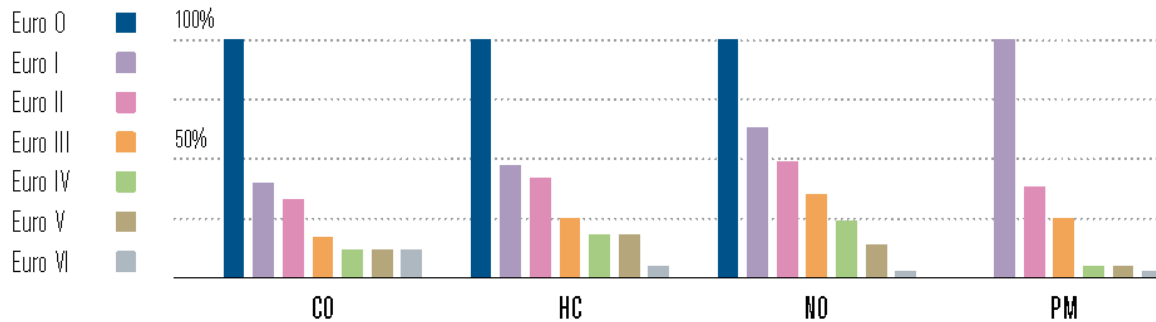


Figure 1.3: Exhaust gas pollutants for heavy commercial vehicles [2]. Euro 0 (before 1990), Euro I (1993), Euro II (1996), Euro III (2001), Euro IV (2005), Euro V (2008), Euro VI (2014).

pollutants from transportation have been established. Near zero impact-level pollutant limits have been set for new cars, light-weight vehicles and heavy-duty trucks.

Fig. 1.3 illustrates the exhaust gas emissions for European heavy-duty commercial vehicles. Today, a 40 tonne truck burns around a third less fuel than one produced in the 1970s. Per tonne transported, this corresponds to a fuel consumption of just one liter of diesel per 100 tonne-km. In terms of pollutant emissions, dramatic reductions have been achieved. Compared to levels in the 1980s (Euro 0), modern trucks pollutant emissions are approximately ten times less. The NO_x emissions are down by 86% compared to the ones from 1990s (Euro I), while particulate matter are reduced by 95%. In Europe, this resulted in an overall 60% reduction in particulate matter. However, the improvements in terms of emissions have reached a point where they conflict with fuel economy. This means, that a trade-off between emissions reduction and fuel economy is present. For this reason, the automotive industry is looking for alternative solutions to further improve the engine efficiency while complying with future emission legislation.

1.2 State-of-the-art in waste heat recovery

Energy recovery from processes generating waste heat is a promising solution to improve fuel economy. This solution has been successfully applied for power plants and refrigeration cycles. Recently, energy recovery received a lot of attention in automotive applications, where it is possible to exploit the energy from the engine heat using evaporators and expander (see Fig. 1.4). The technologies used are various: from mechanical turbo-compounding [4] and electrical turbo-compounding [5] to thermoelectric systems [6] and Rankine Cycles [7].

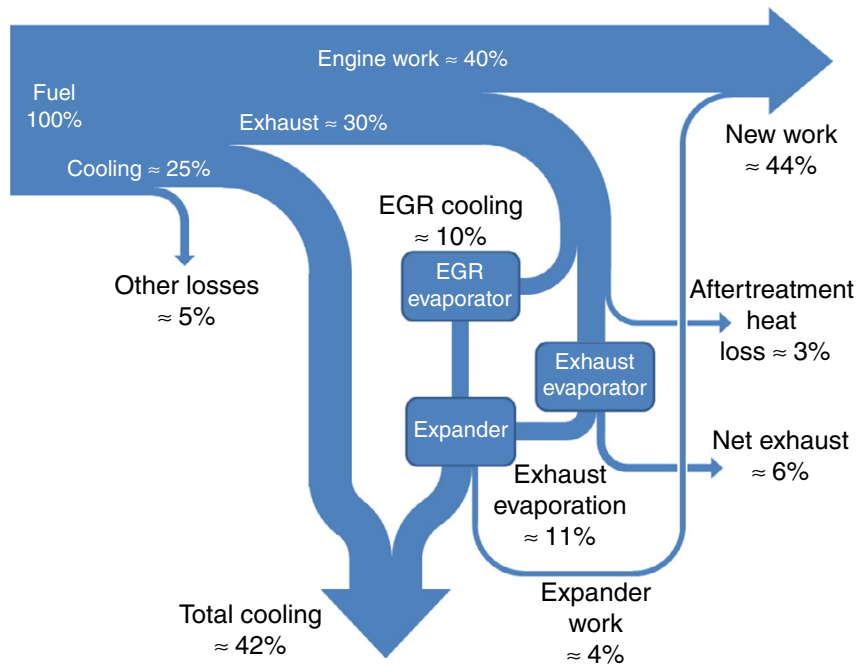


Figure 1.4: Sankey diagram of engine with WHR system [8].

The Rankine Cycle (RC) is a promising technology for power generation from heat. Although RC's have been used in the past, they regained interest because of their potential for small scale systems with low-temperature heat sources. This makes them suitable for automotive applications, where the physical space is limited and temperatures are relatively low compared to the ones from a thermal power station.

Even if small-scale RC's have relatively low efficiency, typically around 10% [9], their feasibility in automotive has been successfully demonstrated. For passenger applications, a WHR system can improve the fuel economy by 1.3% [10]. For heavy-duty applications, the heat quantity and quality is larger than for passenger cars meaning more potential for heat recovery. Higher exhaust gas mass flow rates and temperatures around 200-600°C are typical for trucks. Hence, for heavy-duty applications, waste heat recovery becomes a key solution to further improve the engine efficiency [11, 12].

1.2.1 The Rankine Cycle

Fig. 1.5a illustrates a typical Rankine Cycle. The RC components includes a boiler, an expander, a condenser and a pump. The working principle is as follows: a fluid is brought at high pressure and passed through a boiler, where it is vaporized. The vapor is expanded and as a result mechanical power is generated. The low pressure vapor

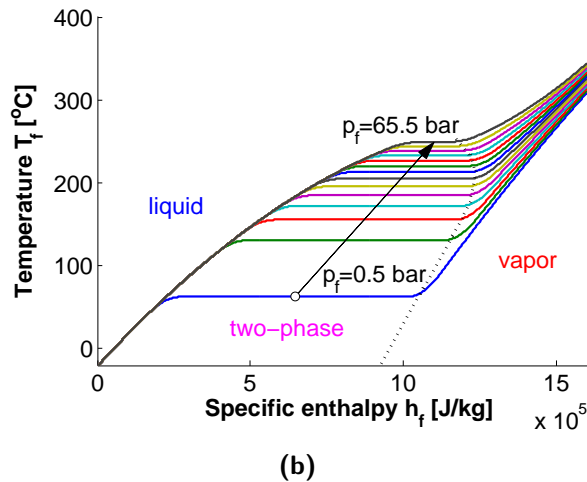
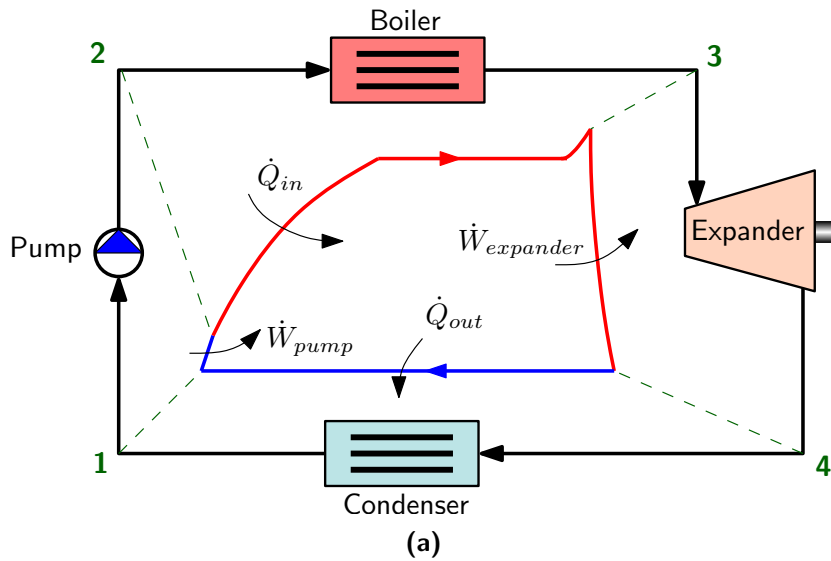


Figure 1.5: (a) The Rankine Cycle. (b) Ethanol temperature as a function of specific enthalpy and pressure.

is brought back to its liquid state using a condenser and then the cycle repeats. In automotive applications, the Organic Rankine Cycle (ORC) appears favorable over the traditional Rankine Cycle. The ORC uses instead of water an organic working fluid, *e.g.*, R245fa or ethanol. Typically, these organic working fluids are characterized by a lower boiling temperature, enabling low-grade waste heat recovery. Fig. 1.5b illustrates the ethanol temperature as a function of specific enthalpy and pressure. The phases that the ethanol goes through are: liquid, two-phase, and vapor.

The complexity of engines with WHR systems is very high (see Fig. 1.6). Hence, there are many challenges that need to be addressed, in order to make the WHR systems

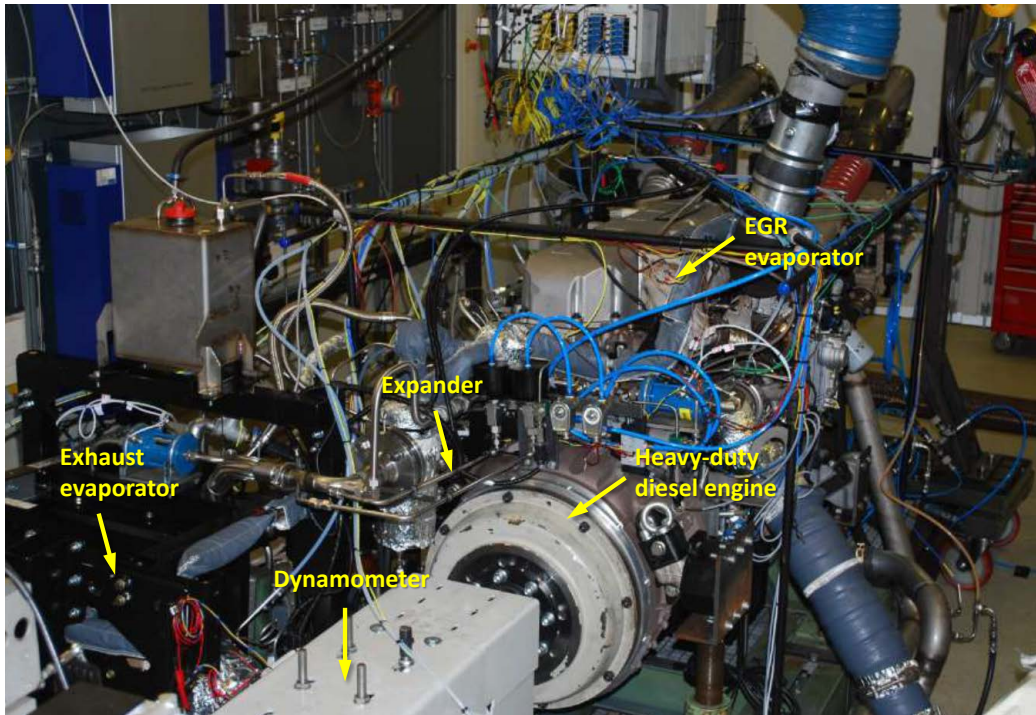


Figure 1.6: Photograph of the engine with waste heat recovery system experimental setup (courtesy of TNO Automotive).

operational in automotive. Three levels of challenges can be distinguished:

- WHR system (associated with low-level control strategies);
- Powertrain integration (associated with high-level control strategies);
- Business case (concerning cost versus profit).

WHR system level

In automotive applications, the WHR system has to deal with heat sources that are often unsteady or transient which can affect power generation and system performance. According to the driving conditions, the engine exhaust gas heat flow rate can experience large variations. This can lead to critical conditions such as: dry-out, flooding and temperature shocks in the components [13]. Furthermore, safe system operation related to vapor production needs to be guaranteed. The system is said to operate safely if vapor state is maintained before the expander. The presence of droplets can lead to expander damage [14]. To avoid these critical conditions, the optimal system and control design are essential.

The working fluid selection is an important aspect for the system efficiency and environmental impact. The working fluid must be selected, such that is compatible

with the system components. In addition, the properties need to be suitable for the application, without having the risk of ignition, degradation and component damage.

Powertrain integration level

There are size, weight and package configuration restrictions. In automotive, these aspects need to be considered, since the physical space is limited. Furthermore, the interaction between engine and WHR system needs to be accounted for. This includes considerations like the cooling demand, the exhaust gas backpressure and the effect on the tailpipe emissions.

For engines with WHR system, control is of paramount importance. Due to multiple actuators and process variables, the interaction between subsystems needs to be considered for control design. Under highly dynamic conditions, the control system needs to optimize the complete powertrain performance, to minimize fuel consumption within the emission constraints set by legislation. System modeling is an important tool in achieving such requirements. Hence, a model-based control approach is essential.

Business case level

The business case level is concerned with the costs due to the WHR system itself and impact on the overall vehicle, *e.g.*, the cooling system and powertrain energy management. Moreover, aspects related to the return on investment, maintenance costs, feasibility, system reliability and robustness, are some of the main objectives at this level. All these concerns are important to create a profitable business case.

This work concentrates on the WHR system level and powertrain integration level. For the business case level, an approximate calculation regarding the return on investment is presented.

1.3 Problem statement

Waste heat recovery in automotive engines is a new concept to achieve substantial fuel reduction. To guarantee the feasibility of this concept, many challenges arise that demand research. These challenges can be addressed at the design stage using dynamic models and simulations. Fig. 1.7 illustrates the studied engine scheme with aftertreatment, the WHR system, the control system, and the areas of research. For this system, the following problems are addressed:

- *Dynamic WHR system modeling.* The WHR system has a highly nonlinear behavior, mainly due to the two-phase phenomena and components nonlinear characteristic. Thus, the development of a complete system model is essential to analyze, design and apply control strategies.
- *Low-level control design.* Under highly dynamic driving conditions, the WHR system control is crucial. The control strategy should prevent critical situations and maximize the WHR system power output.
- *Integrated powertrain control approach.* Besides the low-level WHR system control, there is a need of an integrated high-level controller that optimizes the complete powertrain performance. This controller should minimize the running operational costs, associated with fuel and AdBlue consumption, while satisfying the tailpipe emission constraints.
- *System architecture.* It is important to consider the WHR system configuration with respect to the engine configuration and driving conditions. In other words, choosing a WHR system architecture that is the most beneficial in terms of performance and cost for a certain type of automotive application.
- *Business case.* At this level, a business case has to indicate if a WHR system provides an attractive return on investment.

1.3.1 Dynamic WHR system modeling

Modeling of a WHR system in a control-oriented fashion is not a simple task due to its complexity, nonlinear thermal behavior and real-time requirements. For vapor production, the heat exchanger is a key component within the WHR system and, as a result, requires special attention. Heat exchangers are commonly modeled using two approaches: moving boundary models and discretized models. These two methods are a trade-off between accuracy and computation. While the moving boundary approach results in a low-order, computationally efficient model, the discretized approach is known to give a more accurate but less computationally efficient model [15].

The Moving Boundary (MB) modeling approach divides the heat exchanger in three regions: liquid, two-phase and vapor separated by boundaries. During dynamical operation, the regions will expand or contract while the position of each phase transition will change. The main idea of MB models is to either track or capture the phase transitions position. The MB models have been successfully used in refrigeration

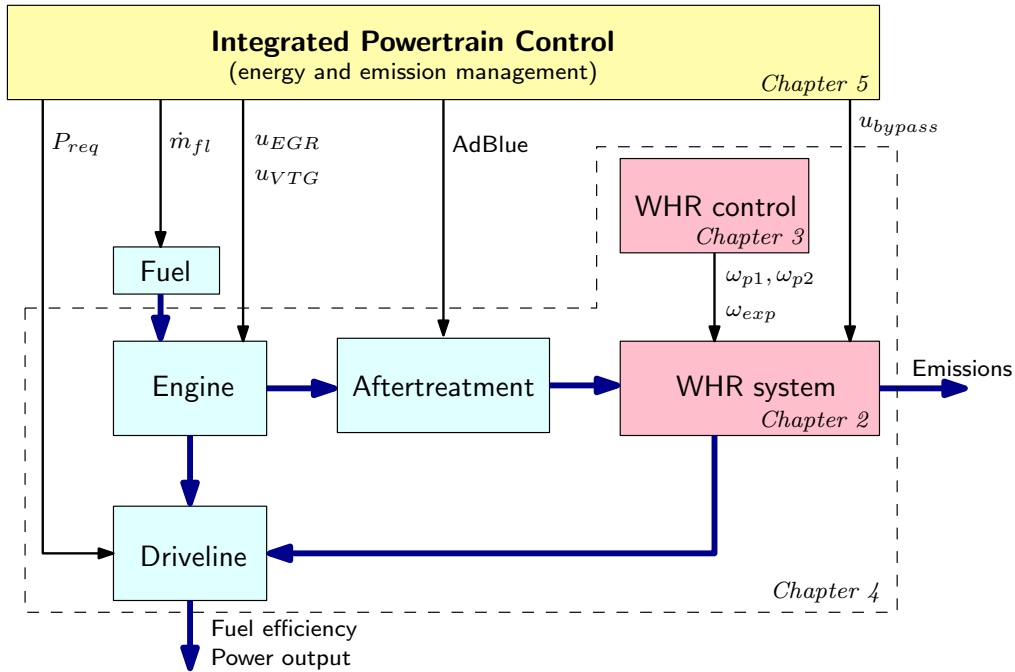


Figure 1.7: Schematic representation of the control system for an engine with aftertreatment and WHR system. The topics covered by each chapter is indicated in italic.

systems. In [16], a general heat exchanger model is developed based on the MB approach to perform simulations with different refrigerants types or mixtures. The MB approach is also used in [17], where attention is focused on switching algorithms to improve accuracy and robustness of the model. In [18], the MB model is validated for single and multi-evaporator air conditioning systems and found to give acceptable results against experimental data. However, in case the volume of one region becomes much smaller than the others, the MB models become singular and can lead to failures [17].

The discretized heat exchanger modeling approach, most commonly based on the Finite Volume (FV) [19–21] or Finite Difference (FD) formulation [22, 23], is a more robust method during start-up and shut-down processes. A disadvantage is that discretized models are more computationally expensive due to a larger number of system states.

In this thesis, we consider a modular heat exchanger design, in which the working fluid side is divided into three sections called modules. These modules are shifted along the heat exchanger length to improve the heat transfer between the flows and to avoid high temperatures in the wall material. In such a design, multiple phase transitions in a single pipe flow can occur, especially during transients. As a result, the modeling of modular heat exchangers using only the MB approach is not straightforward. This

thesis combines the FD approach with the MB approach to capture the effect of multiple phase transitions induced by the modular design. The model is validated on a state-of-the-art Euro-VI heavy-duty diesel engine equipped with a WHR system. The model validation is performed over the complete engine operating range and during highly dynamic engine conditions.

Concerning the complete WHR system model, the work and results in the literature are mostly oriented on modeling and control of steam cycles for large-scale power plants, with considerably different configurations in comparison with the small-scale types used in automotive. In [24] and [25] a Rankine Cycle system model is presented for a biomass-fired power plant. The model is intended to be used for equipment dimensioning and control design. Furthermore, in [14], [26] the focus is on ORC basic scheme modeling for energy recovery from a variable waste heat source. However, for automotive applications, only a few results are presented in the literature [27, 28]. Although these applications are characterized by highly transient conditions, validation results of dynamic WHR models are still lacking. This also holds for the combination of engine and WHR system.

In this thesis, a dynamic model of the complete WHR system is identified and validated. For control purposes, this model has to reasonably capture the real WHR system behavior and has to be computationally efficient. The main contributions of this study is the combination of:

- (i) modeling complex WHR system with two parallel evaporators, which is installed on a state-of-the-art Euro-VI diesel engine;
- (ii) systematic identification of WHR model parameters;
- (iii) and model validation of steady-state as well as dynamic behavior over a wide operating range using engine dynamometer results.

1.3.2 Low-level control design

The Rankine Cycles are mostly used in power plants where typically a steady heat source is available. Thus, the system operates in stationary conditions with little concern regarding transients that could disturb the cycle. In contrast, engine WHR systems are governed by highly transient heat sources that are rarely in steady-state. As a result, control of WHR systems is of paramount importance for automotive applications. The control strategy has to deal with highly dynamic engine conditions, cope with interaction within the system and take into account constraints.

Table 1.1: Literature overview for Waste Heat Recovery system control

Ref.	Input	Output	Control strategy
[29]	ω_p, ω_{exp}	T_{ev}, p_f	P control with feed-forward
[30]	ω_p, u_t	p_f, τ_{exp}	supervisory PID control
[27, 28, 31]	ω_p, ω_{exp}	T_{ev}, p_f	PI control
[32]	u_{egr}, u_{exh}	$T_{f,egr}, T_{f,exh}$	PI control
[33]	ω_p, ω_{exp}	T_{ev}, p_f	PID with feed-forward inverse model
[34]	v_e	T_{ev}	supervisory predictive control
[35]	$u_t, \omega_p,$ v_e, v_c	$P_{exp}, p_f,$ T_{ev}, T_c	LQR with PI control; generalized predictive control
[36]	u_o, ω_k	T_{ev}, T_a	Model Predictive Control

Table 1.1 gives a brief literature overview for WHR system used sensors and actuators and applied control strategies. These strategies [27–33] are explicitly dedicated to automotive applications, while [34, 35] are dedicated to power plants and [36] to refrigeration systems. A common used solution to control automotive WHR systems in industry is the PI or PID control strategy.

From Table 1.1, it follows that Model Predictive Control (MPC) has not been used for automotive WHR systems. For waste heat recovery in power plants, [34] presents a supervisory predictive controller for the evaporator, while [35] applies a generalized predictive control strategy. Furthermore, [36] presents an MPC strategy for vapor compression cycles in ventilating and air-conditioning (HVAC) systems (control inputs: u_o expansion valve opening, ω_k compressor speed; control outputs: T_{ev} evaporator outlet temperature, T_a supply air temperature). Compared to a classical PID strategy, the main advantages of an MPC strategy are:

- (i) it handles multivariable control problems naturally, in an optimal fashion;
- (ii) it explicitly takes into account actuator limitations;
- (iii) it considers the effect of measurable disturbances before they become visible at the plant output.

This thesis presents a switching Model Predictive Control strategy for a heavy-duty automotive WHR system. The studied WHR system consists of two parallel evaporators, one installed on the exhaust gas recirculation path and one downstream the aftertreatment system. The focus is on output power maximization, while the safety

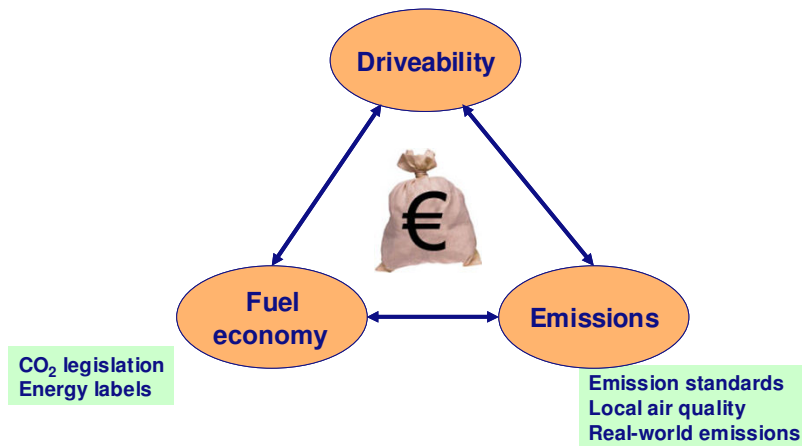


Figure 1.8: Powertrain optimization problem [37].

requirement is still guaranteed under highly dynamic engine disturbances. Based on the simulation results, the performance of the MPC strategy is evaluated using a classical PI control strategy as a benchmark.

1.3.3 Integrated powertrain control approach

The automotive industry is confronted with challenges to find a cost-efficient balance between drivability and fuel economy, within the emissions constraints, as illustrated in Fig. 1.8. Up to a large extent, future developments will be driven by legislation. With the introduction of Euro VI targets, the pollutants (CO, HC, NO_x, PM) limit is pushed towards near zero impact levels.

To meet the requirements of the upcoming legislation, it is necessary to optimize the entire powertrain performance. In other words, the synergy between engine, driveline, aftertreatment and WHR system has to be exploited during all operating conditions. The powertrain performance is expressed in terms of fuel economy, power output, and emissions (see Fig. 1.7). A solution to optimize the powertrain performance, is to design an Integrated Powertrain Control (IPC) approach [32]. With the increasing powertrain complexity, the goal of the IPC strategy is to provide a solution to the coupling of the energy and emission management. This will allow to optimally adapt the engine settings online (auto-calibration), such that the operational costs are minimized, while the tailpipe emissions constraints are satisfied.

Engine calibration consists in finding the engine tuning maps (*i.e.*, look-up tables) and control parameters, that are used in engine control. Due to the increased number of

parameters, manual tuning of engine maps is replaced by a model assisted calibration process [38]. Such a process relies on modeling methods, to reduce the number of experimental tests to build the engine response. As the modeling methods become more and more accurate due to the numerous studies in this area, it is natural to move from manual engine tuning to online model-based adaptation techniques, which we call auto-calibration. This will increase robustness while it will reduce the effort and development time for the engine calibration process.

Only a few studies deal with overall powertrain system performance with WHR systems. In [10], the fuel saving potential for a passenger vehicle with a WHR system is presented. The study shows the effect of vehicle integration and restrictions on WHR power output due to the architecture of the on-board electric system, package considerations, increased weight, cooling demand and exhaust gas backpressure. However, the study does not consider the impact of the WHR system on vehicle emissions.

In this thesis, we extend the integrated energy and emission management from [32] to a heavy-duty diesel engine with an electrified WHR system. The advantages of an electrified WHR system are: it gives more control flexibility due to an additional degree of freedom, by allowing energy to be stored in a battery for latter usage and it provides easy WHR power output manipulation. Moreover, an electrified WHR system can be easily integrated within a hybrid electric vehicle (HEV) architecture. In the future, it is expected to combine the benefits of a HEV for city driving with the benefits of a WHR system for highway driving.

1.3.4 System architecture

The WHR system configuration plays an important role towards fuel consumption minimization. Therefore, for each driving condition a certain type of system configuration is most suitable. In this thesis, three driving conditions are analyzed: urban, rural and highway. The urban and rural driving is dominated by a relatively low exhaust gas temperature. Thus, an electrified WHR system that allows electrical energy storage using a battery, may be a suitable solution. However, for highway conditions (*e.g.* long-haul applications), typically dominated by driving on a relatively flat terrain, this may not be the case. A more suitable system configuration could be a WHR system mechanically coupled to the engine crankshaft. Even if a WHR system configuration mechanically coupled to the engine is more cost effective due to a lower number of components, a disadvantage from a control perspective is the reduced degree of freedom. In such a design, the expander speed is not free to vary, thus limiting the WHR system

performance. The system analysis carried out in this thesis, quantifies the fuel economy, of each system configuration according to the driving conditions.

1.3.5 Business case

To start the series production of automotive WHR systems, a business case analysis needs to be performed. First, the system should be beneficial in terms of fuel economy, which is one of the objectives of this thesis. Second, the system component sizing and system configuration should be chosen such that a good trade-off is obtained between cost and performance. The optimum system sizing problem is not addressed, however the system performance, in terms of power output and operational costs for different system configurations, is addressed in this thesis. Third, the profit from fuel savings due to a WHR system should amortize the production and maintenance costs of the system. Based on the obtained fuel saving, a brief analysis concerning the return on investment period is provided in Chapter 6.

1.4 Outline of this thesis

This thesis is divided into four chapters, that cover the topics illustrated in Fig. 1.7. Each chapter represents a research paper and is therefore self-contained with respect to the other chapters. Thus, each chapter can be read independently.

In Chapter 2, the model development and validation for a modular two-phase heat exchanger is presented. The model is developed for temperature and vapor quality prediction and for control design of the waste heat recovery system. Compared to other studies, the model is able to capture multiple phase transitions along the fluid flow by combining the finite difference approach with a moving boundary approach. The model is validated using experiments from a state-of-the-art Euro-VI heavy-duty diesel engine equipped with a waste heat recovery system. This chapter is based on the journal paper [39], of which a preliminary version was presented in [40].

Chapter 3 considers the modeling of the complete waste heat recovery system. Subsequently, the low-level control design is presented. The objective is to guarantee safe system operation, while maximizing the waste heat recovery system output power. To achieve this, a switching model predictive control strategy is developed. The simulation results show the effectiveness of the proposed controller in comparison with a classical proportional-integral control strategy and a nonlinear model predictive control strategy. This chapter is based on the journal publication [41], of which earlier versions are presented in [42] and [43].

The low-level control of a waste heat recovery system with expander and pumps decoupled from the engine is presented in Chapter 4. It is shown that using a mechanically decoupled architecture, up to 29% net output power improvement is obtained as compared to a waste heat recovery system with the expander coupled to the engine. This is demonstrated in simulations based on the waste heat recovery system model and realistic disturbances from a Euro-VI heavy-duty diesel engine. This chapter is based on [44].

Chapter 5 presents an integrated energy and emission management strategy for an Euro-VI diesel engine with waste heat recovery system. This strategy optimizes the CO₂-NO_x trade-off by minimizing the operational costs associated with fuel and AdBlue consumption while satisfying tailpipe emission constraints. Compared to the baseline control strategy, it is shown that the optimal IPC strategy with an electrified WHR system reduces the CO₂ emissions by 3.5% within the tailpipe NO_x emissions constraints. This chapter is based on the journal paper [45].

Finally, in Chapter 6, conclusions are drawn and recommendation for future research are indicated.

1.5 List of publications

Journal articles

- E. Feru, N. Murgovski, B. de Jager, and F. Willems. Supervisory control of a heavy-duty diesel engine with an electrified waste heat recovery system. *Submitted to Control Engineering Practice*, 2015. – Chapter 5
- E. Feru, F. Willems, B. de Jager, and M. Steinbuch. Modeling and control of a parallel waste heat recovery system for Euro-VI heavy-duty diesel engines. *Energies*, 7(10), 6571-6592, 2014. – Chapter 3
- E. Feru, B. de Jager, F. Willems, and M. Steinbuch. Two-phase plate-fin heat exchanger modeling for waste heat recovery systems in diesel engines. *Applied Energy*, 133, 183-196, 2014. – Chapter 2
- F. Willems, F. Kupper, G. Rascanu, and E. Feru. Integrated energy and emission management for diesel engines with waste heat recovery using dynamic models. *Oil and Gas Science and Technology*, 70(1), 143-158, 2014.

Proceedings & Conference Contributions

- E. Feru, and X. Luo. Towards constrained optimal control of spark-ignition engines. Conference Paper : *Proceedings of the European Control Conference (ECC 2015)*, 15-17 July 2015, Linz, Austria, (pp. 1397-1402).
- E. Feru, F. Willems, B. de Jager, and M. Steinbuch. Control of a waste heat recovery system with decoupled expander for improved diesel engine efficiency. Conference Paper : *Proceedings of the European Control Conference (ECC 2015)*, 15-17 July 2015, Linz, Austria, (pp. 148-153). – Chapter 4
- E. Feru, F. Willems, B. de Jager, and M. Steinbuch. Model predictive control of a waste heat recovery system for automotive diesel engines. Conference Paper : *Proceedings of the 18th International Conference on System Theory, Control and Computing*, 17-19 October 2014, Sinaia, Romania, (pp. 664-669).
- E. Feru, F. Willems, G. Rascanu, B. de Jager, and M. Steinbuch. Control of automotive waste heat recovery systems with parallel evaporators. Conference Paper : *Proceedings of the FISITA World Automotive Congress 2014*, 2-6 June 2014, Maastricht, The Netherlands, FISITA Techn. Paper: F2014-CET-015.
- E. Feru, F. Willems, C. Rojer, B. de Jager, and M. Steinbuch. Heat exchanger modeling and identification for control of waste heat recovery systems in diesel engines. Conference Paper : *Proceedings of the American Control Conference (ACC 2013)*, 17-19 June 2013, Washington DC, USA, (pp. 2866-2871).
- E. Feru, F. Kupper, C. Rojer, X. Seykens, F. Scappin, W. Willems, J. Smits, B. de Jager, and M. Steinbuch. Experimental validation of a dynamic waste heat recovery system model for control purposes. Conference Paper : *Proceedings of the 2013 SAE World Congress*, 16-18 April 2013, Detroit, MI, USA, SAE Techn. Paper 2013-01-1647.

Supervised projects

- R. Salama. Analysis of the pumps dynamic behaviour for a Waste Heat Recovery system, *BSc thesis*, Eindhoven University of Technology, January 2015.
- S.J.M. Koopmans. Hardware specifications for a Waste Heat Recovery test set-up, *BSc thesis*, Eindhoven University of Technology, September 2014.

-
- M. Oom. Identification and validation of an expander model for automotive waste heat recovery systems, *BSc thesis*, Eindhoven University of Technology, June 2014.
 - R.R.M. Reinders. Steady state analysis of a Waste Heat Recovery system with decoupled expander and pumps design, *BSc thesis*, Eindhoven University of Technology, April 2014.
 - G. Rascanu. Integrated Powertrain Control for truck engines with Waste Heat Recovery system. *MSc thesis*, CST 2013.095, Eindhoven University of Technology, Report number: CST 2013.095, September 2013.

Two-phase plate-fin heat exchanger modeling¹

Abstract This chapter presents the modeling and model validation for a modular two-phase heat exchanger that recovers energy in heavy-duty diesel engines. The model is developed for temperature and vapor quality prediction and for control design of the waste heat recovery system. In the studied waste heat recovery system, energy is recovered from both the exhaust gas recirculation line and the main exhaust line. Due to the similar design of these two heat exchangers, only the exhaust gas recirculation heat exchanger model is presented in this chapter. Based on mass and energy conservation principles, the model describes the dynamics of two-phase fluid flow. Compared to other studies, the model is able to capture multiple phase transitions along the fluid flow by combining finite difference approach with moving boundary approaches. The developed model has low computational complexity, which makes it suitable for control design and real-time implementation.

To validate the model, experiments are performed on a state-of-the-art Euro-VI heavy-duty diesel engine equipped with the waste heat recovery system. Simulation results show good accuracy, over the complete engine operating range, with average error below 4%. This is demonstrated on transitions between stationary operating points and on a dynamic response to a standard world harmonized transient cycle for both cold-start and hot-start conditions.

¹This chapter is based on [39].

2.1 Introduction

Due to stringent CO₂ emissions regulation, increased fuel costs and concerns about energy security, the automotive industry invests much effort in developing fuel efficient powertrains. Despite that, for trucks the fuel efficiency has been stagnating for the last two decades. However, for CO₂ emissions, USA legislation indicates a 20% reduction by 2020. In Europe, similar requirements are expected to be introduced. Studies [29, 46] show that even with advanced engine technologies around 60-70% of the fuel energy is still lost through the coolant or the exhaust system. Thus, energy recovery from the exhaust is a promising technology allowing a 4-5% increase in the engine efficiency [30, 47, 48]. These energy recovery systems are called Waste Heat Recovery (WHR) systems.

The technologies used in a WHR system are various: from mechanical turbo-compounding [4] and electrical turbo-compounding [5] to thermoelectric systems [6] and Rankine Cycles [7]. For heavy-duty applications, the Rankine Cycle promises high potential in terms of costs and overall efficiency improvement of the engine [49]. Moreover, it has been shown in [50] that on a truck diesel engine, due to the low temperature sources, the use of an Organic Rankine Cycle (ORC) appears to be favorable in comparison with the classical Rankine Cycle. The main difference between the ORC and classical Rankine Cycle is the use of an organic working fluid instead of water [51]. Regardless the Rankine Cycle type, a control design is necessary to optimize the efficiency of the overall WHR system and to ensure safe operation, i.e., no liquid at the heat exchanger outlet. In automotive, control of engines with WHR systems is challenging due to the large number of sensors and actuators, strong coupling between the engine and WHR system and continuous changes in time of the heat available for recovery. Moreover, to maximize the WHR efficiency the system is required to be operated close to the constraint boundaries, while safety is still guaranteed. Thus, dynamical modeling of such systems plays an important role for control and performance prediction.

The dynamic behavior of a WHR system is mainly influenced by the heat exchanger and condenser. These components are most commonly modeled using two approaches: moving boundary models and discretized models. The Moving Boundary (MB) models [14, 16, 52] divide the heat exchanger in three regions: liquid, two-phase and vapor separated by boundaries. Due to dynamical conditions, the regions will expand or contract while the position of each phase transition will change. The main idea of MB models is to either track or capture the phase transitions position. However, when the volume of one region becomes much smaller than the others, the MB models become

singular [17]. A more robust approach during start-up and shut-down processes is obtained using discretized models, most commonly based on the Finite Volume (FV) [19–21] or Finite Difference (FD) formulation [22, 23]. A disadvantage is that discretized models are more computationally expensive due to a larger number of system states.

Many of the heat exchanger models have been designed for large-scale power plants and refrigeration systems. For small-scale applications characterized by highly dynamic conditions, e.g. automotive applications, only a few studies have been reported. In [28], a dynamic heat exchanger model has been developed and validated for a passenger car application. The model represents a tube-finned heat exchanger based on the MB principle. The studied heat exchanger is non-modular meaning the two flows travel the complete heat exchanger length uniformly. In contrast, we consider a modular heat exchanger design, in which the working fluid side is divided into three sections called modules. These modules are shifted along the heat exchanger length to improve the heat transfer between the flows and to avoid high temperatures in the wall material. In such a design, multiple phase transitions in a single pipe flow can occur, especially during transients. As a result, the modeling of modular heat exchangers using only the MB approach is not straightforward.

In this chapter, a dynamic model for a modular plate-fin heat exchanger is presented. The model is developed by combining the FD approach with the MB approach to capture the effect of multiple phase transitions induced by the modular design. The contributions are as follows. First, the mass and energy balance equations for the exhaust gas side, working fluid side, and heat exchanger wall are reconsidered. At the heat exchanger wall, the energy balance includes the transverse conductivity through the wall. To reduce the model complexity a dynamic range analysis is performed. Second, the resulting model is discretized in space and time using a staggered grid approach based on a FD method. Third, to account for the multiple phase transitions, a phase-change detection algorithm is implemented that mimics the MB approach within each discretization cell. Fourth, the model is validated on a state-of-the-art Euro-VI heavy-duty diesel engine equipped with a WHR system. The model validation is performed over the complete engine operating range and during highly dynamic engine conditions. In comparison with previous developments [40, 42], the simulation results demonstrate an improved representation of the real system in terms of accuracy, while the real-time requirements are reached.

This chapter is organized as follows. Section 2.2 presents the layout and working principle of the studied experimental set-up. In Section 2.3, the mathematical description including the heat transfer relations are given and a non-dimensional form

of the heat exchanger model is derived. In Section 2.4, the resulting partial differential equations are discretized with respect to time and space. The model is experimentally validated and the results are discussed in Section 2.5. Finally, Section 2.6 presents the conclusions.

2.2 System description

The experimental set-up (see Fig. 2.1) consists of a 375 kW, 12.9 l, 6 cylinder diesel engine, which is equipped with a 2500 bar common rail fuel injection system, sa cooled high pressure Exhaust Gas Recirculation (EGR) system, Variable Turbine Geometry (VTG) and Charge Air Cooling (CAC). The exhaust aftertreatment system contains a Diesel Oxidation Catalyst (DOC), a Diesel Particulate Filter (DPF), a Cu-Zeolite SCR catalyst (SCR) and an Ammonia Oxidation catalyst (AMOX) to avoid unwanted NH_3 slip. To meet the upcoming CO_2 regulations, a WHR system is integrated with the engine.

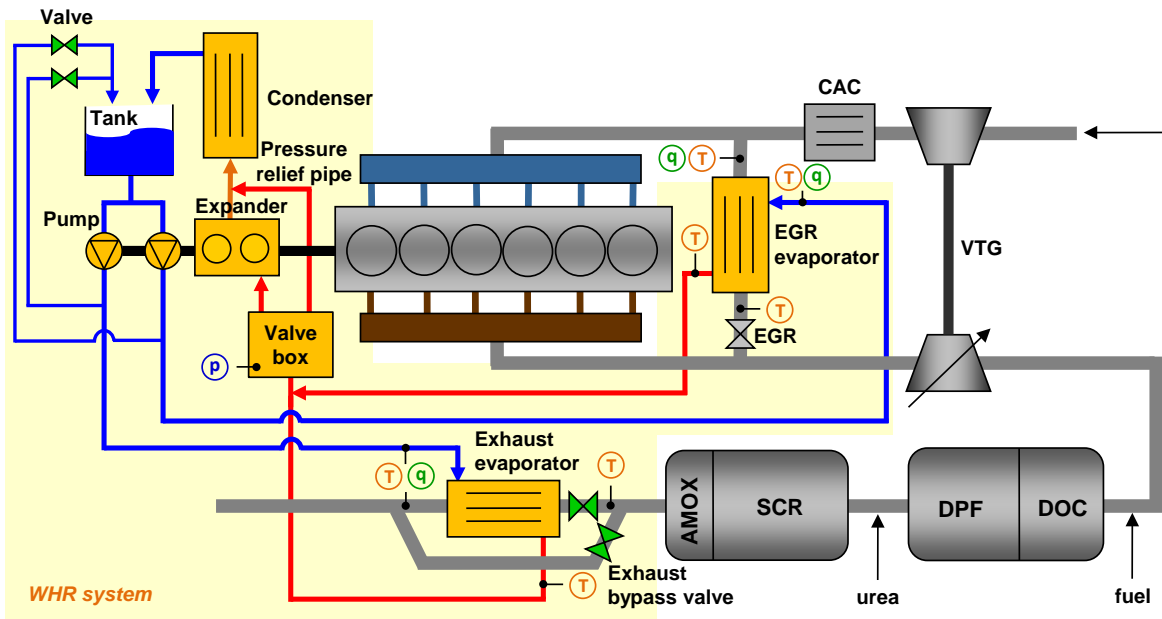


Figure 2.1: Schematic representation of a heavy-duty diesel engine equipped with a WHR system.

In this WHR system, the heat is recovered from both the EGR line and exhaust line using two evaporators, one for each of the exhaust circuits. The recovered exhaust heat is converted to mechanical power, by means of a piston expander. The piston

expander and pumps are mechanically coupled with the engine crankshaft. As a result, the recovered power is directly transmitted to the driveline. The selected working fluid is pure ethanol, because of its physical and thermodynamic properties, which are suitable for applications with low temperature heat sources. The ethanol mass flow is controlled by two bypass valves, one for each evaporator. To close the Rankine Cycle, the ethanol is cooled back before the tank by means of a condenser. To comply with the vehicle and WHR system cooling capabilities, an exhaust bypass valve is installed before the exhaust evaporator. This valve bypasses the exhaust gas and therefore manipulates the input heat for the exhaust evaporator. Due to drivability requirements, the power delivered by the WHR system must be interrupted temporarily, e.g., during braking or gear shifting. In this case, an electric bypass valve is activated which shuts off the vapor flow to the expander and thereby reduces the generated torque. For safety reasons, a 60 bar pressure relief valve is used that releases the excess vapor flow before the condenser. The electric bypass valve and the pressure relief valve are located in the valve box.

The considered experimental set-up is furthermore equipped with temperature (T), pressure (p) and flow (q) sensors. The measurement system consists of thermocouples of type T and K to measure temperature, thin-film pressure sensors to measure pressure, Coriolis flow meters to measure the exhaust gas mass flow rate and helicoidal flow meters to measure the ethanol mass flow rate. The uncertainty of the measurement due to sensor error is up to 5 K for the temperature, $\pm 1.5\%$ regarding the pressure, and $\pm 0.3\%$ for the exhaust gas and ethanol mass flow rate. These accuracies are indicated by the individual sensor manufacturer. However, when installed in an engine platform, several factors can worsen the measurement accuracy. For instance, the exhaust gas temperature measurement is affected by a non-uniform temperature distribution over the exhaust gas pipe cross section. Furthermore, the fluid mass flow sensor accuracy is given for a constant fluid flow in the pipe. However, in the studied platform the flow is not constant but rather pulsating due to the pumping behavior. These effects influence the accuracy of the measured system performance and of the energy flow rates.

The engine with WHR system is connected to an engine dynamometer for testing the system under any engine load and rotational speed within the engine operating range. Furthermore, the WHR system was protected with insulation material to minimize heat losses to the environment. The layout of the complete system, engine with WHR system, was designed based on the real vehicle layout. The purpose of this set-up is to demonstrate the potential of the WHR system, to develop and validate dynamical models and to design and test control strategies. In this study, recorded data is used to validate a dynamic model for the EGR heat exchanger.

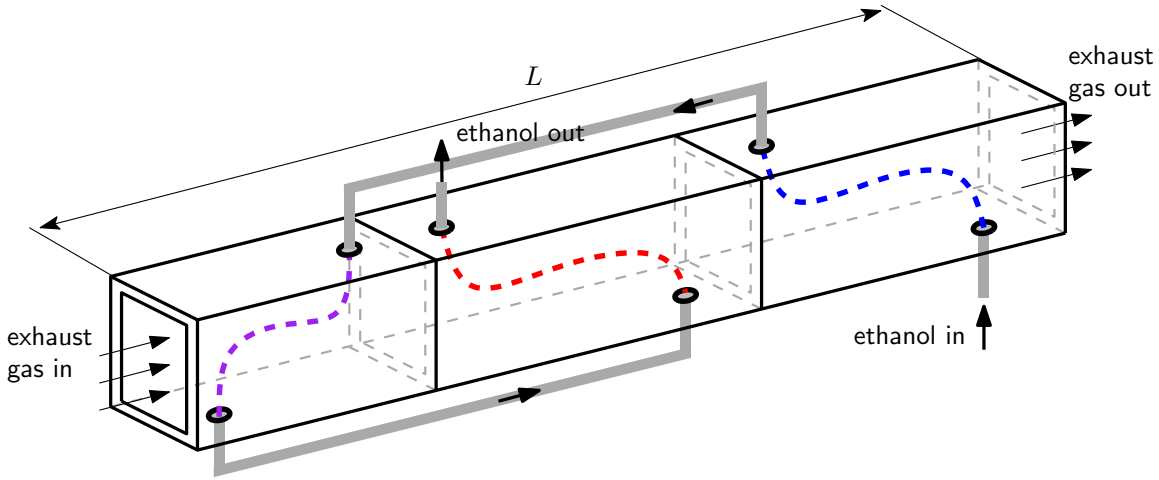


Figure 2.2: Diagram of the Exhaust Gas Recirculation heat exchanger modular design.

2.3 Heat exchanger modeling approach

The objective of this study is to develop a heat exchanger model with the following properties: *(i)* good prediction of the vapor quality, *(ii)* good dynamical prediction of the outlet working fluid temperature and *(iii)* good prediction of the outlet exhaust gas temperature. Each of these properties are proposed for the following reasons: *(i)* is crucial for safe system operation, *(ii)* is important for control design and *(iii)* is in strong relation with the engine out emissions and proper function of the EGR system. In the considered WHR system, two heat exchangers are used that differ in size and geometry. However, the dynamic behavior is similar and can be described by the same mathematical relations. Thus, to avoid repetition, only the EGR evaporator is described.

The EGR evaporator (Fig. 2.2) is a prototype plate-fin heat exchanger, in which the two fluids flow parallel to each other, but in opposite direction. The plates are vertically aligned and connected with fins. Heat transfer enhancement is achieved by means of a staggered fins arrangement similar to the arrangement in [53].

The heat exchanger is divided into three modules. The main reason for this is to avoid high wall temperatures, which could harm the wall material. In a classical counter-flow heat exchanger design, the wall temperature is highest where the working fluid exits and the exhaust gas enters the heat exchanger. From the working fluid flow direction perspective, by dividing the heat exchanger into three modules and swapping the last two modules the wall peak temperature is reduced. This is due to the fact that a lower exhaust gas temperature corresponds to the module with the working fluid in vapor

state. To reduce heat losses to the environment, the heat exchanger is wrapped in an insulation layer.

2.3.1 Mass and energy conservation

The mathematical description of the heat exchanger is formulated using the general conservation principles for mass and energy. Radiation and viscous friction are neglected, since their contributions are much smaller than the remaining terms. In addition, the exhaust gas change in density is neglected as a function of temperature and pressure, and thus no dynamic mass balance equation is used at the exhaust gas side. Furthermore, we consider the temperature to be uniform along the transverse direction for both the exhaust gas and working fluid. The time derivative of pressure is neglected for both the working fluid side and exhaust gas side. This assumption is made, since the pressure dynamics are considered to be characterized by small time scales in comparison to the relevant thermal phenomena. Thus, no equation for momentum conservation is used. Consequently, the heat exchanger model can be written by the following set of partial differential equations.

Conservation of mass (working fluid):

$$V_f \frac{\partial \rho_f}{\partial t} + L \frac{\partial \dot{m}_f}{\partial z} = 0, \quad (2.1)$$

Conservation of energy:

$$\rho_g c_{pg} V_g \frac{\partial T_g}{\partial t} = c_{pg} \dot{m}_g L \frac{\partial T_g}{\partial z} - \alpha_g S_g (T_g - T_{wg}) - \dot{Q}_{loss}, \quad (2.2a)$$

$$\rho_f V_f \frac{\partial h_f}{\partial t} = -\dot{m}_f L \frac{\partial h_f}{\partial z} + \alpha_f S_f (T_{wf} - T_f), \quad (2.2b)$$

Conservation of energy at the wall:

$$\rho_w c_{pw} \gamma_w V_w \frac{\partial T_{wg}}{\partial t} = \alpha_g S_g (T_g - T_{wg}) - \frac{\lambda_w S_w}{\delta_w} (T_{wg} - T_{wf}), \quad (2.3a)$$

$$\rho_w c_{pw} (1 - \gamma_w) V_w \frac{\partial T_{wf}}{\partial t} = -\alpha_f S_f (T_{wf} - T_f) + \frac{\lambda_w S_w}{\delta_w} (T_{wg} - T_{wf}), \quad (2.3b)$$

where L is the heat exchanger length, V_f is the volume occupied by the working fluid including the connecting pipes between modules and V_g is the volume occupied by the exhaust gas. Despite the connecting pipes, for simplicity we assume constant cross sectional area along the heat exchanger length. A constant density ρ_g and heat capacity c_{pg} is assumed for the exhaust gas side. The working fluid density ρ_f however changes as a function of the enthalpy h_f and pressure p_f . For the wall, the volume V_w includes

the plate material and fins but not the casing material. Note that a constant factor $\gamma_w = 0.6$ is introduced in (2.3) to separate the mass of the wall, i.e., $M_w = \rho_w V_w$, including fins on the exhaust side from the mass of the wall on the working fluid side.

Note that in (2.3) we only consider the transverse wall conduction computed based on two temperature points T_{wg} and T_{wf} . The longitudinal heat conduction is neglected since it is significantly less important than the transverse heat conduction (see, e.g., [16]). This reduces the modeling problem from a two dimensional to a one dimensional problem. Furthermore, the heat conduction between the three heat exchanger modules (Fig. 2.2) is neglected, since the core (consisting of plates and fins) is separated between modules.

The change in phase occurs only on the working fluid side and not on the exhaust gas side. Therefore, in (2.2a) we choose to describe the exhaust gas enthalpy using a well known approximation $h_g = c_{pg}T_g$. Furthermore, since the heat exchanger operates within a limited temperature window, a constant heat capacity for the wall c_{pw} is considered. The transverse conductivity in the wall is important for steady-state and dynamic behavior. There are several ways to describe the wall transverse conductivity. For simplicity, in (2.3) we characterize the wall by two states T_{wg} and T_{wf} , representing the wall surface temperature in contact with the exhaust gas and working fluid, respectively.

The heat loss from an insulated heat exchanger is expressed at steady-state by

$$\dot{Q}_{loss,ss} = \frac{S_{cs}(T_{g,avg} - T_{amb})}{\frac{1}{\alpha_g} + \frac{\delta_{cs}}{\lambda_{cs}} + \frac{\delta_{ins}}{\lambda_{ins}} + \frac{1}{\alpha_{amb}}}, \quad (2.4)$$

where S_{cs} is the heat exchanger casing surface area, δ_{cs} is the thickness and λ_{cs} is the thermal conductivity of the casing, respectively. The insulating layer is characterized by a thickness δ_{ins} and a thermal conductivity λ_{ins} . The average exhaust gas temperature $T_{g,avg}$ is obtained based on the inlet and outlet temperature, i.e., $T_{g,avg} = (T_{g,in} + T_{g,out})/2$. The heat transfer coefficient to the ambient α_{amb} is considered to be constant.

The heating-up thermal inertia of the casing material is introduced as a first order system response:

$$\frac{d\dot{Q}_{loss}}{dt} = \frac{1}{\tau_{cs}} \left(\dot{Q}_{loss,ss} - \dot{Q}_{loss} \right), \quad (2.5)$$

where τ_{cs} is the heat exchanger casing time constant obtained based on the mass and heat capacity of the casing and insulation material.

2.3.2 Heat transfer

The heat transfer from the exhaust gas to the wall and from wall to the working fluid is modeled as forced convection. In the wall, heat conduction is considered based on the wall conductivity λ_w , the wall thickness δ_w and surface area S_w expressed for one plate.

To describe the convective heat transfer from a moving fluid to the solid boundary (wall), a heat transfer coefficient α is employed. This quantity depends on the relevant fluid and process properties as well as geometrical configurations of the wall. In general, the heat transfer coefficient is determined experimentally and correlations for various technical configurations are derived [54]. For this purpose, a dimensionless heat transfer coefficient called Nusselt number is used:

$$\text{Nu} = \frac{\alpha d_h}{\lambda}, \quad (2.6)$$

where d_h is the hydraulic diameter and λ is the thermal conductivity of the fluid. For parallel plates, the hydraulic diameter d_h is twice the spacing between the plates.

To derive correlations for the Nusselt number in forced convection, two other dimensionless numbers are used, namely the Reynolds number and the Prandtl number. The Reynolds number describes the flow characteristics and is given by:

$$\text{Re} = \frac{\dot{m}_{vel} d_h}{\eta}, \quad (2.7)$$

where \dot{m}_{vel} is the mass velocity and η is the fluid dynamic viscosity. The mass velocity is $\dot{m}_{vel} = \dot{m}/A$ with \dot{m} the mass flow rate and A the flow cross sectional area. Further, the Prandtl number is given by:

$$\text{Pr} = \frac{\eta c_p}{\lambda}, \quad (2.8)$$

where c_p is the heat capacity of the fluid.

On the exhaust gas side, the heat transfer is enhanced by fins and thus, a Nusselt number correlation that can be used for heat transfer coefficient calculation in staggered finned surfaces has to be selected. On the working fluid side, in the liquid region, the Reynolds number indicates the flow is laminar ($\text{Re}_l < 2300$) while in the vapor region, the Reynolds number indicates the flow is turbulent ($\text{Re}_v > 4000$). Therefore, appropriate Nusselt numbers correlation in single-phase are selected from [54].

Using the appropriate Nusselt numbers correlation for the working fluid, the local single-phase heat transfer coefficients $\alpha_{f,l}$ and $\alpha_{f,v}$ are determined for the liquid and vapor region, respectively. In the two-phase region, the heat transfer coefficient α_f in vertical

tubes is used:

$$\frac{\alpha_f}{\alpha_{f,l}} = \left\{ (1 - \chi_q)^{0.01} \left[(1 - \chi_q) + 1.9\chi_q^{0.6} \left(\frac{\rho_l}{\rho_v} \right)^{0.35} \right]^{-2.2} + \chi_q^{0.01} \left[\frac{\alpha_{f,v}}{\alpha_{f,l}} \left(1 + 8(1 - \chi_q)^{0.7} \left(\frac{\rho_l}{\rho_v} \right)^{0.67} \right) \right]^{-2} \right\}^{-0.5}, \quad (2.9)$$

where ρ_l and ρ_v are the saturated liquid density and saturated vapor density, respectively. The vapor quality χ_q is obtained from:

$$\chi_q = \max(0, \min(1, \chi_r)), \quad \chi_r = \frac{h_f - h_l}{h_v - h_l}, \quad (2.10)$$

where χ_r represents the vapor ratio, with h_l and h_v the saturated working fluid enthalpy in liquid state and vapor state at a specific pressure p_f , respectively.

Many empirical correlations for describing the saturated flow boiling exist in the literature [55, 56]. The reason for selecting (2.9) comes from the fact that it covers fluids with values of ρ_l/ρ_v from 3.75 to 1017, i.e., typical for our application. Furthermore, the expression is smooth and goes to its proper limits $\alpha_{f,l}$ and $\alpha_{f,v}$ at $\chi_q = 0$ and $\chi_q = 1$, respectively.

Remark 2.3.1. *Note that the two-phase heat transfer coefficient (2.9) corresponds to a tube arrangement. However, the heat exchanger which we aim to model has plates instead of tubes. The main reason for using (2.9) is that, considering the two-phase nature of our problem, the physics for boiling inside tubes is well-established [54]. Moreover, in Section 2.5, we will show that using (2.9) produces a model with acceptable validation properties.*

To predict the phase change along the heat exchanger fluid flow, properties of the working fluid have to be provided. In the considered WHR system and experimental set-up, an analysis of the physical and thermodynamic properties indicates that ethanol is a good candidate as a working fluid. In this study, the used working fluid properties are the saturation temperature, the temperature-enthalpy characteristic and the density-enthalpy characteristic. In [40], the ethanol properties have been described mathematically to create independence from chemical databases. Here, a similar approach is used to express the saturation temperature. However, the working fluid temperature, heat transfer coefficient and density as a function of enthalpy changes are smoothed around the liquid and vapor saturated enthalpy h_l and h_v , respectively (see Fig. 2.3).

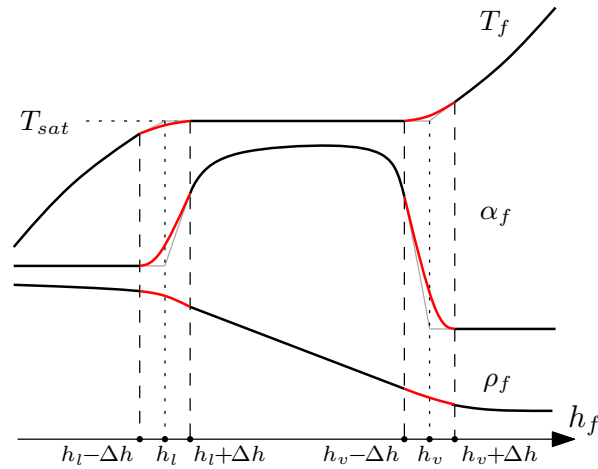


Figure 2.3: Smoothed temperature, heat transfer coefficient and density of the working fluid using cubic interpolation functions.

The smoothing is performed using cubic functions around an enthalpy range given by Δh . The enthalpy range Δh is a positive value, upper limited by the critical pressure such that the two interpolation cubic functions do not overlap. The first reason of the smoothing is to become more in line with the experiments due to imperfect fluid mixing at the saturation boundaries. The second reason is to avoid discontinuities in the working fluid enthalpy derivative during a phase change, which can lead to chattering phenomena. More details regarding the working fluid properties are given in Appendix A.1.

2.3.3 Non-dimensional analysis

In what follows, we bring the system to a non-dimensional form by means of scale analysis. Scale analysis has several advantages: it gives an indication of the important parts of an equation, reduces the number of free parameters while it avoids numerical difficulties.

To non-dimensionalize the system of equations, we first identify the independent and dependent variables. Second, we replace each of them with a quantity scaled relative to a characteristic unit of measure, i.e.,

$$\begin{aligned}
\text{independent variables: } t^* &= \frac{t}{t_{wg}^c}, \quad z^* = \frac{z}{L}; \\
\text{dependent variables: } h_f^* &= \frac{h_f}{h_f^c}, \quad h_g^* = \frac{h_g}{h_g^c}, \quad T_f^* = \frac{T_f}{T^c}, \quad T_g^* = \frac{T_g}{T^c}, \\
T_{wg}^* &= \frac{T_{wg}}{T^c}, \quad T_{wf}^* = \frac{T_{wf}}{T^c}, \quad \dot{m}_f^* = \frac{\dot{m}_f}{\dot{m}_f^c}, \quad \dot{m}_g^* = \frac{\dot{m}_g}{\dot{m}_g^c}, \\
\rho_f^* &= \frac{\rho_f}{\rho_f^c}, \quad \alpha_g^* = \frac{\alpha_g}{\alpha_g^c}, \quad \alpha_f^* = \frac{\alpha_f}{\alpha_f^c}, \quad \dot{Q}_{loss}^* = \frac{\dot{Q}_{loss}}{\dot{Q}_{loss}^c}.
\end{aligned} \tag{2.11}$$

Next, choose

$$\begin{aligned}
t_g^c &= \frac{\rho_g V_g}{\dot{m}_g^c}, \quad t_f^c = \frac{\rho_f V_f}{\dot{m}_f^c}, \quad t_{wg}^c = \frac{\rho_w c_{pw} \gamma_w V_w}{\dot{m}_g^c c_{pg}}, \quad t_{wf}^c = \frac{\rho_w c_{pw} (1 - \gamma_w) V_w T^c}{\dot{m}_f^c h_f^c}, \\
\alpha_g^c &= \frac{\dot{m}_g^c c_{pg}}{S_g}, \quad \alpha_f^c = \frac{\dot{m}_f^c h_f^c}{S_f T^c}, \quad \dot{Q}_{loss}^c = \dot{m}_g^c c_{pg} T^c.
\end{aligned} \tag{2.12}$$

Then, the mass and energy conservation equations become:

Conservation of mass (working fluid):

$$R_1^* \frac{\partial \rho_f^*}{\partial t^*} + \frac{\partial \dot{m}_f^*}{\partial z^*} = 0, \tag{2.13}$$

Conservation of energy:

$$R_2^* \frac{\partial T_g^*}{\partial t^*} = \dot{m}_g^* \frac{\partial T_g^*}{\partial z^*} - \alpha_g^* (T_g^* - T_{wg}^*) - \dot{Q}_{loss}^*, \tag{2.14a}$$

$$\rho_f^* R_1^* \frac{\partial h_f^*}{\partial t^*} = -\dot{m}_f^* \frac{\partial h_f^*}{\partial z^*} + \alpha_f^* (T_{wf}^* - T_f^*), \tag{2.14b}$$

Conservation of energy at the wall:

$$\frac{\partial T_{wg}^*}{\partial t^*} = \alpha_g^* (T_g^* - T_{wg}^*) - C_1^* (T_{wg}^* - T_{wf}^*), \tag{2.15a}$$

$$R_3^* \frac{\partial T_{wf}^*}{\partial t^*} = -\alpha_f^* (T_{wf}^* - T_f^*) + C_2^* (T_{wg}^* - T_{wf}^*), \tag{2.15b}$$

where

$$R_1^* = \frac{t_f^c}{t_{wg}^c}, \quad R_2^* = \frac{t_g^c}{t_{wg}^c}, \quad R_3^* = \frac{t_{wf}^c}{t_{wg}^c}, \quad C_1^* = \frac{1}{\dot{m}_g^c c_{pg}} \frac{\lambda_w S_w}{\delta_w}, \quad C_2^* = \frac{T^c}{\dot{m}_f^c h_f^c} \frac{\lambda_w S_w}{\delta_w} \tag{2.16}$$

In (2.12), the time constants t_g^c and t_f^c are the residence times. These values are the average amount of time that a particle from the exhaust gas or working fluid travels the complete heat exchanger length. For the wall, t_{wg}^c and t_{wf}^c are the heating-up and cooling-down time constants.

Remark 2.3.2. *Note that the choice of dimensionless parameters is not unique. A different choice of dimensionless parameters results in a similar system representation that differs only in scale. Here, we have chosen the constants h_f^c , h_g^c , T_c , \dot{m}_f^c , \dot{m}_g^c and ρ_f^c as the maximum values the system can reach inside the operating window.*

Table 2.1: Heat exchanger time constants

Parameter	Time [s]	Type
t_{wg}^c	28	constant
t_{wf}^c	13	constant
t_g^c	0.3	constant
t_f^c	[0.2, 8]	variable

For this particular heat exchanger, the time constants from (2.12) are numerically given in Table 2.1. While t_{wg}^c , t_{wf}^c and t_g^c are constant, t_f^c is variable. The working fluid time constant t_f^c varies due to the change in density along the heat exchanger length. It starts from 8 s in liquid phase and decreases to 0.2 s for the working fluid in vapor phase. The objective is to develop a numerically stable model with low computational complexity that fits typical Electronic Control Units (ECU) specifications. To accomplish this, we neglect the exhaust gas dynamics since t_g^c is significantly small compared to the wall time constant t_{wg}^c . Thus, the energy conservation for the exhaust gas side becomes:

$$0 = \dot{m}_g^* \frac{\partial T_g^*}{\partial z^*} - \alpha_g^* (T_g^* - T_{wg}^*) - \dot{Q}_{loss}^*. \quad (2.17)$$

To illustrate that this simplification holds, experimental data is used in Section 2.5. The simplified dynamical behavior of the model is governed by a first order casing model, the working fluid and the wall dynamics. The resulting continuous-time heat exchanger model is given by (2.5), (2.13), (2.14b), (2.15) and (2.17).

2.4 Model discretization

In this section, the continuous-time heat exchanger model is discretized with respect to time and space based on a finite-difference approximation. For the space discretization, a staggered grid is used to calculate the heat flux from the exhaust gas to the wall and from the wall to the working fluid.

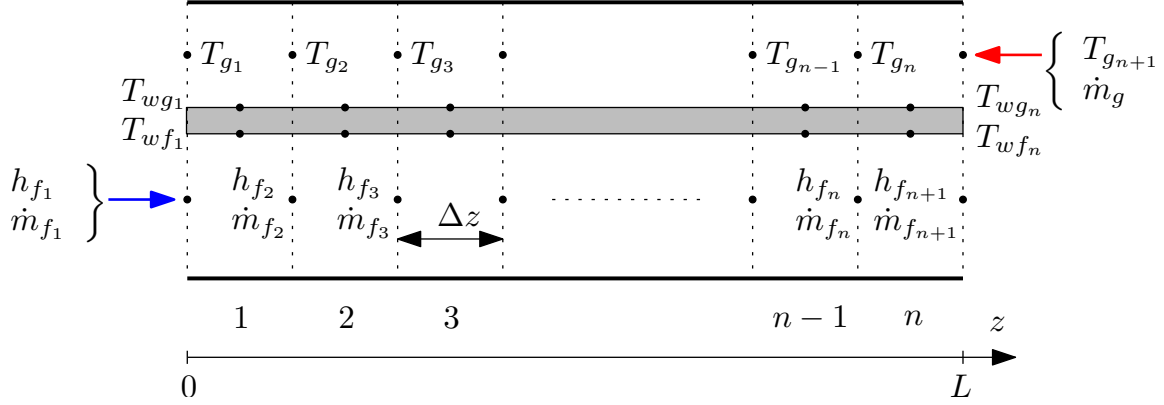


Figure 2.4: Staggered space discretization of the heat exchanger length.

First, as shown in Fig. 2.4, the heat exchanger fluid path is divided into n cells in which the mass conservation principle and energy conservation principle are applied. Note that the parameters (2.16) are adapted for one cell to incorporate Δz^* , resulting in a more simple expression for (2.13), (2.14b), (2.15) and (2.17). Thus, the mass balance Eq. (2.13) for each cell $i = 1, \dots, n$ is given by:

$$\dot{m}_{f_{i+1}}^* = \dot{m}_{f_i}^* - R_1^* \frac{d\rho_{f_i}^*}{dt}, \quad (2.18)$$

where $\rho_{f_i}^*$ is the non-dimensional density computed as function of the average enthalpy inside cell i .

Next, let us consider the following dimensionless average values in cell i : $\bar{T}_{g_i}^* = (T_{g_{i+1}}^* + T_{g_i}^*)/2$ for the exhaust gas temperature $\bar{T}_{f_i}^* = (T_{f_{i+1}}^* + T_{f_i}^*)/2$ for the working fluid temperature and $\bar{\alpha}_{f_i}^* = (\alpha_{f_{i+1}}^* + \alpha_{f_i}^*)/2$ for the working fluid heat transfer coefficient. The energy conservation for the exhaust gas (2.17) has a steady-state form, i.e.,

$$T_{g_i}^* = \frac{(2\dot{m}_g^* - \alpha_g^*)T_{g_{i+1}}^* + 2\alpha_g^*T_{wg_i}^* - 2\dot{Q}_{loss}^*}{2\dot{m}_g^* + \alpha_g^*}. \quad (2.19)$$

Note that in (2.19), the exhaust gas temperature profile is computed from right to left corresponding to the flow direction of the fluid.

The conservation of energy for the working fluid and at the wall can be written in discrete-space form as

$$\frac{dh_{f_{i+1}}^*}{dt^*} = \frac{1}{\bar{\rho}_f^* R_1^*} \left(-\dot{m}_{f_i}^* (h_{f_{i+1}}^* - h_{f_i}^*) + \bar{\alpha}_{f_i}^* (T_{wf_i}^* - \bar{T}_{f_i}^*) \right), \quad (2.20a)$$

$$\frac{dT_{wg_i}^*}{dt^*} = \alpha_g^* (\bar{T}_{g_i}^* - T_{wg_i}^*) - C_1^* (T_{wg_i}^* - T_{wf_i}^*), \quad (2.20b)$$

$$\frac{dT_{wf_i}^*}{dt^*} = \frac{1}{R_3^*} \left(-\bar{\alpha}_{f_i}^* (\bar{T}_{wf_i}^* - T_{f_i}^*) + C_2^* (T_{wg_i}^* - T_{wf_i}^*) \right). \quad (2.20c)$$

In (2.20a), we choose to approximate the working fluid density inside the heat exchanger using $\bar{\rho}_f^* = (1/n) \sum_{i=1}^n \rho_{f_i}^*$.

Second, the continuous-time set of Eq. (2.20a), (2.20b) and (2.20c) are discretized in time based on a forward Euler approximation. For simplicity, let us denote:

$$x_i^* = \begin{bmatrix} h_{f_{i+1}}^* \\ T_{wg_i}^* \\ T_{wf_i}^* \end{bmatrix}, \quad \phi_i^*(x_i^*, x_{i-1}^*) = \frac{dx_i^*}{dt^*}, \quad i = 1, \dots, n. \quad (2.21)$$

Then, the one-step ahead system state $x_i^*(k+1)$ can be approximated using a forward Euler scheme as:

$$x_i^*(k+1) = x_i^*(k) + t_s^* \phi_i^*(x_i^*(k), x_{i-1}^*(k)), \quad i = 1, \dots, n, \quad (2.22)$$

where t_s^* is a dimensionless sampling rate defined as $t_s^* = t_s/t_{wg}^c$.

2.4.1 Phase-change detection

When modeling two-phase flow heat exchangers, the dynamic information of liquid and vapor region length is of interest for control and heat exchanger performance analysis. However, due to space-discretization of the partial differential Eqs. (2.13) and (2.14b), (2.15a) and (2.15b) and (2.17), these regions have to be computed algebraically. To address this problem a phase-change detection routine is implemented. As shown in Fig. 2.5, the phase-change detection finds the crossing point inside a cell i based on the current state information $h_{f_i}^*$ and $h_{f_{i+1}}^*$.

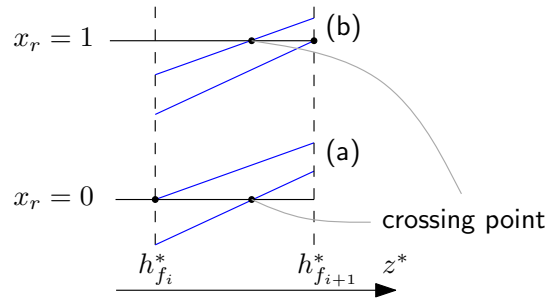


Figure 2.5: Representation of two different phase-change detection situations:
(a) From liquid to two-phase, (b) From two-phase to vapor.

Fig. 2.5 shows the crossing point detection for a heating-up process. For a cooling-down process a similar approach is employed. As in the MB method also in the phase-change detection routine, the aim is to find the crossing point position (see Fig. 2.5).

However, this becomes more challenging for modular heat exchangers due to multiple phase transitions in a single flow. As a solution, the phase-change detection considers the existence of a phase change in each cell and thus is applicable for modular heat exchangers with multiple phase transitions. It can detect a finite number of phase transitions according to the number of discretization cells. By using a larger number of discretization cells, the accuracy of the algorithm is improved.

2.4.2 Model verification

To verify and show the two-phase model capabilities, three consecutive steps in the exhaust gas heat flow rate are simulated. The normalized inlet exhaust gas temperature is kept constant at $T_{g,in}^* = 1.6$ while the exhaust gas mass flow rate is varied stepwise from $\dot{m}_g^* = 0.6$ to $\dot{m}_g^* = 0.7$ and finally to $\dot{m}_g^* = 0.34$. This corresponds to 55 kW, 65 kW and 32 kW, respectively, thermal power available on the exhaust gas side. The initial condition of the wall and working fluid temperature is chosen equal to the ambient temperature of 22 °C. The boundary condition for the working fluid side is chosen to be constant: normalized working fluid mass flow $\dot{m}_f^* = 0.5$, inlet normalized working fluid temperature $T_{f,in}^* = 0.6$, and normalized working fluid pressure $p_f^* = 0.4$. The working fluid boundary condition is chosen such that vapor is obtained at the heat exchanger outlet for the first 55 kW exhaust gas heat flow rate to show a heat-up simulation from ambient condition.

Fig. 2.6 shows the outlet working fluid and exhaust gas temperature evolution and the vapor ratio of the working fluid. As expected, the working fluid runs through all three regions, liquid, two-phase and vapor, during the heat-up phase (0-100 seconds). Then, between 200 and 400 s, the working fluid temperature reaches a new steady-state value, in the super-heated region, due to an increased exhaust gas heat flow rate. At 400 s, the step applied in the exhaust gas heat flow rate is no longer sufficient to generate vapor at the heat exchanger outlet. Thus, the working fluid goes into the two-phase region where the working fluid temperature is constant and equal to the saturation temperature (see Fig. 2.6). This is also indicated by the vapor ratio χ_r between 0 and 1 at the heat exchanger outlet.

In Fig. 2.7 the saturated liquid and saturated vapor boundaries inside the evaporators are given. These boundaries are in correspondence with the vapor ratio (see Fig. 2.6): when $\chi_r \leq 0$, no boundary is present; when $0 < \chi_r < 1$, only the liquid boundary is present; and in case $\chi_r \geq 1$, both boundaries are present. Furthermore, due to the heat exchanger modular design, the boundaries appear to be non-smooth when passing from

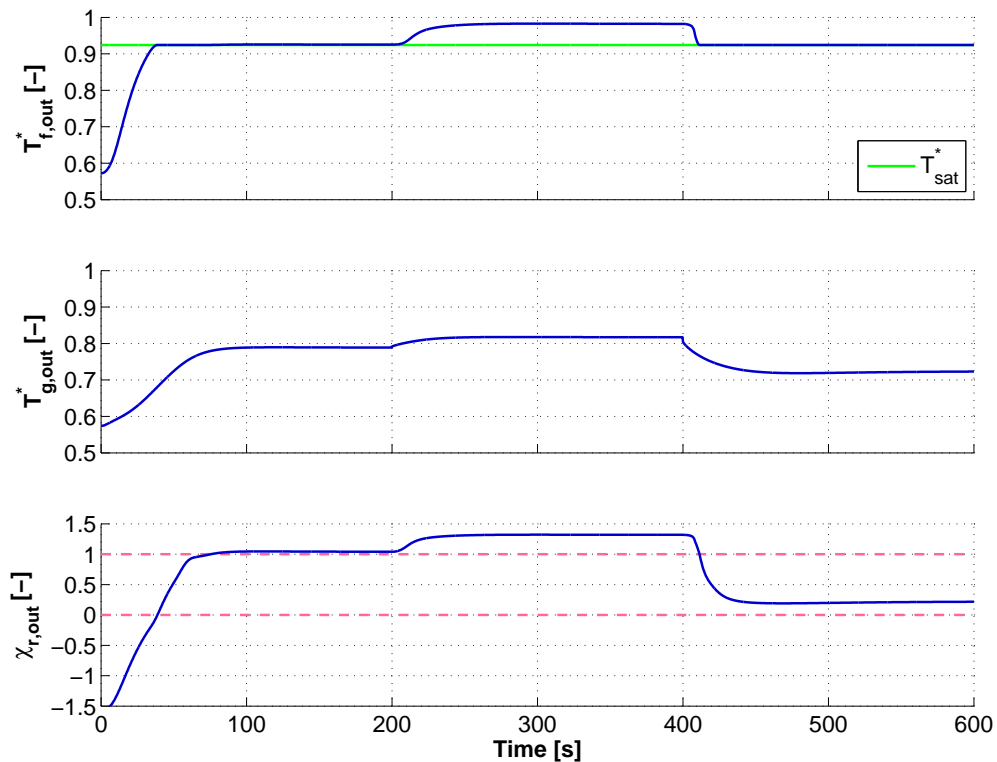


Figure 2.6: Normalized outlet working fluid temperature, exhaust gas temperature and working fluid vapor ratio during three consecutive steps in the exhaust gas heat flow rate.

one module to another. The effect is expected since the heat flux from the exhaust gas to the working fluid differs for each module.

In Fig. 2.8, the heat flow rate on both the working fluid side and exhaust gas side including losses are shown. As expected, the exhaust gas heat flow rate including losses, equals the working fluid heat flow rate as the system reaches steady state. Furthermore, the mass balance on the working fluid side is shown to be satisfied. On top of that, for transients conditions the outlet working fluid mass flow increases during heating and decreases during cooling.

The next section is dedicated to the experimental validation of the EGR heat exchanger model.

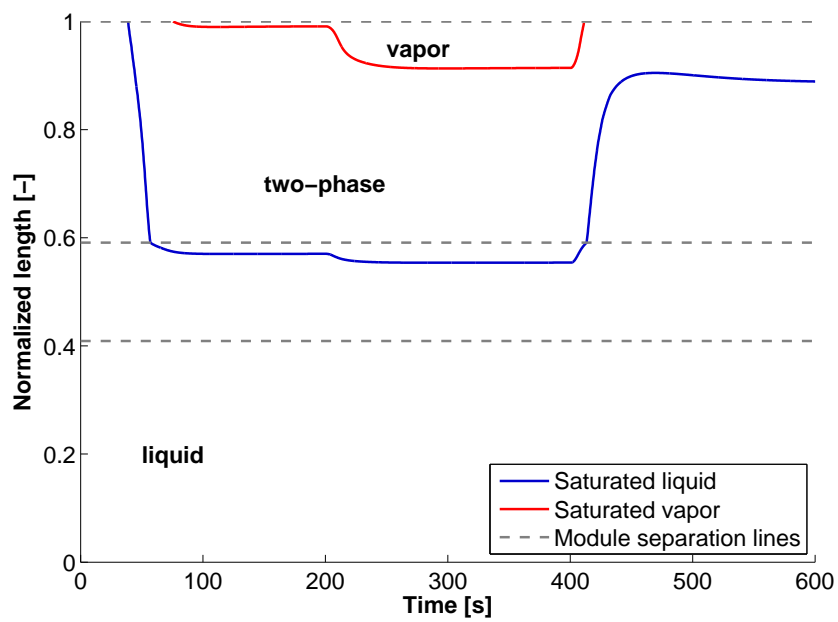


Figure 2.7: Normalized liquid and vapor boundaries.

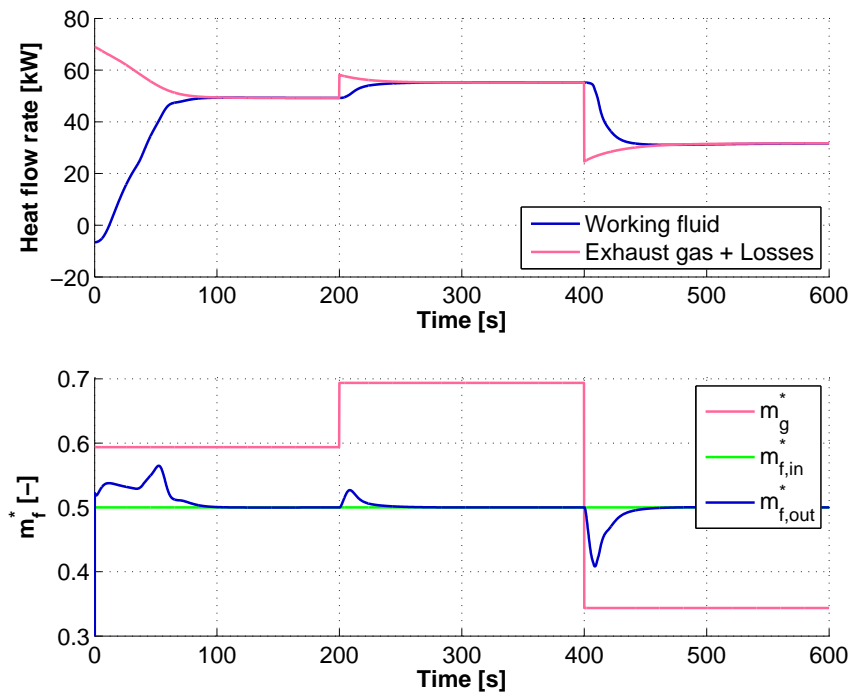


Figure 2.8: Heat flow rate and normalized mass balance.

2.5 Experimental validation

In this section, we verify the overall energy balance for the measurements, followed by the heat exchanger model validation. The energy balance is necessary to verify the measurements correctness. For stationary conditions, the energy equations are:

$$\dot{Q}_g = \dot{m}_g c_{pg} (T_{g,in} - T_{g,out}), \quad (2.23a)$$

$$\dot{Q}_f = \dot{m}_f (h_{f,out} - h_{f,in}). \quad (2.23b)$$

In the ideal case where no losses are present $\dot{Q}_g = \dot{Q}_f$ in steady-state. A disagreement between \dot{Q}_g and \dot{Q}_f is an indicator for heat losses or for possible errors in the measurement system. From (2.4), the calculated heat losses $\dot{Q}_{loss,ss}$ appear to be small, between 100 and 400 W as a consequence of the good heat exchanger insulation. However, from the measurements, see Fig. 2.9, the energy imbalance between \dot{Q}_g and \dot{Q}_f is more significant, up to 6 kW. This requires closer analysis since it can induce a large error between the measured temperatures and the model prediction.

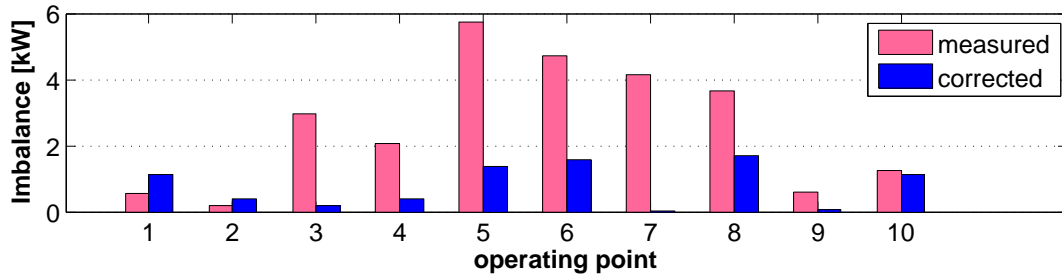


Figure 2.9: Energy imbalance for different operating conditions.

In steady-state, the energy imbalance observed for the experiments can be due to several factors: inaccuracies in exhaust gas and working fluid properties and measurement errors. The exhaust gas properties are related to the heat capacity, which is considered to be constant in (2.23), but the exhaust gas heat capacity varies with temperature. However, within the temperature window that the system operates only 2% error in the computed energy is induced by taking a constant heat capacity. Furthermore, the working fluid property equations used to compute the enthalpy are not exact but approximate the working fluid used within the experimental set-up. The above reasons did not explain the imbalance. Further investigations revealed that the energy imbalance was mainly due to mass flow measurement errors. The mass flow sensors, on the working fluid and exhaust side, were determined to have large systematic error for high mass flow rates that correspond to a high heat flow rate. This is mainly caused by the

pulsating flow as a consequence of the pumping behavior on both the working fluid side and engine side. To account for these effects, data reconciliation techniques [57] can be used. These techniques consider the correction of the measured values, such as mass flow rate, by minimizing a least-square error objective function subject to the energy conservation principles (2.23). The resulting mass flow correction for the exhaust gas side and working fluid side are:

$$\dot{m}_g^c = c_1 \dot{m}_g + c_2, \quad \dot{m}_f^c = c_3 \dot{m}_f + c_4, \quad (2.24)$$

where c_1, c_3 are the gain and c_2, c_4 are the offset mass flow corrections, respectively. Fig. 2.9 shows that the mass flow corrections lead to an improved energy balance. Using these corrections, the remaining maximum error reduces to 2 kW.

Note that the problem considered is dynamic, while the mass flow corrections, (2.24), based on an energy balance, (2.23), are in steady-state. Certainly, also the mass flow sensor dynamic response is important for accurate measurements. However, a direct assessment of the sensor dynamics was not possible. Indirectly it follows from calibration, that this was not a significant effect. Moreover, based on the simulation results, we show that using (2.24) produces acceptable results also during transients.

The model validation is performed using measured data from a Euro VI heavy-duty diesel engine. Note that different data sets are used for energy balance correction and for the model validation. The data sets used for model validation cover the complete engine operating condition. The first data set consists of several operating points obtained by changing the engine load step-wise. The second data set is a World Harmonized Transient Cycle (WHTC) [58], used to validate the model for normal driving, during cold-start and hot-start conditions. The focus is on verifying the model accuracy regarding the working fluid temperature, vapor ratio and exhaust gas temperature and on confirming that objectives (i)-(iii) are fulfilled.

In Fig. 2.10, input signals of the first data set are shown. These were recorded by running the engine, with standard Euro-VI calibration, in different operating conditions over the engine speed range of 1200-1850 rpm and engine torque range of 500-2600 Nm.

Initially, the engine is warm and vapor is generated at the heat exchanger outlet. The simulation results in comparison with experimental data are given in Fig. 2.11. The working fluid, exhaust gas outlet temperatures, and vapor ratio describe well the measurements over the complete operating range. Since the instrumentation to measure the vapor ratio χ_r was not available, the vapor ratio is calculated based on the working fluid temperature and pressure measurements. However, this calculation can be performed only in the liquid region and vapor region, where the working fluid

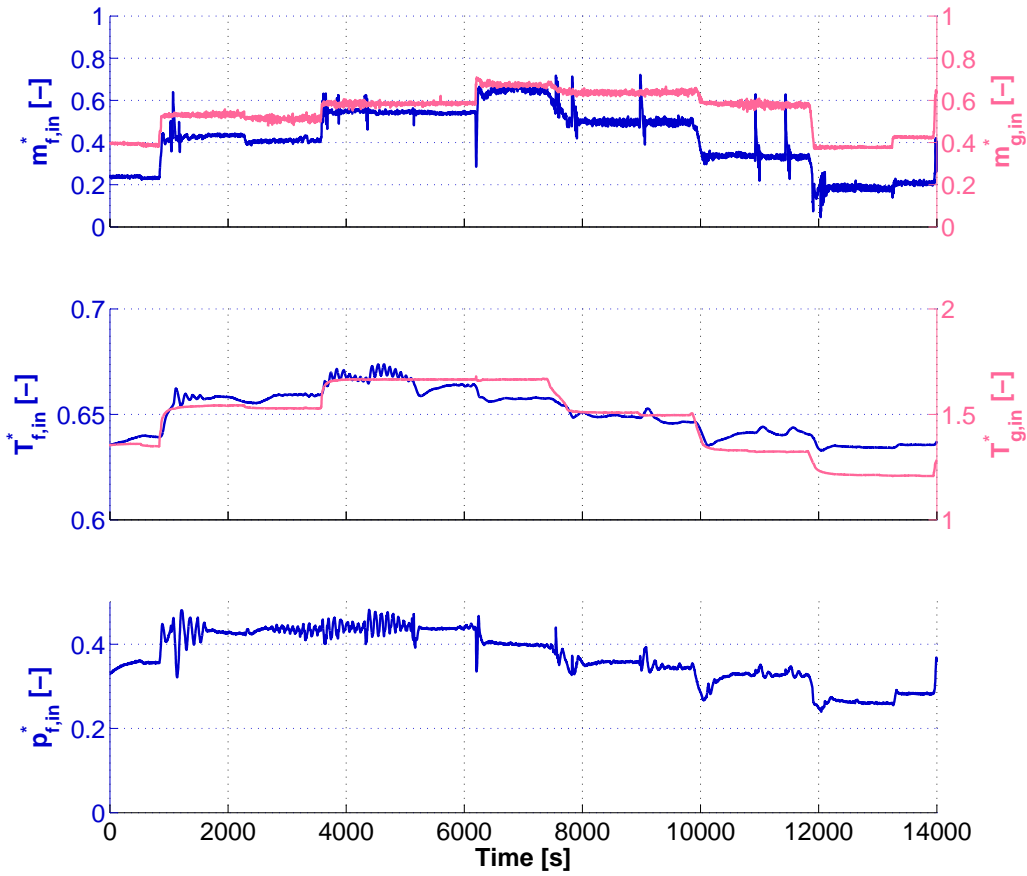


Figure 2.10: Experimental input signals.

temperature is not saturated. Therefore, a comparison in the two-phase region is not possible.

At 6200 s (see Fig. 2.11), an increase in the working fluid and exhaust gas temperature is present. This increase in both temperatures is caused by a rapid descend in working fluid mass flow during an increase in the exhaust gas mass flow from the engine (see Fig. 2.10).

The prediction errors are computed as follows. Let the temperature from simulation and measurement in Kelvin be T_{sim} and T_{meas} , respectively. The error in percentage for both the working fluid side and exhaust side is defined as:

$$e = 100 \cdot \frac{|T_{sim} - T_{meas}|}{|T_{in} - T_{out}|_{max}}, \quad (2.25)$$

where $|T_{sim} - T_{meas}|$ is the absolute error and $|T_{in} - T_{out}|_{max}$ is the temperature difference over the heat exchanger at maximum thermal load. For the working fluid side, the

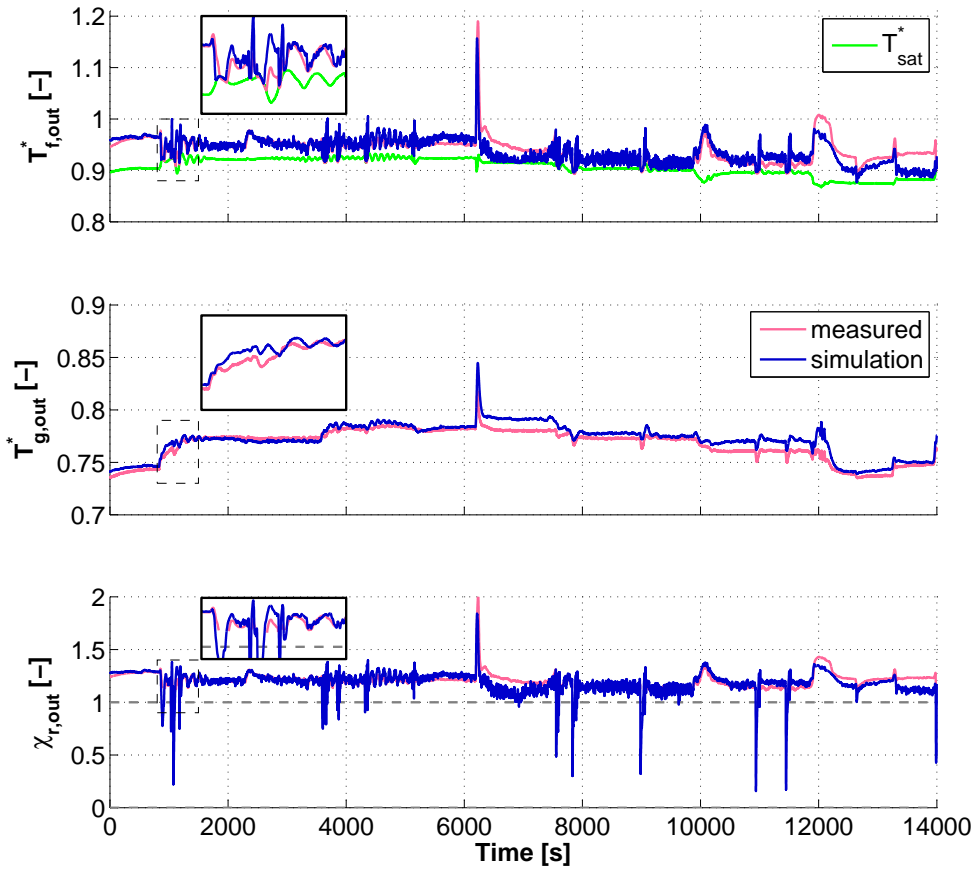


Figure 2.11: Working fluid temperature, exhaust gas temperature and vapor ratio in comparison with measurements.

temperature difference at maximum thermal load corresponds to 215 K, and for the exhaust gas side to 450 K, respectively. Note that (2.25) is still valid in case normalized temperature values (2.11) are used.

The mean absolute error for steady-state conditions is 6 K for the working fluid side and 3 K for the exhaust gas side. This corresponds to 2.8% and 0.7% relative error on the working fluid side and exhaust gas side, respectively. The maximum deviation in steady-state is 23 K for the working fluid side and 12 K for the exhaust gas side, corresponding to 10.7% and 2.7%, respectively. Primarily, this is a consequence of the uncertainties in the measurements, which still results in an energy imbalance of up to 2 kW. For low heat flows, the energy imbalance represents approximately 10% of the energy up-take from the exhaust gas. As a consequence, the temperature prediction can be worse for low heat flow rates. For instance in case of a 20 kW transferred heat

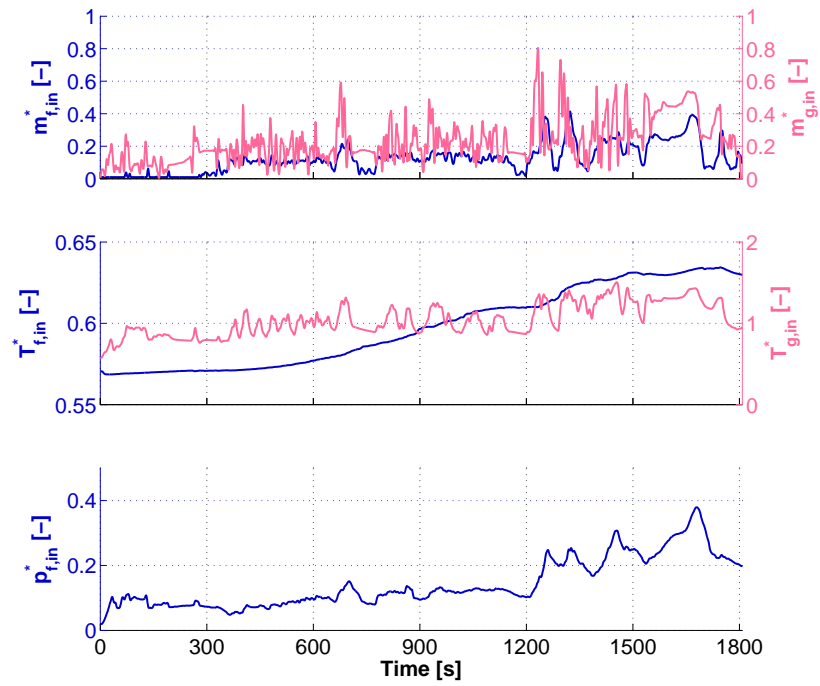
with an energy imbalance of 2 kW on the working fluid side, results in a working fluid temperature prediction error of approximately 45 K.

The modeling uncertainties, for instance the working fluid properties and heat transfer coefficient, also play a role for model accuracy. As can be seen between 6000-8000 s and 12000-14000 s, that a slightly higher heat transfer coefficient would improve the results. From a dynamical point of view, incorporating conduction in the casing, especially between modules, might improve the model accuracy during transients. Thus, using a more accurate measurement system, heat transfer coefficient for plates instead of tubes and conduction in the casing, can lead to more accurate results. The error induced due to numerical approximation is small compared to the error due to modeling uncertainties. Reducing the sample time and increasing the number of cells does not significantly improve the results.

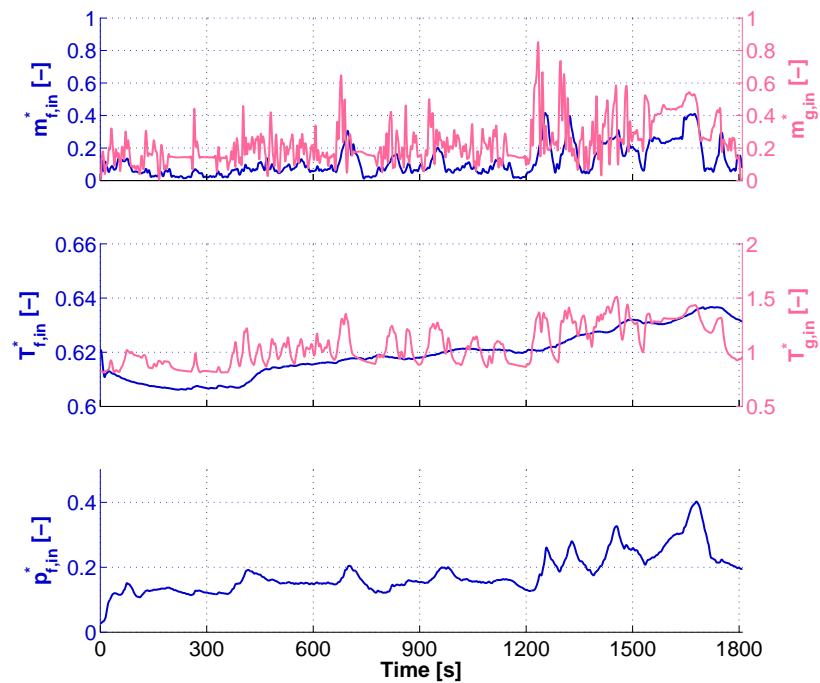
To validate the model for representative real-world driving conditions, we use a standard WHTC during cold-start and hot-start. The WHTC type approval cycle is a transient test of 1800 s that covers typical driving conditions: urban, rural and highway. This cycle generates in terms of mass flows, temperatures and pressure the input data shown in Fig. 2.12a and in Fig. 2.12b during cold-start and hot-start, respectively. On the exhaust gas side, the mass flow responds almost immediately, while the temperature has a first order behavior with a time constant of approximately 16 s. Furthermore, on the working fluid side, slower dynamic behavior can be seen for the mass flow rate, temperature and pressure in the system.

The simulation results for the cold-start and hot-start WHTC are given in Fig. 2.13a and in Fig. 2.13b, respectively. Note that the instrumentation to measure the vapor ratio χ_r was not available. In the liquid and vapor region, the vapor ratio χ_r is calculated from (2.10) based on measured working fluid temperature and pressure. In the two-phase region, the measured temperature equals the saturation temperature, while having no information about the vapor ratio. Thus, a direct comparison of the vapor ratio with respect to the measurements is not possible. However, using a highly dynamic test cycle, the working fluid at the heat exchanger outlet switches between the two-phase and the vapor region repeatedly. From the simulation results, the moment of switching between these two regions is well described (see Fig. 2.13). This is important for a control strategy that needs to guarantee safe system operation.

For the cold-start WHTC the ambient initial condition is used. First, regarding the fast dynamic capabilities during normal operating conditions, namely after 1200 s within the WHTC, the model gives good results with respect to the measurements. Dynamic behavior of the working fluid temperature, exhaust gas temperature and vapor ratio are

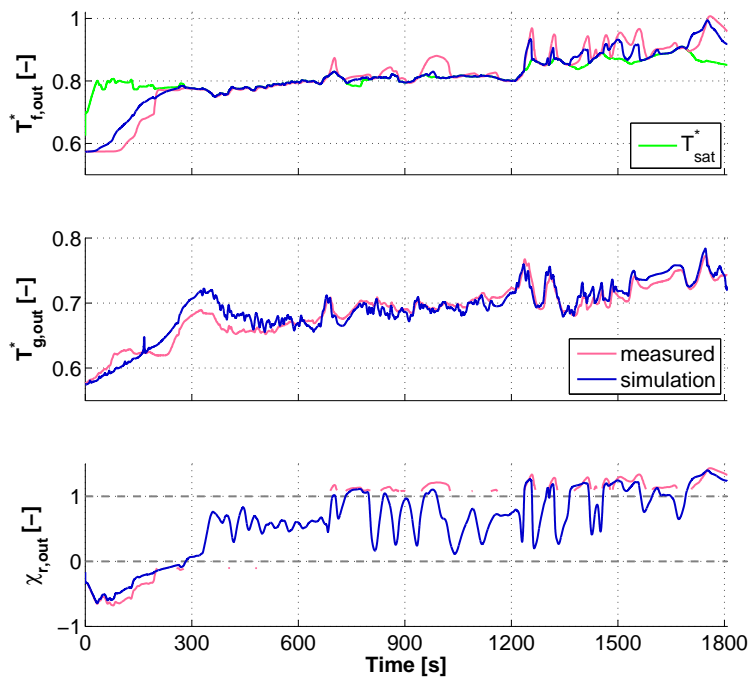


(a)

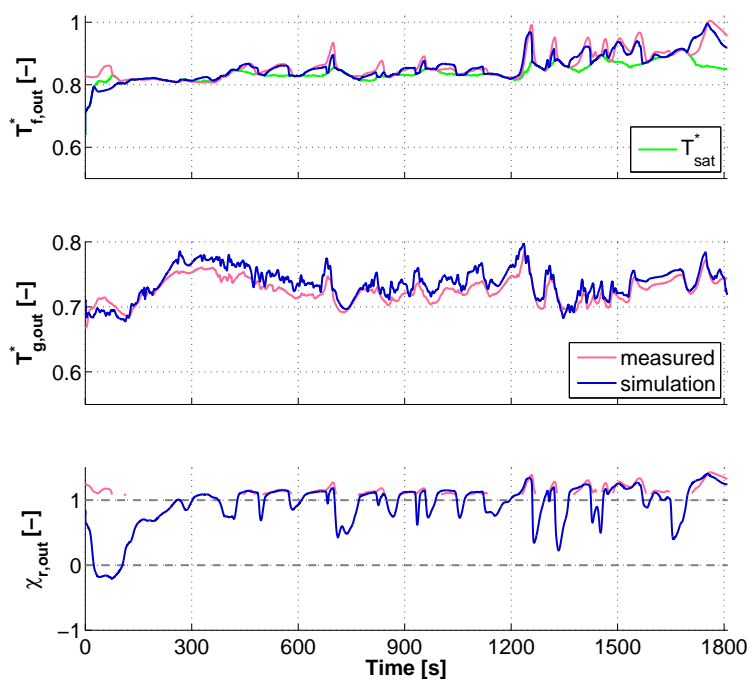


(b)

Figure 2.12: (a) Experimental input signals from a cold-start WHTC. (b) Experimental input signals from a hot-start WHTC.



(a)



(b)

Figure 2.13: (a) Normalized working fluid temperature, exhaust gas temperature and vapor ratio for the cold-start WHTC. (b) Normalized working fluid temperature, exhaust gas temperature for the hot-start WHTC.

well captured. Second, the model shows that during the heating-up process, between 200 and 400 s, the working fluid temperature rises more rapidly in comparison with the measurement. As a consequence of the energy conservation principle, also the exhaust gas temperature shows a slight disagreement with the measurements. This effect is mainly caused by the casing material for which a simple first order model was used. The result can therefore be improved, by including a more accurate heat loss model for the casing. However, for a long haul application, the start-up appears for a very limited time, typically only 6-7 min (see Fig. 2.13a), compared to the complete operation time, which is in the order of hours. In practice, the start-up can be accommodated in the controller design using for instance a start-up procedure to bring the system from a cold condition to a state close to the desired operating condition. Another controller that is designed for normal operating conditions can be activated from that point.

For the hot-start WHTC, in terms of accuracy, the results are similar to the cold-start WHTC. Note however, that the model initial condition is challenging to choose, since the system is not in steady-state and the current state for the real system is unknown. This results in a less accurate solution for the first 100 s (see Fig. 2.13b). In contrast with a non-modular heat exchanger, where the liquid and vapor boundaries appear once as a function of time, in a modular heat exchanger multiple phase transitions can be present. Fig. 2.14 shows the model capabilities to capture multiple phase transitions in single flow. Between 100 and 300 s, is the most prominent time interval where multiple liquid to two-phase transitions are encountered. Similarly, multiple two-phase to vapor transitions can be present, however, they are less visible due to high fluid velocities. In general, these transitions appear during transients and vanish as the system reaches its steady-state value.

For highly dynamic conditions, the model describes the real system well: working fluid temperature error is below 40 K with vapor ratio well captured and exhaust gas temperature error is below 20 K for the complete operating range. This result is obtained despite the accuracy of the experimental data that can lead to working fluid temperature errors up to 45 K. Thus, the model complies with the proposed objectives (i)-(iii), for WHR system safe operation, control design and emission management, respectively.

In Table. 2.2, the maximum and average model prediction error is summarized for steady state and dynamic conditions.

Regarding computational complexity, the model computational time is approximately 300 times less as compared to the measurements time length. The results were obtained by running the discrete heat exchanger model with 22 cells and a sampling time of 0.2 s

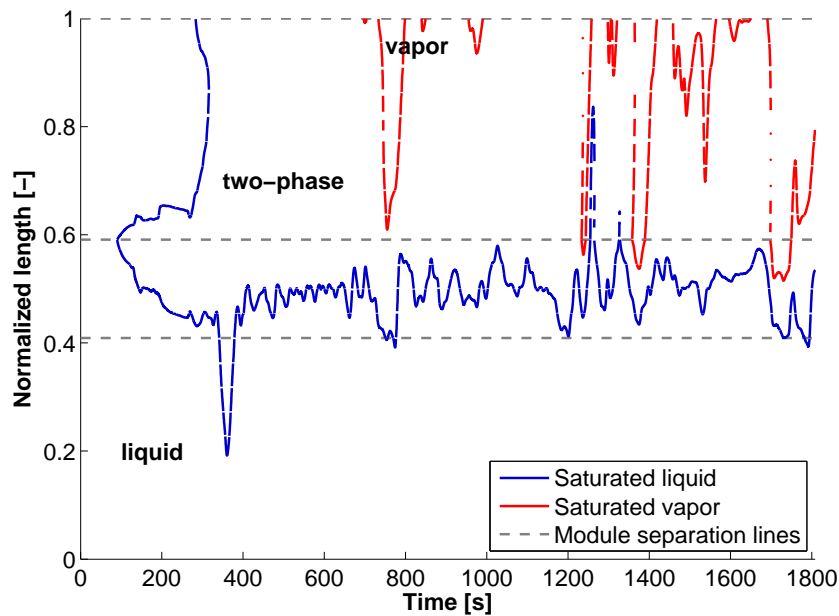


Figure 2.14: Normalized liquid and vapor boundaries for WHTC cold-start.

Table 2.2: Summary of the model prediction error

	Working fluid		Exhaust gas	
	Maximum	Average	Maximum	Average
Steady state	23 K (10.7%)	6 K (2.8%)	12 K (2.7%)	3 K (0.7%)
Dynamic	37 K (17.2%)	8 K (3.7%)	19 K (4.2%)	5 K (1.1%)

on a Lenovo laptop with Windows 7, Matlab 2012a and 2 GHz quad-core processor. The simulation results show that overall a good agreement between the model and experiments is obtained while computational complexity is low.

2.6 Conclusions

A dynamic model of a modular two-phase heat exchanger for waste heat recovery in diesel engines was developed. The studied waste heat recovery system recovers energy from both the exhaust gas recirculation line and main exhaust line. In this study, the modular heat exchanger was described in detail based on the mass and energy balance equations. The model was brought into a non-dimensional form to reduce the number of free parameters while avoiding numerical difficulties. The resulting representation was discretized in time and space using a finite difference and a staggered

grid approach. Compared to other heat exchanger models, the model developed in this chapter combines the finite difference method with the moving boundary modeling approach. Thus, it captures the dynamics of multiple phase transition caused by the modular heat exchanger design. The model was validated on data from a state-of-the-art Euro-VI heavy-duty diesel engine equipped with a waste heat recovery system. The validation was performed on two data sets: transitions between steady-state points that cover the complete engine operating area and a highly dynamic world harmonized transient cycle for both cold-start and hot-start conditions. From the simulation results, it is concluded that the model is a good representation of the real system capable to predict the working fluid and exhaust gas temperature with an average error of less than 4%.

The model developed in this chapter will be first included in a complete waste heat recovery system model. The complete model will be used to develop low-level control strategies that optimize the waste heat recovery system power output within safe operation limits. Second, the supervisory control strategy [32] will be further developed and implemented on the studied engine.

Modeling and control of a parallel waste heat recovery system¹

Abstract This chapter presents the modeling and control of a waste heat recovery system for a Euro-VI heavy-duty truck engine. The considered waste heat recovery system consists of two parallel evaporators with expander and pumps mechanically coupled to the engine crankshaft. Compared to previous work, the waste heat recovery system modeling is improved by including evaporator models that combine the finite difference modeling approach with a moving boundary one. Over a specific cycle, the steady-state and dynamic temperature prediction accuracy improved on average by 2% and 7%. From a control design perspective, the objective is to maximize the waste heat recovery system output power. However, for safe system operation, the vapor state needs to be maintained before the expander under highly dynamic engine disturbances. To achieve this, a switching model predictive control strategy is developed. The proposed control strategy performance is demonstrated using the high-fidelity waste heat recovery system model subject to measured disturbances from an Euro-VI heavy-duty diesel engine. Simulations are performed using a cold-start World Harmonized Transient cycle that covers typical urban, rural and highway driving conditions. The model predictive control strategy provides 15% more time in vapor and recovered thermal energy than a classical proportional-integral (PI) control strategy. In the case that the model is accurately known, the proposed control strategy performance can be improved by 10% in terms of time in vapor and recovered thermal energy. This is demonstrated with an offline nonlinear model predictive control strategy.

¹This chapter is based on [41].

3.1 Introduction

Nowadays, the primary power source for transportation is provided by internal combustion engines. Despite efforts to improve fuel economy in modern engines, approximately 60%–70% of the fuel power is still lost through the coolant and exhaust [29]. Moreover, the upcoming CO₂ emission legislation needs to be fulfilled. For heavy-duty vehicles, USA legislation indicates a 20% CO₂ emissions reduction by 2020. In Europe, similar requirements are expected to be introduced. To meet these upcoming CO₂ regulations and further reduce fuel consumption, diesel engines equipped with waste heat recovery (WHR) systems based on an organic Rankine cycle (ORC) seem very promising [35, 46, 59], especially for long-haul heavy-duty truck applications [49, 50]. A WHR system allows energy to be recovered from the exhaust gas to generate mechanical power useful for propulsion.

For automotive applications, control of WHR systems is challenging. This is due to highly dynamic engine conditions, to interaction between the engine and the WHR system and to constraints, namely actuator limitations and safe operation. The control strategies dedicated to automotive applications are mostly based on a proportional-integral-derivative (PID) control type of approach [21, 27, 28, 30, 31, 33]. However, this approach is most well established for single-input single-output systems. For multiple-input multiple-output systems with constraints, a model predictive control (MPC) can be developed, which, to the authors knowledge, has not been used for automotive WHR applications. Predictive control has been applied only to power plants [34, 52] and refrigeration systems [36]. The main difference is that power plants and refrigeration systems work at different time scales as compared to automotive WHR systems that are governed by highly dynamic engine behavior.

In this chapter, a switching model predictive control strategy is presented that considers the effect of highly dynamic engine disturbances caused by real on-road driving conditions. The WHR system is highly non-linear, mainly due to the two-phase flow phenomena. Thus, a global controller can give limited performance over the complete engine operating area. To account for this, a switching mechanism is developed that assigns a controller for a certain engine operating area. As a result, the control strategy allows operation close to the safety limit with good disturbance rejection properties. To benchmark the MPC strategy performance, a classical proportional-integral (PI) control strategy [43] is used, for comparison. Furthermore, an offline nonlinear MPC (NMPC) strategy is implemented to compare the MPC solution with the optimum solution in the case that the WHR system model is exactly known. The NMPC scheme is developed only for comparison purposes, since it is characterized by high computational

complexity, making it unsuitable for embedded applications using off-the-shelf hardware.

For control design and optimization, dynamical modeling of WHR systems plays an important role. In [42], a dynamical model of the complete WHR system has been developed. The model captures the two-phase flow phenomena based on the conservation principles of mass and energy. However, in [42], simple evaporator models were used with simplified heat transfer coefficients. To improve the accuracy of the WHR system model, more advanced evaporator models are included, based on the approach used in [39] for the exhaust gas recirculation (EGR) evaporator. This approach combines the finite difference modeling approach with a moving boundary one. Thus, it is able to capture multiple phase transitions along a single pipe flow.

This chapter is organized as follows. In Section 3.2, the experimental set-up is described. In Section 3.3, the improved WHR system model is presented and validated against the measurements. In Section 3.4, the control design and switching mechanism are presented. The control performance is evaluated in Section 3.5 by means of simulation results and comparison with a classical proportional-integral (PI) and NMPC control strategy. Conclusions and directions for future research are discussed in Section 3.6.

3.2 Experimental Set-Up

The experimental set-up is schematically illustrated in Figure 3.1. A six-cylinder Euro-VI European emission standards heavy-duty diesel engine is studied with an aftertreatment system that consists of: a diesel oxidation catalyst (DOC), diesel particulate filter (DPF), selective catalytic reduction (SCR) and an ammonia oxidation catalyst (AMOX). The engine is furthermore equipped with a WHR system that recovers heat from both the EGR line and main exhaust (EXH) line. The studied WHR system is based on a typical organic Rankine cycle (ORC) with pure ethanol as the working fluid. Ethanol is selected because of its physical and thermodynamic properties, which are suitable for this low temperature application. The ethanol is pumped from a reservoir at atmospheric pressure through plate-fin counter-flow evaporators, where it changes its state from liquid to two-phase and then vapor at the evaporator outlet. By expanding the vaporized ethanol, mechanical power is generated at the expander shaft. In this set-up, a two-piston expander is used that, according to the manufacturer data, can withstand ethanol in the two-phase state for short periods of time. To close the cycle, a condenser is used that brings the ethanol back to the liquid state. For safety reasons, a pressure relief valve is used that limits the system pressure to 60 bar.

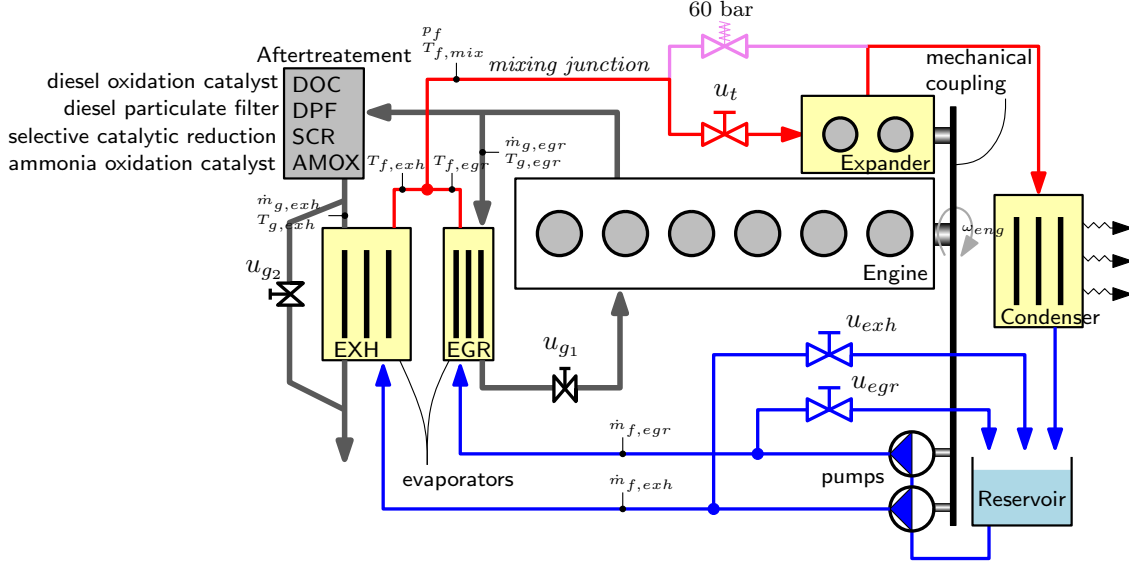


Figure 3.1: Schematic representation of the experimental set-up.

The measurement system consists of thermocouples to measure temperature and thin-film pressure sensors. The exhaust gas mass flow rate is measured using Coriolis flow meters, while the ethanol mass flow rate is measured using helicoidal flow meters. To test the system under various engine loads and rotational speeds, a dynamometer is connected to the engine. To minimize heat losses to the environment, the WHR system was insulated.

Note that in the studied system, the expander and the pumps are mechanically coupled to the engine crankshaft. A disadvantage of this design is that due to mechanical coupling, the pressure in the system can be restricted, and thus, the power of the WHR system becomes limited. The advantage is that the mechanical power is directly transmitted to the engine, without energy losses from a power converter or variable transmission. During gear shifting, when the requested power is less than the WHR system net output power, $P_{req} < P_{whr}$, a throttle valve is closed ($u_t = 0\%$) to avoid unwanted torque response. However, in this study, we focus only on the power mode (excluding gear shifting), and thus, the throttle valve is kept fully opened ($u_t = 100\%$).

To avoid droplets, *i.e.*, to guarantee the vapor state after the EGR evaporator and EXH evaporator, two bypass valves, u_{egr} and u_{exh} , are used. These bypass valves manipulate the ethanol flow rate, such that the vapor state is maintained after the evaporators in the presence of engine disturbances. On the exhaust gas side, the EGR valve u_{g1} is controlled using the standard calibration for a conventional engine. From the cooling perspective, a valve u_{g2} is used to bypass the exhaust gases at the EXH evaporator and, so, accommodates the maximum condenser cooling capacity.

3.3 Waste Heat Recovery System Modeling

The WHR system model is described using a component-based approach using first principle modeling. It consists of a reservoir, pumps, valves, evaporators, condenser and an expander model. The pumps and expander are map-based components, while the rest is modeled based on the conservation principles for mass and energy. The pipes, on the vapor side (indicated with red in Figure 3.1) are modeled as a compressible volume. The WHR system model is developed based on the following assumptions:

- the working fluid flows always in the positive direction;
- transport delays and pressure drops along the pipes are neglected;
- pressure drops along the evaporators are neglected on both the working fluid and exhaust gas side;
- the exhaust gas change in density along the evaporators is neglected;
- the condenser is ideal, so that the reservoir provides working fluid at the ambient pressure of 1 bar and a temperature of 65 °C.

Here, a brief review is given for the main components within the system, and more details can be found in [39, 42].

3.3.1 Pump

The WHR system is equipped with two identical pumps. The mass flow rate through a pump is computed based on the ideal mass flow rate and volumetric efficiency as:

$$\dot{m}_p = \dot{m}_{p,id} \eta_{vol} \quad (3.1)$$

where the volumetric efficiency $\eta_{vol} = f(\omega_p, p_r)$ is a function of pump speed ω_p (rev/s) and the pressure ratio across the pump p_r , according to the measurements. The ideal mass flow rate is given by:

$$\dot{m}_{p,id} = V_d \omega_p \rho \quad (3.2)$$

where V_d is the pump displacement volume and ρ is the working fluid density. The pump power is obtained using:

$$P_p = \dot{m}_p \frac{p_{out} - p_{in}}{\rho \eta_{is} \eta_{vol}} \quad (3.3)$$

where η_{is} is the isentropic efficiency and accounts for internal pump energy loss caused by friction and external thermal loss. Due to the low viscosity of ethanol, the isentropic

efficiency is assumed at the upper limit [60], *i.e.*, $\eta_{is} = 0.9$. The outgoing working fluid temperature is calculated based on the energy balance equation:

$$T_{p,out} = T_{p,in} + \frac{1 - \eta_{is}}{\dot{m}_p c_p} P_p \quad (3.4)$$

where $c_p = f(T_{p,in}, p_{in})$ is the specific heat capacity of the working fluid.

3.3.2 Valve

The valves within the WHR system are modeled as incompressible flow valves for flows in the liquid state and compressible flow valves for the two-phase and vapor flows. The thermodynamic state of the outgoing fluid is calculated assuming an isenthalpic process through the valve, *i.e.*, $h_{out} = h_{in}$.

Incompressible Flow Valve

The mass flow rate through the valve for incompressible flow is expressed as:

$$\dot{m}_{iv} = u_v c_d A_0 \sqrt{2\rho(p_{in} - p_{out})} \quad (3.5)$$

where u_v represents the duty cycle from 0 to 1 applied to the valve actuator, c_d is the discharge coefficient, A_0 is the orifice area and $p_{in} - p_{out}$ is the pressure difference across the valve.

Compressible Flow Valve

The compressible flow valve is modeled using:

$$\dot{m}_{cv} = u_v c_d A_0 \sqrt{\rho_{in} p_{in} \phi} \quad (3.6)$$

where ϕ is the compressibility coefficient defined as:

$$\phi = \frac{2\gamma}{\gamma - 1} \left(\psi^{\frac{2}{\gamma}} - \psi^{\frac{\gamma+1}{\gamma}} \right), \text{ with:} \quad (3.7)$$

$$\gamma = \frac{c_p}{c_v} \quad (3.8)$$

The parameter ψ has the following expression, whether the flow is subsonic or supersonic:

$$\psi = \begin{cases} \frac{p_{out}}{p_{in}} & \text{if } \frac{p_{out}}{p_{in}} > \left(\frac{2}{\gamma+1} \right)^{\frac{\gamma}{\gamma-1}} \text{ subsonic} \\ \left(\frac{2}{\gamma+1} \right)^{\frac{\gamma}{\gamma-1}} & \text{if } \frac{p_{out}}{p_{in}} \leq \left(\frac{2}{\gamma+1} \right)^{\frac{\gamma}{\gamma-1}} \text{ supersonic} \end{cases} \quad (3.9)$$

where $p_{\text{out}}/p_{\text{in}}$ is the pressure ratio across the valve and $\left(\frac{2}{\gamma+1}\right)^{\frac{\gamma}{\gamma-1}}$ is the critical pressure ratio.

3.3.3 Evaporator and Condenser

The thermal behavior of the WHR system is mainly influenced by the evaporators and condenser. Therefore, the modeling of these components plays a crucial role to describe the WHR system dynamic behavior [28]. The evaporators are plate-fin counter-flow heat exchangers in which the working fluid changes its state from liquid to two-phase and from two-phase to vapor [21]. Compared to [42], an improved model for the EGR evaporator is described in [39]. Here, we incorporate the enhanced EGR evaporator model and derive an EXH evaporator using a similar representation as in [39]. The enhanced evaporator model combines a finite difference modeling approach with a moving boundary one. Thus, it captures multiple phase transitions along a single pipe flow. To characterize the single-phase flow, as well as the two-phase flow phenomena, more advanced heat transfer coefficients are used, which improve the prediction accuracy of the exhaust gas and working fluid temperature in general. The evaporator model is based on the conservation principles of mass and energy. The time derivative of pressure is neglected, since the pressure dynamics are much faster than the thermal phenomena. As a result, the evaporator model can be written as the following set of partial differential equations:

Conservation of mass (working fluid):

$$V_f \frac{\partial \rho_f}{\partial t} + L \frac{\partial \dot{m}_f}{\partial z} = 0 \quad (3.10)$$

Conservation of energy:

$$\rho_g c_{pg} V_g \frac{\partial T_g}{\partial t} = c_{pg} \dot{m}_g L \frac{\partial T_g}{\partial z} - \alpha_g S_g (T_g - T_{wg}) - \dot{Q}_{\text{loss}} \quad (3.11a)$$

$$\rho_f V_f \frac{\partial h_f}{\partial t} = -\dot{m}_f L \frac{\partial h_f}{\partial z} + \alpha_f S_f (T_{wf} - T_f) \quad (3.11b)$$

Conservation of energy at the wall:

$$\rho_w c_{pw} \gamma_w V_w \frac{\partial T_{wg}}{\partial t} = \alpha_g S_g (T_g - T_{wg}) - \frac{\lambda_w S_w}{\delta_w} (T_{wg} - T_{wf}) \quad (3.12a)$$

$$\rho_w c_{pw} (1 - \gamma_w) V_w \frac{\partial T_{wf}}{\partial t} = -\alpha_f S_f (T_{wf} - T_f) + \frac{\lambda_w S_w}{\delta_w} (T_{wg} - T_{wf}) \quad (3.12b)$$

where z is the space coordinate along the length L of the evaporator and V_f , V_g and V_w are the volume occupied by the working fluid, by the exhaust gas and by the wall, respectively. Furthermore, S is the surface area, c_p is the specific heat capacity, λ_w represents the wall thermal conductivity and δ_w is the wall thickness. A constant factor $\gamma_w = 0.6$ is introduced in Equation (3.12) to separate the mass of the wall, *i.e.*, $M_w = \rho_w V_w$, including fins on the exhaust side from the mass of the wall on the working fluid side. The wall conduction has been found to be of great importance for the dynamic evaporator behavior. Thus, in Equation (3.12), the transversal wall conduction is computed based on two temperature points, T_{wg} and T_{wf} .

The heat transfer coefficients on the exhaust gas side α_g and working fluid side α_f are based on Nusselt numbers correlation selected from [54]. The heat transfer on the exhaust gas side is enhanced by fins, and thus, a Nusselt number correlation for finned surfaces has been selected. On the working fluid side, the heat transfer coefficient depends on the flow regime, laminar or turbulent, indicated by the Reynolds number, as well as the working fluid state of matter, *i.e.*, liquid, two-phase and vapor. In the two-phase state, the heat transfer coefficient is a function of the vapor fraction obtained from the temperature-enthalpy diagram illustrated in Figure 3.2. The working fluid vapor fraction is computed as:

$$\chi_f = \frac{h_f - h_l(p_f)}{h_v(p_f) - h_l(p_f)} \quad (3.13)$$

where $h_l(p_f)$ and $h_v(p_f)$ denote the specific saturated liquid and vapor enthalpy, respectively, as a function of system pressure p_f .

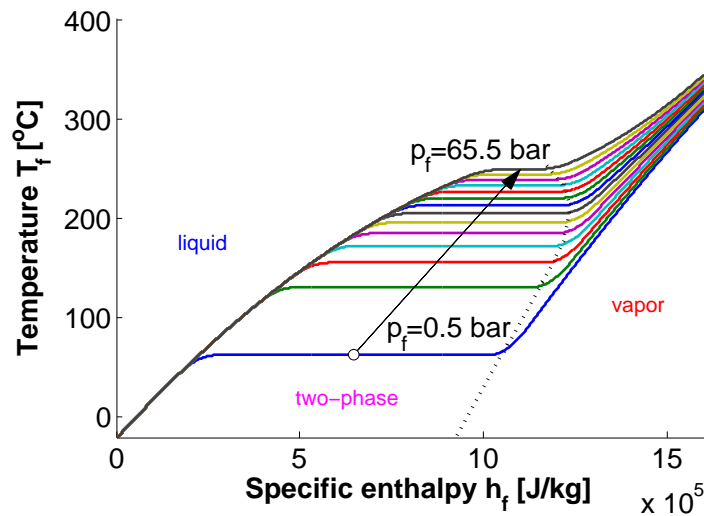


Figure 3.2: Ethanol temperature as a function of specific enthalpy and pressure.

Using Equation (3.13), the working fluid has the following states:

- $\chi_f \leq 0$ for liquid;
- $0 < \chi_f < 1$ for two-phase;
- $\chi_f \geq 1$ for vapor.

The condenser model is based on a simplified approach described in [42].

3.3.4 Mixing Junction

The mixing junction is considered to be characterized by fast fluid dynamics, such that the stationary conservation laws for mass flow and energy can be applied. Thus, the outlet mass flow is given by:

$$\dot{m}_{\text{out}} = \sum_{k=1}^n \dot{m}_{k,\text{in}} \quad (3.14)$$

where n is the total number of inlet fluid streams and $\dot{m}_{k,\text{in}}$ denotes the k -th inlet fluid mass flow.

Assuming ideal mixing, the stationary mixing junction vapor fraction is calculated with the energy balance equation as:

$$\chi_{\text{mix}} = \frac{1}{\dot{m}_{\text{out}}} \sum_{k=1}^n \dot{m}_{k,\text{in}} \chi_{k,\text{in}} \quad (3.15)$$

where $\chi_{k,\text{in}}$ are a function of specific enthalpy and system pressure according to Equation (3.13).

Pressure Volume

Let us consider the piping after the evaporators as a fixed volume. A pressure volume model is introduced to characterize the pressure and temperature dynamics inside the volume, as a function of the inlet and outlet conditions. The pressure volume model assumes that the working fluid is in the vapor state and that it behaves like an ideal gas. The laws for the mass conservation Equation (3.16a) and energy conservation Equation (3.16b) are then applied to this ideal gas:

$$\frac{dm}{dt} = \dot{m}_{\text{in}} - \dot{m}_{\text{out}} \quad (3.16a)$$

$$m c_v \frac{dT}{dt} = c_p \dot{m}_{\text{in}} T_{\text{in}} - c_v \left(\dot{m}_{\text{in}} - \dot{m}_{\text{out}} + \frac{c_p}{c_v} \dot{m}_{\text{out}} \right) T \quad (3.16b)$$

where m is the working fluid mass and T is the temperature inside the pressure volume.

Next, assume the ideal gas law:

$$\frac{dp}{dt} = \frac{p}{T} \frac{dT}{dt} + \frac{RT}{V} \frac{dm}{dt} \quad (3.17)$$

and define:

$$a = -\dot{m}_{in} - (\gamma - 1) \dot{m}_{out}, \quad b = \gamma \dot{m}_{in} \quad (3.18)$$

Then, Equation (3.16a) and (3.16b) become:

$$m \frac{dT}{dt} = bT_{in} + aT \quad (3.19a)$$

$$mT \frac{dp}{dt} = (bT_{in} + aT)p + mT \frac{R}{V} (\dot{m}_{in} - \dot{m}_{out}) \quad (3.19b)$$

where V is the volume, R is the ideal gas constant and γ is given by Equation (3.8). For steady-state conditions, Equation (3.19a) and (3.19b) simplify to $\dot{m}_{out} = \dot{m}_{in}$ and $T = -(b/a)T_{in} = T_{in}$, respectively.

3.3.5 Expander

The expander model is a map-based component, in which the outgoing mass flow rate is:

$$\dot{m}_{exp} = f_m \left(\omega_{exp}, \frac{p_{in}}{p_{out}} \right) \quad (3.20)$$

where ω_{exp} is the expander speed and p_{in}/p_{out} is the pressure ratio. In a similar way, the WHR system net output power, including the pumps' power, is given by:

$$P_{whr} = f_P \left(\omega_{exp}, \frac{p_{in}}{p_{out}} \right) \quad (3.21)$$

Next, the expander power is calculated by adding to Equation (3.21) the absolute net power of the pumps:

$$P_{exp} = P_{whr} + P_{p1} + P_{p2} \quad (3.22)$$

where P_{p1} , P_{p2} are the pumps' requested power. Assuming that the heat losses to the environment are negligible, the enthalpy at the expander outlet is obtained from:

$$h_{out} = h_{in} - \frac{P_{exp}}{\dot{m}_{exp}} \quad (3.23)$$

Similar to the vapor fraction modeling for the evaporator, the expander outlet vapor fraction is obtained by substituting Equation (3.23) into Equation (3.13).

3.3.6 Experimental Validation

The WHR system model validation is performed over a wide range of engine operating conditions: engine torque between 500–2600 N·m and engine speed between 1200–1850 rpm. The experimental data was first processed to check if the energy conservation principles are satisfied. To this end, data reconciliation techniques have been applied to correct for the mass flow rate measurement inaccuracies (more details are given in [42]).

The measured signals used as input for the WHR system model are: the expander speed, bypass valves duty cycle, exhaust gas mass flow rate and temperature for both the EGR and EXH evaporator. Based on these input signals, the WHR system model predicts the heat flow rate through the system, the working fluid mass flow rate, the system pressure, the temperature and the power. For brevity, here, we show a few results that are related to the improved evaporator models.

In Figure 3.3, the heat flow through the system, mass flow rate and pressure are compared with the measurements. All of the heat flow rates are expressed relative to the maximum condenser cooling capacity. The working fluid mass flow rates $\dot{m}_{f,egr}$ and $\dot{m}_{f,exh}$ and system pressure p_f are expressed relative to the maximum values that the system can reach. To calculate the exhaust gas and working fluid heat flow rate for both evaporators, the following expressions are used:

$$\begin{aligned}\dot{Q}_g &= \dot{m}_g c_{pg} (T_{g,in} - T_{g,out}) \\ \dot{Q}_f &= \dot{m}_f (h_{f,in} - h_{f,out})\end{aligned}\tag{3.24}$$

where c_{pg} is the exhaust gas heat capacity. For brevity, in Figure 3.3a, we show the total exhaust heat flow rate, calculated as:

$$\dot{Q}_{g,tot} = \dot{Q}_{g,egr} + \dot{Q}_{g,exh} + \dot{Q}_{loss,egr} + \dot{Q}_{loss,exh}\tag{3.25}$$

where $\dot{Q}_{loss,egr}$ and $\dot{Q}_{loss,exh}$ are the heat losses to the environment (see Equation (3.11a)). The exhaust gas heat flow rates $\dot{Q}_{g,egr}$ and $\dot{Q}_{g,exh}$ are transferred to the working fluid in the form of $\dot{Q}_{f,egr}$ and $\dot{Q}_{f,exh}$, respectively. From the simulation results, we can see that heat flow rates through the system are well captured by the model on both the exhaust gas side and working fluid side, with an average error of 2%. Furthermore, the mass flow rates through both evaporators show good behavior. The average error is 3%, as well as the pressure dynamics, with an average error of 2%. The oscillations observed between 2000–4000 s are a consequence of the WHR control algorithm, which manipulates the bypass exhaust gas valve u_{g_1} due to cooling requirements. As can be seen, after 4000 s, a peak in the total exhaust gas heat flow rate is present that exceeds the condenser

cooling capacity. However, this is for a short period of time, and thus, not visible in the working fluid heat flow rate, which could eventually lead to cooling issues.

In Figure 3.4, the working fluid temperature and vapor fraction after the evaporators and mixing junction are compared with experimental data. The working fluid temperature after the EXH evaporator shows that there are differences as compared to the measurements. This follows from the applied data reconciliation techniques, which are not perfect and still result in some inaccuracies with respect to the energy conservation principle. To overcome this behavior, more accurate mass flow sensors are necessary. Unfortunately, this equipment was not available at the experimental set-up. Furthermore, the instrumentation to measure the vapor fraction was not available. However, in the liquid region ($\chi \leq 0$) and vapor region ($\chi \geq 1$), the vapor fraction can be calculated based on the measured temperature and pressure. The two-phase behavior can be validated by observing at which moment the working fluid switches from the vapor state to the two-phase state and back at the evaporator outlet. This behavior can be seen for the EXH evaporator between 5000–7000 s, where the vapor fraction $\chi_{f,\text{exh}}$ drops significantly due to the low heat input (see the corresponding $\dot{Q}_{f,\text{exh}}$ in Figure 3.3a).

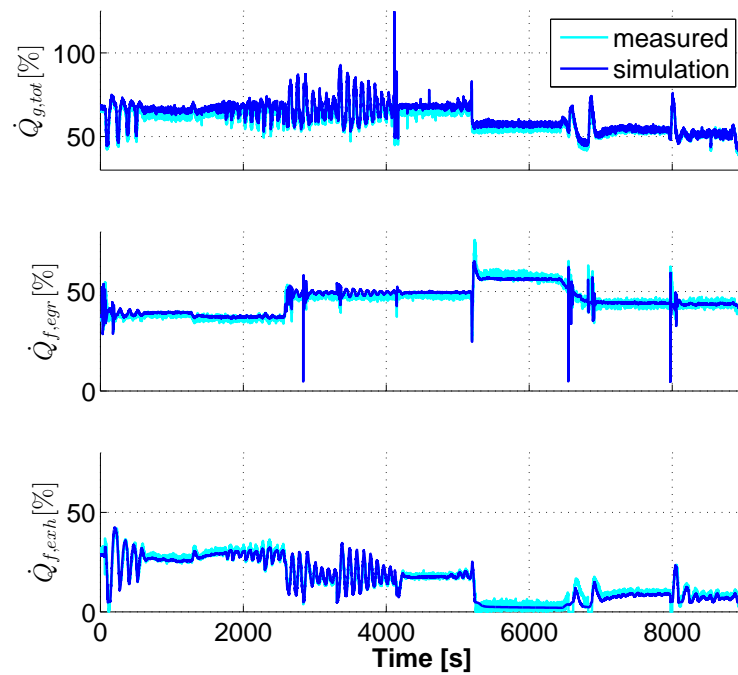
The model prediction error is calculated using the following expression:

$$e = 100 \cdot \frac{|y_{\text{sim}} - y_{\text{meas}}|}{y_{\text{max}} - y_{\text{min}}} \quad (3.26)$$

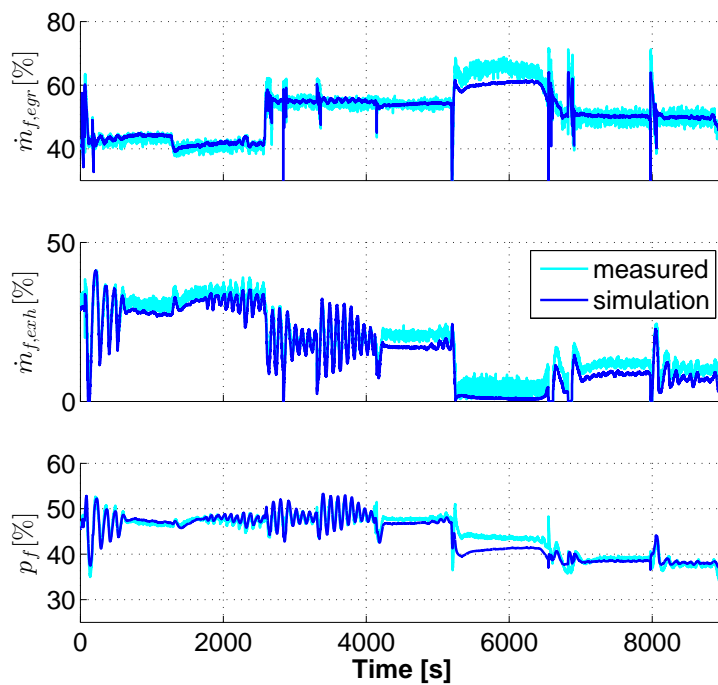
where y_{sim} is the output to be compared, while y_{max} and y_{min} are the outputs at maximum and minimum engine thermal load, respectively. The resulting average and maximum error for the heat flow rate, mass flow rate, system pressure and temperature are summarized in Table 3.1.

Table 3.1: Summary of the model prediction error and improvement compared with data from [42]

Symbol	Error		Improvement	
	Average	Maximum	Average	Maximum
\dot{Q}_f	2%	4%	-	2%
\dot{m}_f	3%	7%	-	-
p_f	2%	3%	-	1%
T_f	4%	13%	2%	7%

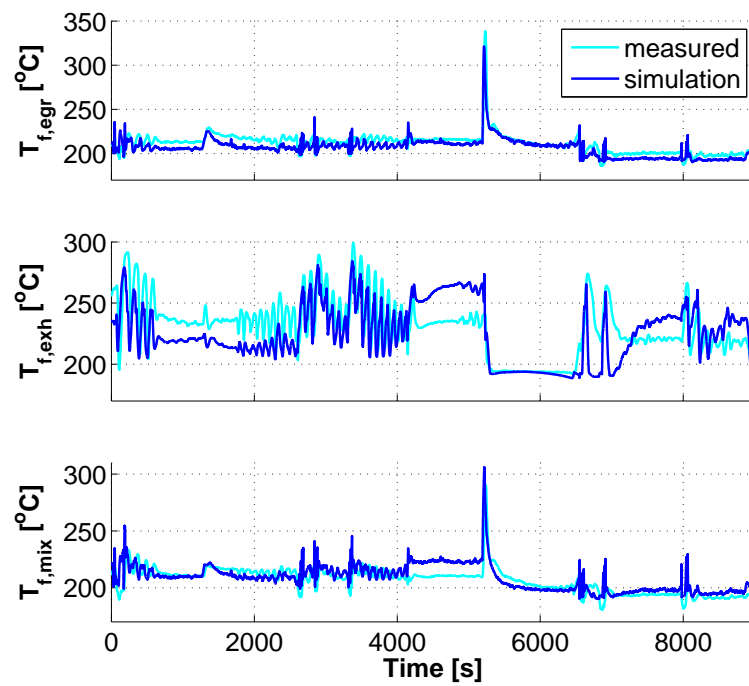


(a)

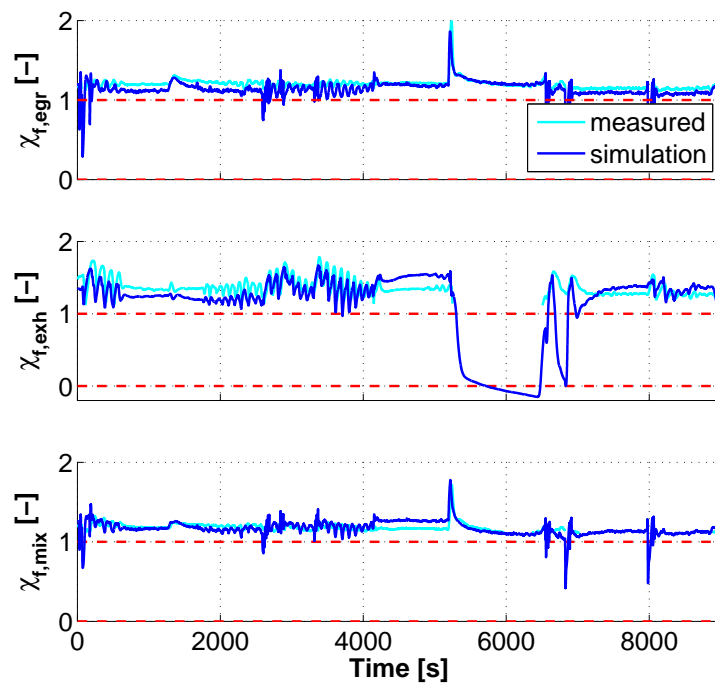


(b)

Figure 3.3: (a) Total exhaust gas heat flow rate, including losses and working fluid heat flow rate for both evaporators; (b) Working fluid mass flow rate through the evaporators and system pressure.



(a)



(b)

Figure 3.4: (a) Working fluid temperature after the evaporators and mixing junction; (b) Vapor fraction after the evaporators and mixing junction.

Compared to the previous model, we first see that the working fluid temperature prediction error decreased on average by 2%, while the maximum error decreased by 7%. This indicates that both the steady-state and dynamic behaviors of the evaporators are improved. For the mass flow rate, there is no improvement, since the pump and the valve models are kept the same. Furthermore, there is insignificant improvement for the average heat flow rate and system pressure error. However, due to the improved EGR and EXH evaporator models, the maximum heat flow rate and system pressure error decreased by 2% and 1%, respectively.

3.4 Control Design

In this section, the control objective is presented, followed by the model for control and the problem formulation in the model predictive control framework.

3.4.1 Control Objective

Based on Equation (3.13), let us denote the vapor fraction after the EGR and EXH evaporator with $\chi_{f,\text{egr}}$ and $\chi_{f,\text{exh}}$. Using Equation (3.15), the vapor fraction downstream of the mixing junction is given by:

$$\chi_{f,\text{mix}} = \frac{\dot{m}_{f,\text{egr}}\chi_{f,\text{egr}} + \dot{m}_{f,\text{exh}}\chi_{f,\text{exh}}}{\dot{m}_{f,\text{egr}} + \dot{m}_{f,\text{exh}}} \quad (3.27)$$

In Figure 3.5, the control scheme is illustrated. The control input is $u = [u_{\text{egr}} \ u_{\text{exh}}]^\top$; the output is $y = [\chi_{f,\text{egr}} \ \chi_{f,\text{exh}}]^\top$; and the engine disturbance $w = [\dot{Q}_{g,\text{egr}} \ \dot{Q}_{g,\text{exh}} \ \omega_{\text{eng}}]^\top$. The controller design objective can now be formulated as the synthesis of a control algorithm that maximizes the WHR system output power while guaranteeing safe operation, *i.e.*, $\chi_{f,\text{mix}} \geq 1$, in the presence of highly dynamic engine disturbances. However, an optimization problem that maximizes power with $\chi_{f,\text{mix}} \geq 1$ gives a non-unique global solution as a function of control input u . This could lead to excessive system actuation [61]. Additionally, in order to avoid infeasibility during optimization, the output constraints need to be included as soft constraints, which requires additional optimization variables. Thus, the problem complexity increases. To avoid these undesired effects while satisfying the safe operation requirement, here, we use a particular solution, in which the vapor quality after both evaporators indicates vapor, *i.e.*, $[\chi_{f,\text{egr}} \ \chi_{f,\text{exh}}]^\top \geq [1 \ 1]^\top$. The expander is able to cope with working fluid in

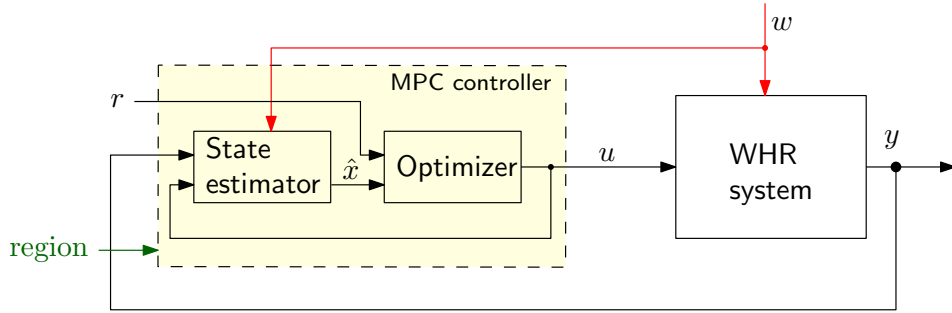


Figure 3.5: Schematic representation of the control scheme.

the two-phase state. Thus, for short periods of time, we assume a vapor fraction limit of 0.9 at the expander inlet.

The WHR system efficiency increases as the system operates closer to the safety margin [31], *i.e.*, $\chi_{f,egr} = \chi_{f,exh} = \chi_{f,mix} = 1$. Consequently, based on simulation results, the WHR output power is shown to reach its maximum at the safety margin [61]. Thus, for maximum output power, the controller design objective reduces to the synthesis of a control algorithm with good disturbance rejection properties that allows operation close to the safety limit.

3.4.2 Model for Control Design

For control design, a low-computational model that captures the WHR system dynamics is necessary. However, the developed high-fidelity WHR system model has around 150 states and is highly nonlinear, mainly due to the two-phase phenomena. Therefore, the model is linearized and reduced around a representative set of operating conditions. In Figure 3.6a, we show the steady-state WHR system operating area, including limitations: the sum of $\dot{Q}_{g,egr}$ and $\dot{Q}_{g,exh}$ is limited to 100% by the condenser cooling power; ethanol decomposition can occur at a temperature higher than 280 °C, and emissions can increase due to the low exhaust gas flow through the EGR valve. These limitations are expressed in the steady state, and thus, they can be violated for short periods of time, especially during transients. The resulting WHR system operating area is shown in green in Figure 3.6a.

Within the WHR system operating area, three linearization points are selected (see Figure 3.6a with numbers) that are shown to be sufficient in describing the WHR system dynamics [43]. The points are selected close to the boundaries for emissions and condenser limitation, where the system is expected to operate more often. This is seen from a World Harmonized Transient Cycle and steady-state measurements that

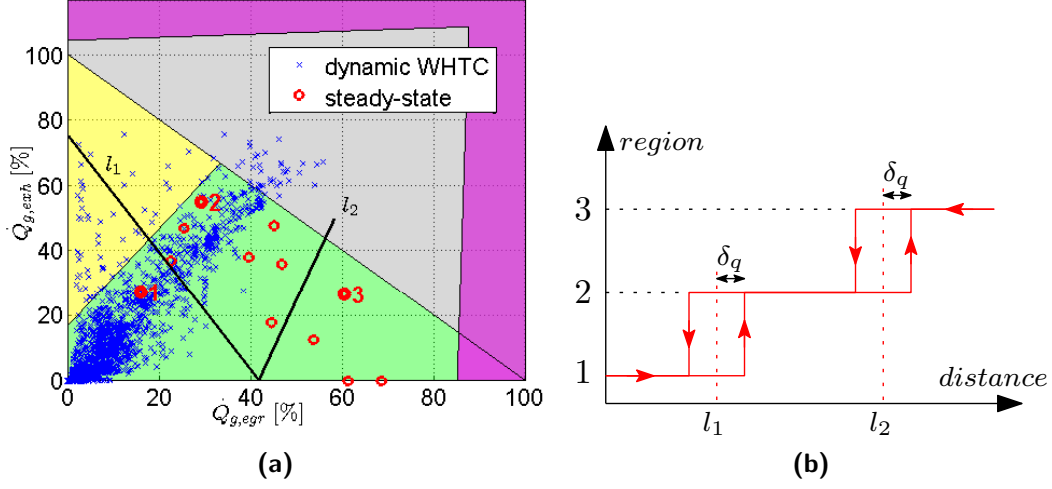


Figure 3.6: (a) Cold-start World Harmonized Transient Cycle and steady-state points within the waste heat recovery (WHR) system operating area (green) and limitations: cooling capacity (grey), high emissions (yellow), ethanol decomposition (magenta); (b) Schematic representation of the switching mechanism with hysteresis.

also motivate the switching lines choice l_1 and l_2 .

The three corresponding linear models are of high order, because they retain the same number of states as the high-fidelity model. To use these models for control, model reduction techniques based on balanced truncation are used. A model order of $n = 7$ is chosen, such that the error system $\|G - G_r\|_\infty$ satisfies:

$$\|G - G_r\|_\infty \leq 2(\sigma_{n+1} + \sigma_{n+2} + \dots + \sigma_m) \quad (3.28)$$

where G is the full linear model of order m , G_r is the reduced linear model of order n and σ are the singular values of G . The reduced order state-space linearized model in discrete time is:

$$\begin{aligned} x(k+1) &= A_i x(k) + B_{i,u} u(k) + B_{i,w} w(k) \\ y(k) &= C_i x(k), \quad i = \{1, 2, 3\} \end{aligned} \quad (3.29)$$

where $A_i \in \mathbb{R}^{n \times n}$, $B_{i,u} \in \mathbb{R}^{n \times q}$, $B_{i,w} \in \mathbb{R}^{r \times n}$, $x \in \mathbb{R}^n$, $u \in \mathbb{R}^p$, $w \in \mathbb{R}^q$, $y \in \mathbb{R}^r$.

The three reduced order models are integrated within the control scheme using a switching mechanism with hysteresis, as shown in Figure 3.6b. The switching mechanism indicates the active controller based on the EGR and EXH heat flow rates from the engine. This is achieved by monitoring the distance between the switching lines l_1 , l_2 and the point that expresses the current EGR and EXH heat flow rate. A parameter δ_q that defines the hysteresis is introduced to avoid chattering around

the switching lines. From simulation results, we conclude that $\delta_q = 14.5\%$ gives good switching behavior without chattering.

3.4.3 Linear Model Predictive Control

The control inputs $u(k) = [u_{\text{egr}}(k) \ u_{\text{exh}}(k)]^\top$, at time k , are computed by an MPC controller. The controller consists of a state estimator and an optimizer (see Figure 3.5). The state estimator is used to obtain estimates of $x(k)$ from the output $y(k) = [\chi_{\text{f,egr}}(k) \ \chi_{\text{f,exh}}(k)]^\top$ computed from the measurements. To improve the state estimation, the engine disturbances $w(k)$ are assumed to be measured.

The optimizer solves a linear optimization problem that minimizes a cost function J subject to constraints. As the objective is to have good disturbance rejection, the cost function J penalizes deviations of the predicted controlled outputs $\hat{y}(k+i)$ from a constant reference $r(k+i)$ and changes of the inputs $\Delta u(k+i)$. The penalty matrices W_y and $W_{\Delta u}$ are constant inside each operating region of the WHR system. The predictions are expressed in terms of $\Delta u(k+i) = u(k+i) - u(k+i-1)$, and the cost function is defined as:

$$J(k) = \sum_{i=0}^{N_y-1} \|r(k+i+1) - \hat{y}(k+i+1)\|_{W_y}^2 + \sum_{i=0}^{N_u-1} \|\Delta u(k+i)\|_{W_{\Delta u}}^2, \quad N_u \leq N_y \quad (3.30)$$

where N_y is the prediction horizon and N_u is the control horizon. The cost function $J(k)$ is obtained based on the reduced order linear model, which is used to predict the behavior of the plant, starting at the current time k , over a future prediction horizon N_y . This predicted behavior depends on the assumed input trajectory $u(k+i)$ over a control horizon N_u and measured output $y(k)$ and disturbance $w(k)$. The input increments $\Delta u(k+i) = 0$ for $i \geq N_u$, *i.e.*, $u(k+i) = u(k+N_u-1)$ for all $i \geq N_u$. In Equation (3.30), $\|\cdot\|_W^2$ denotes the weighted two-norm squared, *i.e.*, $\|x\|_W^2 = x^\top W^\top W x$.

At each time $k \in \mathbb{Z}_+$, we estimate the system state $x(k)$ and solve the following optimization problem (this is often called a receding horizon principle):

Problem 3.4.1.

$$\min_{\Delta u(k), \dots, \Delta u(k+N_u-1)} J(k) \quad (3.31)$$

subject to Equation (3.29) and:

$$0 \leq u(k+i) \leq 100, \quad i = 0, \dots, N_y - 1 \quad (3.32)$$

The control action sent to the system is $u(k) = u(k-1) + \Delta u^*(k)$, where $\Delta u^*(k)$ is the first element of the optimal sequence obtained by solving Problem 3.4.1. For state estimation, a general linear state observer [62] is designed based on the measured plant output, which gives the state estimate \hat{x} through a gain matrix. The gain matrix is designed using well-known Kalman filtering techniques.

For each region in the operating WHR area, an MPC controller is designed. All three MPC controllers receive the current manipulated variable and output signals, for their state estimates. During switching, the state estimator can experience bumps, because the model reduction does not preserve the same states for each region. However, by penalizing the input increments $\Delta u(k+i|k)$ in the optimization Problem 3.4.1, these effects are mitigated and aggressive plat actuation is avoided.

3.4.4 Nonlinear Model Predictive Control

In this section, a nonlinear model predictive control (NMPC) is developed using the high-fidelity WHR system model. In the NMPC control structure, the high-fidelity WHR system model is used for both, as prediction model and as simulation model. We denote the high-fidelity WHR system model using the general form of a non-linear system, *i.e.*:

$$\begin{aligned} \dot{x} &= f(x, u, w) \\ y &= g(x) \end{aligned} \tag{3.33}$$

where x is the state vector, u the control input, w the disturbance vector and y the model output. Then, at each time step $k \in \mathbb{Z}_+$, the NMPC strategy solves the following optimization problem:

Problem 3.4.2.

$$\min_{u(k), \dots, u(k+N_u-1)} J(k) \tag{3.34}$$

subject to Equation (3.33) and:

$$0 \leq u(k+i) \leq 100, \quad i = 0, \dots, N_y - 1 \tag{3.35}$$

The NMPC uses the same prediction horizon N_y and control horizon N_u as the linear MPC. However, note that Problem 3.4.2 computes directly the control input $u(k)$ over the control horizon N_u and not the control input increment $\Delta u(k)$. Moreover, a state

estimator and a switching mechanism are not necessary, since the control model and the high-fidelity model are identical. The solution to Problem 3.4.2 is obtained using the *fmincon* routine from Matlab.

The main reason for developing an NMPC strategy is for comparison purposes, since the algorithm is computationally expensive and, thus, is not feasible for online implementation.

3.5 Simulation Results and Discussion

To evaluate the MPC strategy, measurements from a Euro VI heavy-duty diesel engine are used. The control strategy is tested on a simple stepwise cycle and then on a cold-start World Harmonized Transient Cycle (WHTC) that covers typical driving conditions: urban, rural and highway. As a benchmark, a classical PI controller is used [43], as well as a nonlinear MPC (NMPC) strategy. The PI control objective is to manipulate the control input u , such that the evaporator's outlet temperature follows a predefined reference temperature. This reference temperature is the ethanol saturation temperature plus a safety margin of 10 °C. The simulation environment is MATLAB/Simulink[®] from The Mathworks Inc., Massachusetts, USA. The MPC strategy is implemented using the model predictive control Toolbox, while the NMPC strategy uses a sequential quadratic programming (SQP) solver.

The controller sampling time is $T_s = 0.4$ s, which yields an acceptable approximation of the system dynamics. The prediction horizon is $N_y = 45$, and the control horizon is $N_u = 4$ time steps. The prediction horizon of 18 s is chosen, so that the most important system dynamics within the engine operating area are captured. The control horizon of 1.6 s follows from the fact that larger values do not considerably improve the performance, while the computational complexity increases significantly. The corresponding weighting matrices are:

$$\begin{aligned}
 \text{MPC}_{\{1,2,3\}} : \quad & W_y = \{\text{diag}(0.8, 0.8), \text{diag}(0.9, 0.9), \text{diag}(0.8, 0.9)\}, \\
 & W_{\Delta u} = \{\text{diag}(0.05, 0.05), \text{diag}(0.1, 0.1), \text{diag}(0.2, 0.2)\}, \\
 \text{NMPC:} \quad & W_y = \text{diag}(0.9, 0.8), \\
 & W_u = \text{diag}(10^{-5}, 10^{-5})
 \end{aligned} \tag{3.36}$$

For the MPC strategy, the weighting matrices are tuned for a stepwise cycle, such that a good trade-off is obtained between control effort and robustness to model uncertainty. However, using these settings, the controller is shown to perform well also for other type of cycles, such as a WHTC. For the NMPC strategy, a similar weighting is chosen for

W_y . Since the NMPC optimization is performed subject to the high-fidelity model in Equation (3.33), the weighting W_u is chosen small to allow more control freedom.

3.5.1 Stepwise Cycle

In this cycle, illustrated in Figure 3.7a, the engine torque is varied stepwise within the complete operating area, *i.e.*, 500–2600 N·m, while the speed is kept constant at 1213 rpm. From the WHR system perspective, the engine torque and speed translates into EGR and EXH heat flow rate (see Figure 3.7b). The EGR and EXH heat flow rate together with the engine speed are the main disturbances for the WHR system, besides other disturbances, such as ambient temperature and ethanol temperature from the reservoir. The operating region is determined based on the EGR and EXH heat flow rate outside the controller. All three controllers become active with no chattering during switching, which could lead to instability. This indicates a good switching behavior of the switching mechanism with hysteresis.

In Figure 3.8, we show the vapor fraction after the EGR and EXH evaporator, as well as after the mixing junction. The reference r for the controller is set to a constant value of 1.05 superheat for both evaporators. From Equation (3.13), the superheat in temperature corresponding to this vapor fraction varies as a function of pressure from 10 °C to less than 5 °C as the pressure reaches its maximum. After the mixing junction, a good disturbance rejection is obtained, with $\pm 5\%$ maximum deviation from the specified reference r . Starting from 2400 s, the control inputs reached the limits (see the lower plot in Figure 3.8), *i.e.*, $u_{\text{egr}} = 0\%$ (fully closed) and $u_{\text{exh}} = 100\%$ (fully opened). Thus, the output is indeed no longer able to follow the reference. The reason comes from the engine heat flow rate: at the EGR evaporator, the exhaust gas heat flow rate reached more than 60% while at the EXH evaporator, it dropped close to zero due to u_{g_2} actuation to avoid exceeding the condenser cooling capacity. However, depending on the situation, the vapor fraction after the mixing junction can still show the vapor state, and therefore, mechanical power is delivered, despite the control input that hit the constraint.

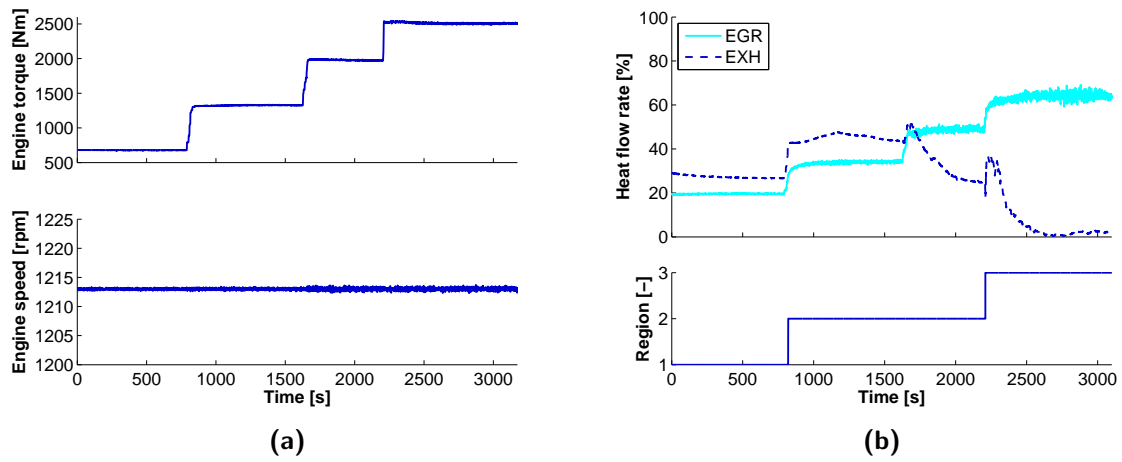


Figure 3.7: (a) Engine torque and speed; (b) Engine exhaust gas heat flow rate and the operating region signal.

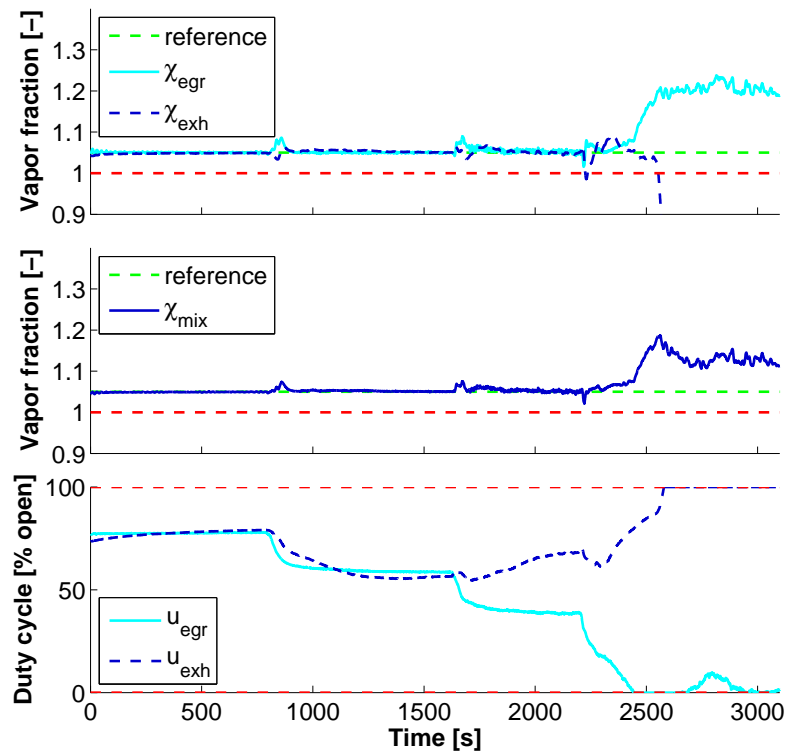


Figure 3.8: Vapor fraction after the exhaust gas recirculation (EGR) evaporator, exhaust (EXH) evaporator, mixing junction together with the control input for the model predictive control (MPC) strategy.

3.5.2 World Harmonized Transient Cycle

To validate and quantify the performance of the developed control strategy, a highly dynamic cold-start World Harmonized Transient Cycle (WHTC) is used (Figure 3.9a). This is an 1800 s cycle that consists of urban, rural and highway driving conditions. The WHTC is a challenging cycle due to a highly dynamic behavior that includes also the heat-up phase of the engine and WHR system. The engine disturbances from such a cycle are illustrated in Figure 3.9b. The switching signal indicates that only Regions 1 and 2 are reached.

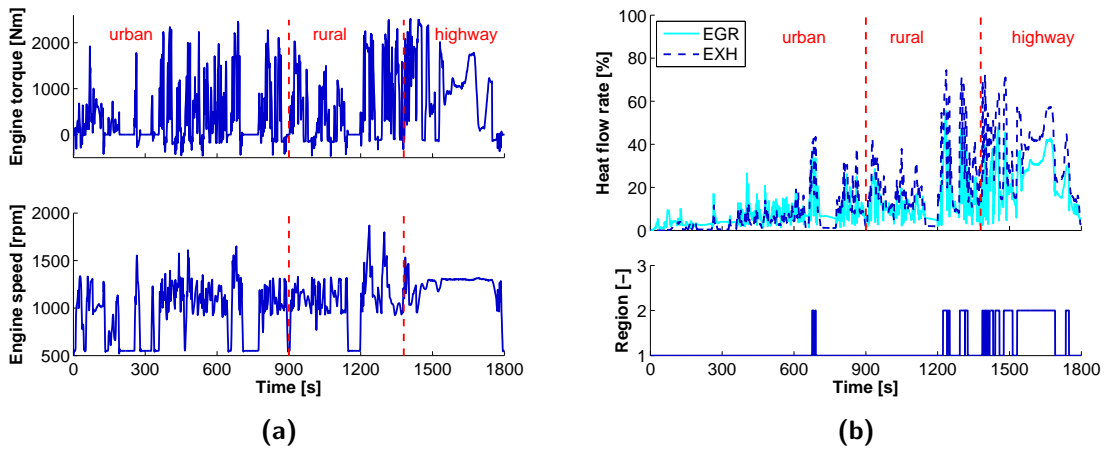


Figure 3.9: (a) Engine torque and speed from a cold-start World Harmonized Transient Cycle (WHTC); (b) Engine heat flow rate from a cold-start WHTC and operating region signal.

For comparison, we use two additional control strategies: a classical PI control scheme [43] and an NMPC strategy described in Section 3.4. The results for these three control strategies are shown in Figure 3.10. For brevity, we only show the vapor fraction after the mixing junction.

During the first 1200 s, the WHR system is heating up, and therefore, no vapor state is encountered after the mixing junction. Note, however, that for each evaporator, the heat-up period is different, up to 600 s for the EGR evaporator and 1200 s for the EXH evaporator. The exhaust evaporator takes longer to heat-up due to more mass and the aftertreatment system located upstream. The difference in heat-up period can be observed also from the period of time the control input u_{egr} and u_{exh} are on the constraint.

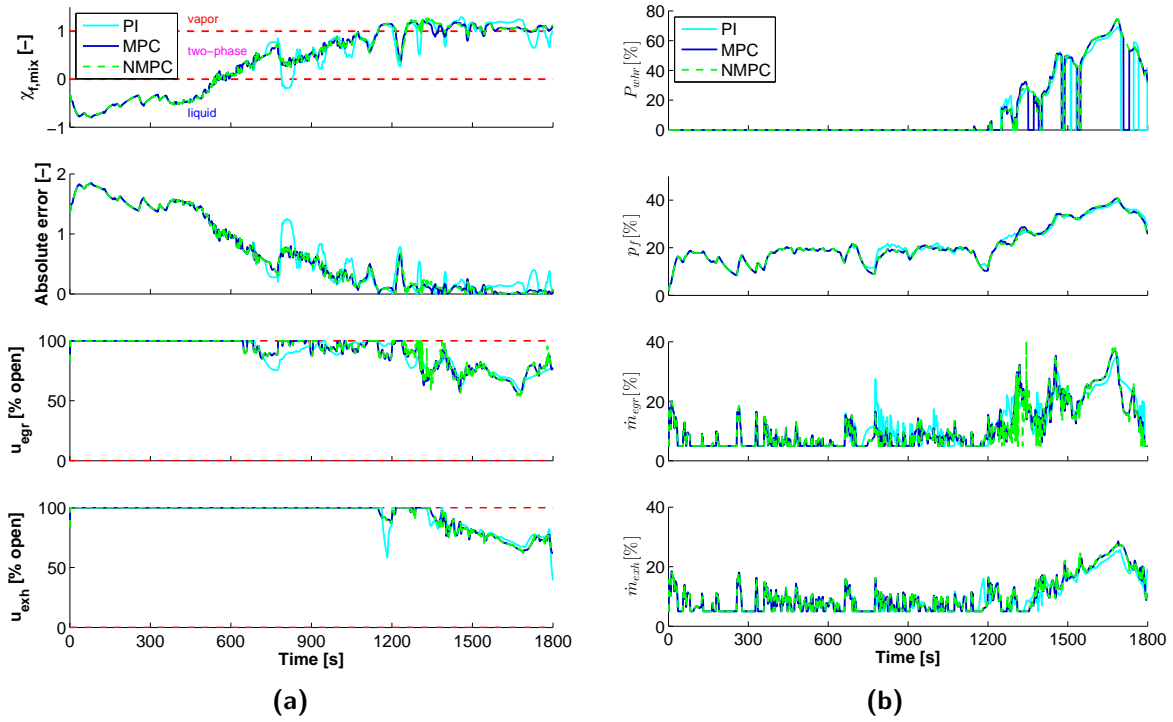


Figure 3.10: (a) Vapor fraction after the mixing junction, absolute error and control inputs for proportional-integral (PI), model predictive control (MPC) and nonlinear MPC (NMPC) control strategy for a cold-start WHTC; (b) WHR system net output power, system pressure and mass flow rates through the EGR and EXH evaporator.

The objective of all three controllers is to maintain vapor and to be as close as possible to $\chi_{f,egr} = \chi_{f,exh} = 1$ for maximum output power. However, due to highly dynamic disturbances and the limitations of the control input, maintaining the vapor state is challenging. The main reasons for introducing an NMPC controller are: first, to verify how good is the control strategy if the WHR system model is exactly known, and second, what the global control input solution is. From the simulation results, we found that the global solution is difficult to obtain, since the system is highly nonlinear with local minima over the prediction horizon. Thus, the NMPC solution is sensitive to the initial condition for the optimization Problem 3.4.2. Here, for initialization of the NMPC strategy, we used the MPC solution. As a result, the NMPC strategy corrects for the modeling errors between the reduced order linear model and the high-fidelity model.

At first instance, all three controllers seem to behave quite similarly, especially the MPC and NMPC control strategies. To quantify the performance of each controller, we use two indicators: the time in the vapor state t_v and the recovered thermal energy U over the complete cycle.

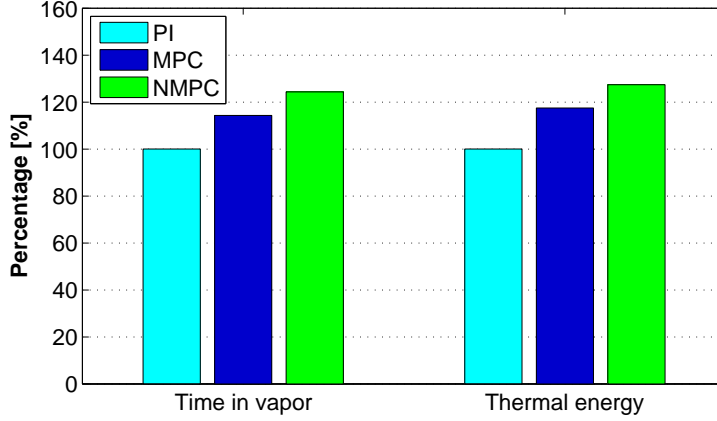


Figure 3.11: Time in the vapor state and recovered thermal energy for the MPC and NMPC strategy compared to the PI control strategy.

The performance indicators are define as follows:

$$\text{Time in vapor state: } t_v = T_s \sum_0^{t_f} (\chi_{\text{mix}} \geq 1) \quad (3.37)$$

$$\text{Thermal energy: } U = \int_0^{t_v} P_{\text{whr}}(t) dt \quad (3.38)$$

where t_f is the total cycle time and $P_{\text{whr}}(t)$ is the instantaneous WHR system net output power. The instantaneous output power $P_{\text{whr}}(t)$ and the recovered energy U are calculated only when the safety requirement $\chi_{\text{mix}} \geq 1$ is satisfied. In the case that the safety requirement is not fulfilled, *i.e.*, $\chi_{\text{mix}} < 1$, the expander needs to be bypassed to avoid damage.

From Figure 3.11, we can see that the MPC controller outperforms the PI controller in terms of time in the vapor state and recovered thermal energy, with approximately 15%. The NMPC strategy improves the considered performance indices by 10% as compared to the MPC strategy. This result gives an indication about the model uncertainty used within the MPC strategy. Despite the improved result, the NMPC controller has several drawbacks. First, the computational complexity is significant, which makes the NMPC scheme not feasible for real-time implementation. Second, it can converge to local minima, resulting in worse control behavior than with a linear MPC. As a solution, an NMPC algorithm that uses global solvers can be considered; however, the computational complexity will grow even more.

3.6 Conclusions and Future Research

The modeling and control of a waste heat recovery system for a Euro-VI heavy-duty truck engine was considered. The exhaust gas energy is recovered by means of two parallel evaporators. To generate power, an expander is used, mechanically coupled with the pumps to the engine crankshaft. The main conclusions of this chapter are summarized in what follows.

- (1) The existing WHR system model was improved by including enhanced evaporator models. The model combines the finite difference modeling approach with a moving boundary one and, thus, captures multiple phase transitions along a single pipe flow.
- (2) A switching model predictive control strategy was designed, to guarantee the safe operation of the WHR system. The proposed control strategy performance is demonstrated on a highly dynamic cold-start World Harmonized Transient Cycle. Simulation results showed improved performance for the proposed MPC strategy in terms of vapor time and recovered thermal energy by 15%, as compared to a classical PI controller;
- (3) A nonlinear model predictive control was developed to demonstrate that control performance can be improved by approximately 10% in the case that the model of the system is exactly known.
- (4) One limitation of the proposed MPC strategy is the need of vapor fraction measurement equipment or an estimator to make the method applicable in practice.

Future work will focus on vapor fraction estimation and on experimental demonstration of the proposed MPC strategy. Furthermore, the supervisory control strategy [32] that combines energy and emission management will be extended by considering the proposed WHR control strategy.

Control of a Waste Heat Recovery System with Decoupled Expander¹

Abstract In this chapter, a switching Model Predictive Control strategy is proposed for a Waste Heat Recovery system in heavy-duty automotive application. The objective is to maximize the WHR system output power while satisfying the output constraints under highly dynamic engine variations. For control design, a WHR system architecture with the expander and pumps decoupled from the engine is considered. Compared to a WHR system with the expander coupled to the engine, up to 29% more output power is obtained for the considered design. This holds for both steady state and highly dynamic engine conditions. The simulation results are obtained using a validated high-fidelity WHR system model with realistic disturbances from a Euro VI heavy-duty diesel engine.

4.1 Introduction

In the automotive industry, the main objective is to minimize the fuel consumption of internal combustion engines within the emission constraints. Despite the implementation of new engine technologies, approximately 60% of the fuel energy is still lost through the coolant and exhaust [29]. A promising technology to further increase the engine efficiency, and thus reducing the CO₂ emissions, is to exploit the exhaust gas energy using a Waste Heat Recovery (WHR) system [31]. A WHR system converts the exhaust gas energy to mechanical power, which can be used for the engine drivetrain or to drive an electric generator.

For automotive applications, one of the most attractive technology for heat recovery is

¹This chapter is based on [44].

based on the Organic Rankine Cycle (ORC) [51, 63]. The main reason is that ORCs use as working fluid an organic substance instead of water, which is better adapted to lower heat temperature sources [59, 64]. Furthermore, unlike Rankine Cycles (RCs) used in power plants, an ORC allows local and small scale power generation. As a result, ORCs become suitable for automotive systems, where physical space is limited.

Compared to power plants, the main challenge in automotive is WHR system operation with highly dynamic heat sources. According to the driving cycle, the exhaust gas temperature and mass flow rate can experience large variations. This can degrade the WHR system performance and lead to critical conditions such as: dry out, flooding and temperature shocks in the components [13].

To maximize the output power while avoiding critical conditions, control of WHR systems is crucial [31]. Most of the control methods are based on PI or PID controllers [26, 27]. A WHR system is a multiple-input multiple-output (MIMO) system characterized by coupling between the inputs and outputs. Often these couplings are neglected and treated as parallel single-input single-output (SISO). This may not be adequate for highly transient applications. In the open literature, only a few WHR control strategies are presented that can handle multivariable control problems. In [60], a generalized minimum variance control was designed for a 100 kW WHR system. Although the control method showed satisfactory set-point tracking and disturbance rejection performance, the literature is still lacking optimal control methods for WHR systems with constraints.

This chapter presents a switching Model Predictive Control strategy for a WHR system heavy-duty automotive application. The method deals with highly dynamic engine behavior and with system constraints to guarantee safe operation. The focus is on maximizing the system pressure as a way of generating the maximum output power, subject to input and output constraints. A WHR system with the expander and pumps decoupled from the engine is considered. Hence, the expander speed is free to vary allowing different operating pressures. For comparison, the WHR system architecture from [41] is used as a benchmark. This benchmark WHR system has the expander and the pumps mechanically coupled to the engine. Both architectures are evaluated for steady-state conditions and for real-world driving conditions from the World Harmonized Transient Cycle (WHTC).

This chapter is organized as follows. In Section 4.2, the studied WHR system is described. In Section 4.3, the control problem is formulated. Section 4.4 provides a steady-state analysis for output power maximization. In Section 4.5, the Model Predictive Control design is presented. Section 4.6 compares the proposed control

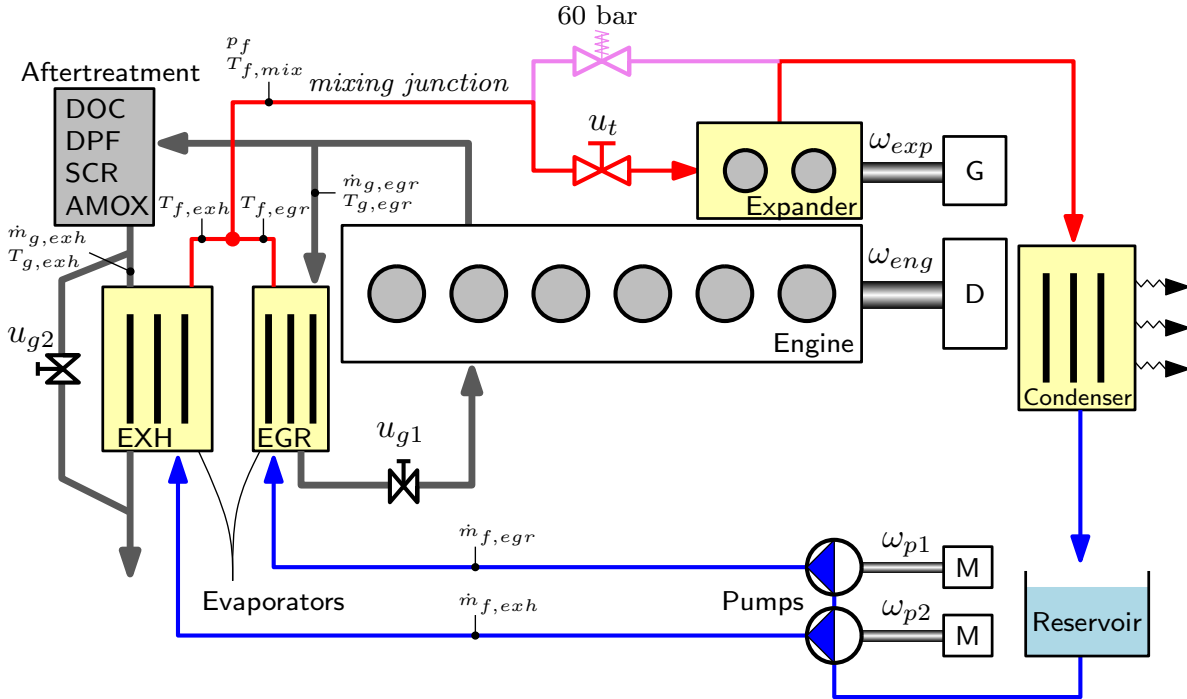


Figure 4.1: Schematic representation of the fully decoupled system.

performance for both coupled and decoupled WHR system architectures. Conclusions and suggestions for future research are presented in Section 4.7.

4.2 System description

The studied system is illustrated in Fig. 4.1. The heat source is a 13 liter, 6 cylinder Euro-VI heavy-duty diesel engine with common rail injection, a variable-geometry turbocharger and an aftertreatment system. The aftertreatment system consists of a Diesel Oxidation Catalyst (DOC), a Diesel Particulate Filter (DPF), Selective Catalytic Reduction (SCR), and an Ammonia Oxidation catalyst (AMOX). To recover the exhaust gas energy a WHR system is installed. The WHR system recovers heat from both the Exhaust Gas Recirculation line and the line downstream of the aftertreatment system, by means of two evaporators: called EGR and EXH, respectively. The working fluid is pure ethanol due to its properties that are suitable for this low-temperature application. The working principle of the studied WHR system is based on the Organic Rankine Cycle (ORC) principle: the ethanol is pumped from a reservoir through the EGR and EXH evaporators. There, the fluid is vaporized, passes through the expander, rejects heat at the condenser, and returns back to the reservoir. Using a two-piston expander, the vaporized ethanol is expanded and as a result, mechanical power is produced.

The system pressure is limited to 60 bar, by a pressure relief valve. The EGR valve u_{g1} is controlled by the Engine Control Unit (ECU), whereas u_{g2} is a valve that bypasses the exhaust gas such that the condenser cooling capacity is not exceeded. The expander is mechanically coupled to a generator (G), while the pumps are independently driven by electric motors (M). This WHR system design offers an additional degree of freedom related to the evaporation temperature. In a design with the expander coupled to the engine the system pressure is given by the engine and pumps speed, while in a decoupled configuration the pressure can be varied by manipulating the expander speed using a generator. An on/off throttle valve u_t is installed before the expander, to accommodate gear shifting for the case with the expander coupled to the engine. In this study, the focus is on power mode (excluding gear shifting). Thus, the throttle valve is maintained fully opened ($u_t = 100\%$).

4.3 Problem formulation

An important requirement for the WHR system is safe operation. The system is said to operate safely if vapor state is maintained before the expander. The presence of droplets at the inlet of the expander can lead to damage of the system.

The ethanol two-phase behavior is based on the temperature-enthalpy characteristic illustrated in Fig. 4.2. Let us define the vapor fraction χ_f as:

$$\chi_f = \frac{h_f - h_l(p_f)}{h_v(p_f) - h_l(p_f)}, \quad (4.1)$$

where $h_l(p_f)$ and $h_v(p_f)$ denote the specific saturated liquid and vapor enthalpy, respectively, as a function of system pressure p_f . Based on Eq. (4.1), the working fluid has the following states:

- $\chi_f \leq 0$ for liquid;
- $0 < \chi_f < 1$ for two-phase;
- $\chi_f \geq 1$ for vapor.

Let us denote the vapor fractions downstream of the EGR and EXH evaporator with $\chi_{f,egr}$ and $\chi_{f,exh}$, respectively. Assuming perfect mixing, the stationary vapor fraction after the mixing junction is:

$$\chi_{f,mix} = \frac{\dot{m}_{f,egr}\chi_{f,egr} + \dot{m}_{f,exh}\chi_{f,exh}}{\dot{m}_{f,egr} + \dot{m}_{f,exh}}, \quad (4.2)$$

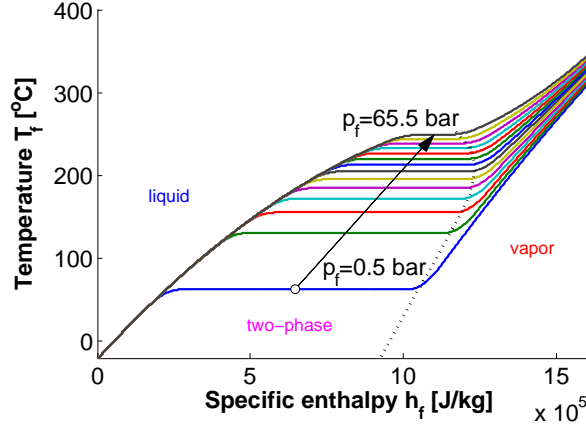


Figure 4.2: Ethanol temperature as a function of specific enthalpy and pressure.

where $\dot{m}_{f,egr}$ and $\dot{m}_{f,exh}$ are the ethanol mass flow rates through the evaporators. The WHR system net output power is defined as:

$$P_{whr} = P_{exp} - P_{pump1} - P_{pump2}, \quad (4.3)$$

where P_{exp} is the expander output power and P_{pump_i} is the requested power for pump $i = \{1, 2\}$.

The objective is to maximize the WHR system net output power, while satisfying the safety requirement in the presence of highly dynamic engine disturbances. These disturbances are the following exhaust gas heat flow rates:

$$\dot{Q}_{g,i} = \dot{m}_{g,i} c_{p,i} (T_{g,i} - T_{amb}), \quad i = \{egr, exh\}, \quad (4.4)$$

where $\dot{m}_{g,i}$ and $T_{g,i}$ are the exhaust gas mass flow rates and temperatures upstream of the evaporators, $c_{p,i}$ are the heat capacities, and T_{amb} is the ambient temperature.

From an optimization perspective, the problem can be formulated as follows:

Problem 4.3.1.

$$\begin{aligned} & \max_{\omega_{p1}, \omega_{p2}, \omega_{exp}} P_{whr} \\ & \text{subject to: } \chi_{f,mix} \geq 1 \\ & \omega_p^{min} \leq \omega_{\{p1,p2\}} \leq \omega_p^{max} \\ & \omega_{exp}^{min} \leq \omega_{exp} \leq \omega_{exp}^{max} \end{aligned} \quad (4.5)$$

In Eq. (4.5), ω_p^{min} , ω_p^{max} are the pump minimum and maximum speed and ω_{exp}^{min} , ω_{exp}^{max} are the expander minimum and maximum speed, respectively.

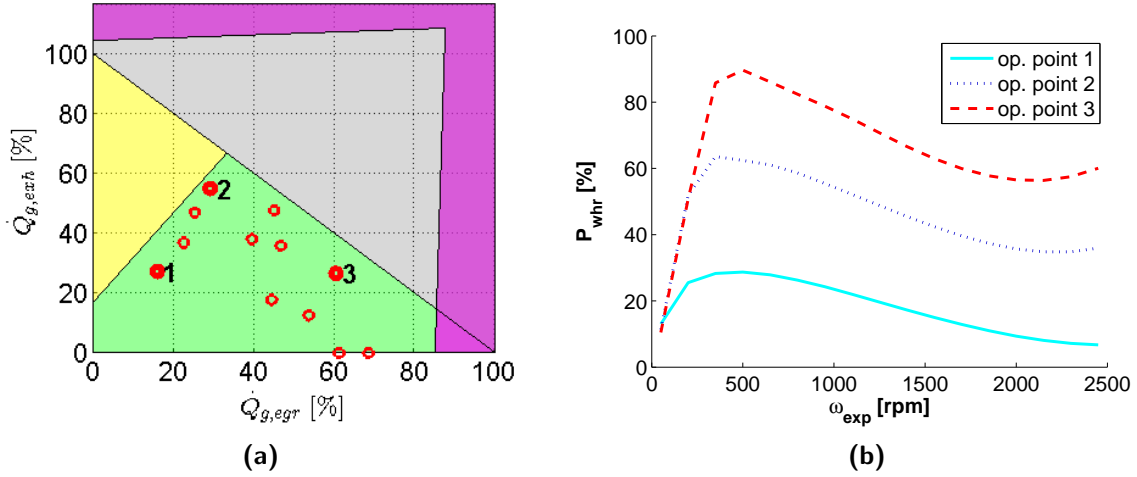


Figure 4.3: (a) WHR system operating area (green) and limitations: cooling capacity (grey), high emissions (yellow), ethanol decomposition (magenta). (b) WHR system net output power for $\chi_{f,egr} = \chi_{f,exh} = 1.1$.

4.4 System analysis

For the analysis of the WHR system, a validated high-fidelity WHR system model is used (details of this model can be found in [41]). The model includes the convective heat losses to the environment and is developed for analysis and control design of the WHR system. In Fig. 4.3a, the WHR system operating area and limitations are shown: *i*) the cooling limitation (grey) due to condenser capacity, *ii*) ethanol degradation (magenta) that can occur at fluid temperatures higher than 280°C, *iii*) increased emissions (yellow) due to low EGR exhaust gas flow rate. Assuming that these limitations are dealt with at a supervisory level, the green area becomes the WHR system operating region. Inside this region, twelve steady-state points were measured on the experimental set-up. We perform a steady-state analysis on three representative operating points (indicated in Fig. 4.3a with numbers).

The WHR system output power as function of the expander speed is shown in Fig. 4.3b. The results are obtained by varying the expander speed over the complete range while the pumps speed are adjusted such that $\chi_{f,egr} = \chi_{f,exh} = \chi_{f,mix} = 1.1$. For all the three operating points, the optimum expander speed is around 500 rpm. It is found that this optimum expander speed is the same for all the engine conditions in which vapor state can be achieved. However, there are engine conditions, *e.g.*, with low exhaust gas temperatures, for which vapor state cannot be realized at $\omega_{exp} = 500$ rpm. Therefore, the expander speed needs to be increased such that the system operates at a lower

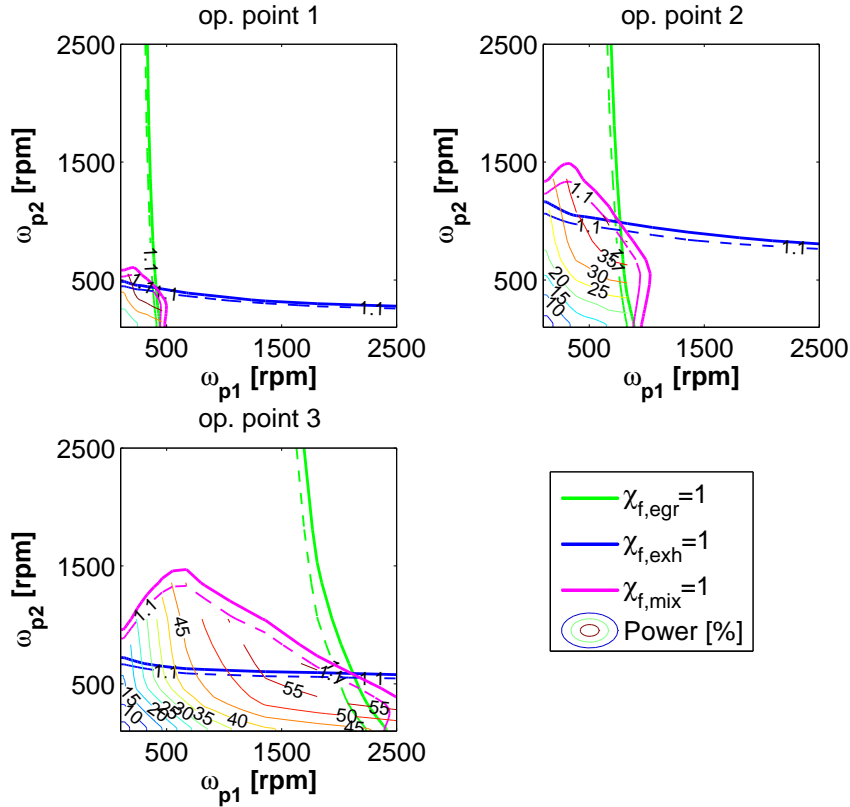


Figure 4.4: Steady-state analysis for a fixed expander speed $\omega_{exp} = 1700$ rpm under three different engine conditions.

pressure. Accordingly, the evaporation temperature can be reached and vapor state can be realized.

For a fixed expander speed, Fig. 4.4 shows the vapor fractions, as a function of pumps speed, after each evaporator and after the mixing junction. The expander speed is kept fixed in order to analyze the maximum net output power as a function of the working fluid superheat. Mechanical power is produced when $\chi_{f,mix} \geq 1$. Otherwise, the expander needs to be bypassed to avoid damage. The power contour lines show that the maximum output power is obtained at the intersection point of the saturated vapor lines, *i.e.*,

$$\chi_{f,egr} = \chi_{f,exh} = \chi_{f,mix} = 1. \quad (4.6)$$

System operation at the saturated vapor boundary is challenging to maintain under highly dynamic engine disturbances. Therefore, the superheat is increased, *e.g.*, to $\chi_{f,egr} = \chi_{f,exh} = \chi_{f,mix} = 1.1$, as illustrated in Fig. 4.4 with dashed lines. The choice of the superheat value is a tradeoff between disturbance rejection and maximum output power.

4.5 Control design

In this section the control objective is given and the control problem is formulated in the Model Predictive (MPC) framework. The main reasons for choosing MPC are: it explicitly takes input and output constraints into account and it handles multivariable control problems naturally.

4.5.1 Control objective

The control scheme illustrated in Fig. 4.5 consists of: a switching mechanism, an MPC controller and the WHR system. The control input is defined as $u = [\omega_{p1} \ \omega_{p2} \ \omega_{exp}]^T$, the output is $y = [\chi_{f,egr} \ \chi_{f,exh} \ p_f]^T$, and the engine disturbance is $w = [\dot{Q}_{g,egr} \ \dot{Q}_{g,exh}]^T$. In practice, for the single-phase state (liquid and vapor), the vapor fractions can be calculated from the measured temperatures $T_{f,egr}$, $T_{f,exh}$ and pressure p_f based on the temperature-enthalpy characteristic illustrated in Fig. 4.2. For the two-phase state, a vapor fraction estimator is required, *e.g.*, using the working fluid density information. Here for simplicity, we assume that the information regarding the vapor fractions $\chi_{f,egr}$ and $\chi_{f,exh}$ are available.

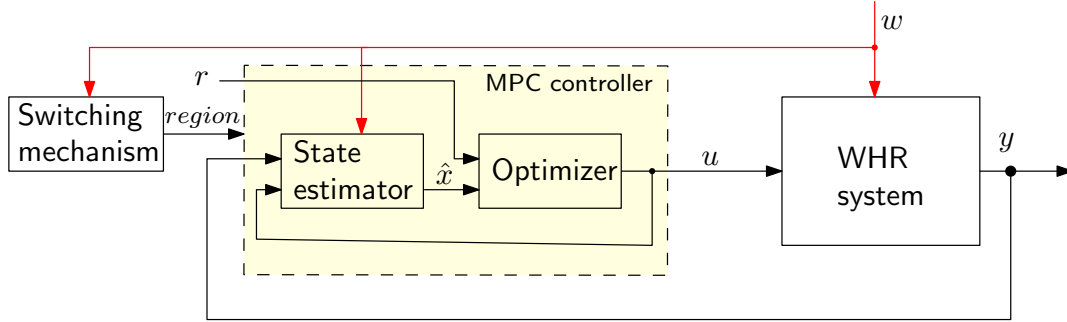


Figure 4.5: Schematic representation of the MPC control strategy.

The objective is to solve optimization Problem 4.3.1. First, the WHR system power is a nonlinear function that depends on the working fluid state (liquid, two-phase and vapor), engine heat flow rates, system pressure, pumps and expander speed. The WHR system output power shows a strong dependency with pressure: as the pressure increases also the output power increases. Thus the expander speed is manipulated, such that the system pressure is maximized and as a consequence, also the output power. Second, with respect to the safe system operation, it was shown that maximum power is obtained at the saturated vapor boundary, *i.e.*, $\chi_{f,egr} = \chi_{f,exh} = 1$. Under highly dynamic engine

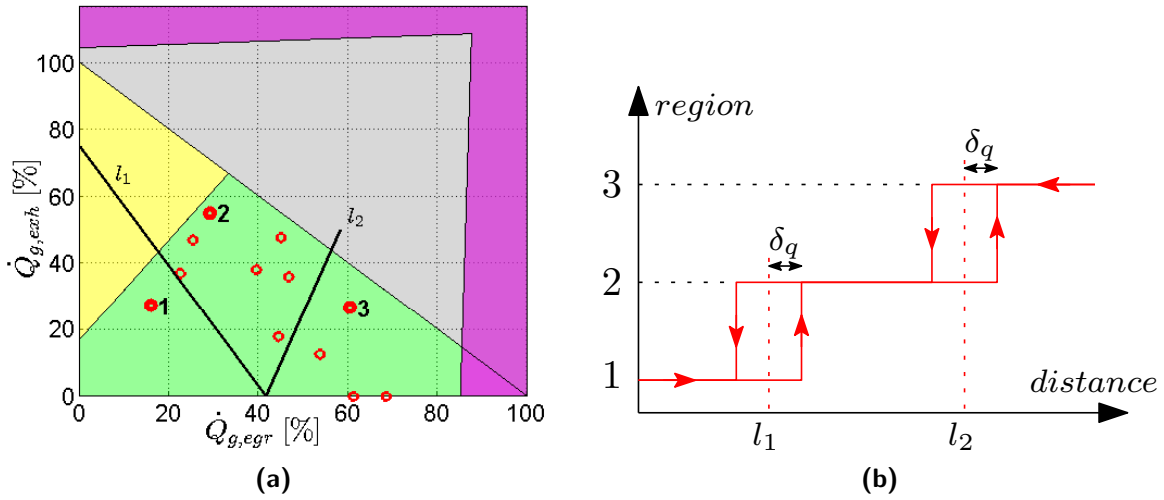


Figure 4.6: (a) WHR system partitioned operating area. (b) Representation of the switching mechanism with hysteresis.

disturbances, the expander manufacturer data indicates that vapor fractions down to 0.9 for a short period of time are allowed. However, to avoid formation of droplets during the expansion process and in the presence of engine disturbances, the operation at the saturated vapor line is not feasible in practice. Thus, a safety margin is adopted in which the regulation control problem is to maintain a vapor fraction of $\chi_{f,egr} = \chi_{f,exh} = 1.1$. In Section 4.6, we will show that, for real driving conditions, this safety margin produces a good tradeoff between disturbance rejection and output power.

The controller design can be summarized as the synthesis of a control algorithm with the following objectives: (i) guarantee safe operation, (ii) maximize system pressure.

4.5.2 Switching mechanism

The WHR system is highly non-linear mainly due to the two-phase phenomena inside the evaporators. As a result, one linear controller for the complete engine operating range is not sufficient to achieve the desired control objectives (i) and (ii). A solution is to partition the WHR system operating area in several regions. Two switching lines l_1 and l_2 are defined that partition the WHR system operating area in three regions (see Fig. 4.6a). To avoid chattering around the switching lines, a hysteresis is introduced, as illustrated in Fig. 4.6b. A parameter δ_q characterizes the switching behavior. Based on simulation results, a $\delta_q = 14.5\%$ is adopted, which shows good switching behavior with respect to highly dynamic engine heat flow rates $\dot{Q}_{g,egr}$ and $\dot{Q}_{g,exh}$.

4.5.3 State estimator

The high-fidelity WHR system model is of high order, *i.e.*, $n = 150$ states, which is rather large for control design. Therefore, the model is linearized and reduced around a representative operating points (see Fig. 4.6a with numbers). The points are selected close to the boundaries for emissions and condenser limitation, where the WHR system is expected to operate more often, as seen from the World Harmonized Transient Cycle. For each region, the linearized model is reduced by balanced truncation, resulting in the following state-space discrete time linear model:

$$\begin{aligned} x(k+1) &= A_i x(k) + B_{i,u} u(k) + B_{i,w} w(k), \\ y(k) &= C_i x(k), \quad i = \{1, 2, 3\}, \end{aligned} \quad (4.7)$$

where $A_i \in \mathbb{R}^{n \times n}$, $B_{i,u} \in \mathbb{R}^{n \times q}$, $B_{i,w} \in \mathbb{R}^{n \times r}$, $x \in \mathbb{R}^n$, $u \in \mathbb{R}^p$, $w \in \mathbb{R}^q$, $y \in \mathbb{R}^r$. The dynamical behavior of (4.7) is more important than the steady-state behavior, since the system will hardly reach steady-state for the studied cycle. The order of these models is chosen such that the error system is less than twice the sum of the full order model singular values [41]. This results in a $n = 9$ order model for each operating region.

To estimate the system state \hat{x} , a general state observer is designed. The state observer estimates \hat{x} based on a gain matrix. The gain matrix is design using well known Kalman filtering techniques [62]. Note that the MPC controller receives measurements of the disturbance $w(k)$, to improve the state estimation. These disturbances, however, are considered constant over the prediction horizon. One could improve the control performance by including information about the disturbance dynamic behavior. As a result, controller switching inside the prediction window becomes possible.

4.5.4 Optimizer

The predictive control problem minimizes at each time step k a cost function $J(k)$. The cost function $J(k)$ penalizes the deviations of the predicted controlled outputs $\hat{y}(k+i)$ from a reference r , changes of the inputs $\Delta u(k+i)$, and additional terms for output constraints violation. The cost function is defined as:

$$\begin{aligned} J(k) &= \sum_{i=0}^{N_y-1} \|r - \hat{y}(k+i+1)\|_{W_y}^2 \\ &+ \sum_{i=0}^{N_u-1} \|\Delta u(k+i)\|_{W_{\Delta u}}^2 + \rho \epsilon^2, \quad N_u \leq N_y \end{aligned} \quad (4.8)$$

where N_y and N_u are the prediction horizon and control horizon, respectively. The decision variables are expressed in terms of the input increments $\Delta u(k+i) = u(k+i) - u(k+i-1)$. For $i \geq N_u$, the input increments $\Delta u(k+i) = 0$, *i.e.*, $u(k+i) = u(k+N_u-1)$ for all $i \geq N_u$. In (4.8), $\|\cdot\|_W^2$ denotes the weighted 2-norm squared, *i.e.*, $\|x\|_W^2 = x^\top W^\top W x$.

The constraints on the output $y(k)$ are softened by introducing a slack variable $\epsilon \geq 0$. The weight ρ penalizes the output constraints violation and is defined as:

$$\rho = 10^5 \cdot \max\{W_y, W_{\Delta u}\}. \quad (4.9)$$

Note that in (4.9), the weight ρ is much larger than any element from W_y and $W_{\Delta u}$. This makes the last term in (4.8) more important than other terms, when the output constraints are violated. Furthermore, in (4.8), the reference is chosen constant, *i.e.*, $r = [1.1 \ 1.1 \ 60]^\top$. This is to force system operation at the maximum allowed pressure of 60 bar, while the vapor fractions are maintained at 1.1.

Next, the model predictive control problem is expressed as the following optimization problem.

Problem 4.5.1.

$$\min_{\Delta u(k), \dots, \Delta u(k+N_u-1), \epsilon} J(k) \quad (4.10)$$

subject to (4.7) and

$$\begin{aligned} u^{min} &\leq u(k+i) \leq u^{max}, \\ y^{min} - \epsilon V^{min} &\leq y(k+i+1), \quad i = 0, \dots, N_y - 1 \end{aligned} \quad (4.11)$$

where the weight V^{min} quantifies the relaxation of the output constraints. As V^{min} becomes larger, the constraint is softer while for $V^{min} = 0$ the constraint is hard and cannot be violated. Here, V^{min} is a positive number such that optimization Problem 4.5.1 remains feasible even if the output constraints are not satisfied, *e.g.*, during the heat-up period. The computed control input is $u(k) = u(k-1) + \Delta u^*(k)$, where $\Delta u^*(k)$ is the first element of the optimal sequence obtained by solving (4.10).

4.6 Simulation results

In this section, the proposed MPC strategy is applied on the fully decoupled WHR system architecture (expander and pumps decoupled from the engine). A comparison

is made with the benchmark configuration (expander and pumps fully coupled) and coupled architecture (expander coupled, pumps decoupled). The switching MPC strategy is tested on both steady-state and dynamic behavior from the World Harmonized Transient Cycle (WHTC). The simulation results are performed using real disturbances from a Euro VI heavy-duty diesel engine with the benchmark WHR system architecture. The MPC strategy is implemented in Matlab[®] using the *Model Predictive Control Toolbox*.

The input and output constraints are defined as:

$$u^{min} = \begin{bmatrix} 50 \\ 50 \\ 500 \end{bmatrix}, u^{max} = \begin{bmatrix} 2500 \\ 2500 \\ 2500 \end{bmatrix}, y^{min} = \begin{bmatrix} 1.05 \\ 1.05 \\ 1 \end{bmatrix}. \quad (4.12)$$

In (4.12), note that the output constraints are between one and the set reference. This is to penalize the cost function before the vapor fraction reaches the two-phase state. Furthermore, the minimum pumps speed is set to a positive value to allow a certain mass flow rate through the pumps and avoid evaporators dry out.

A controller sampling rate of 0.4 s is chosen, which yields an acceptable approximation of the system dynamics. The prediction horizon is $N_y = 45$ (18 s) and control horizon $N_u = 4$ (1.6 s). The prediction horizon is chosen such that it captures the system dynamics, while the control horizon is chosen small since larger values do not improve the performance considerably. For each region 1, 2, 3, the weighting matrices are: $W_y^1 = W_y^3 = \text{diag}(0.2, 0.2, 0.1)$, $W_y^2 = \text{diag}(0.1, 0.1, 0.1)$, and $W_{\Delta u}^1 = W_{\Delta u}^2 = \text{diag}(3, 2, 9)$, $W_{\Delta u}^3 = \text{diag}(2, 2, 3)$. These parameters are normalized weights applied to the scaled inputs and outputs (defined by the maximum value), such that all variables have similar magnitude within the optimization problem. For output constraints softening, a parameter $V^{min} = 40$ is used. The controller parameters are tuned on transitions between steady-state operating points shown in Fig. 4.3a. The tuning is performed to obtain fast disturbance rejection and constraints satisfaction over the whole system operating region. However, we show that these parameters provide good results, also during the transient behavior from the WHTC.

4.6.1 Steady-state results

In Fig. 4.7, the steady-state results for each WHR system architecture is illustrated. Compared to the benchmark, a small output power gain can be seen for the coupled architecture that considers the pumps disconnected from the engine. This indicates that the pumping power is small with respect to the expander power.

For the decoupled configuration, up to 20 – 30% improvement can be seen for 10

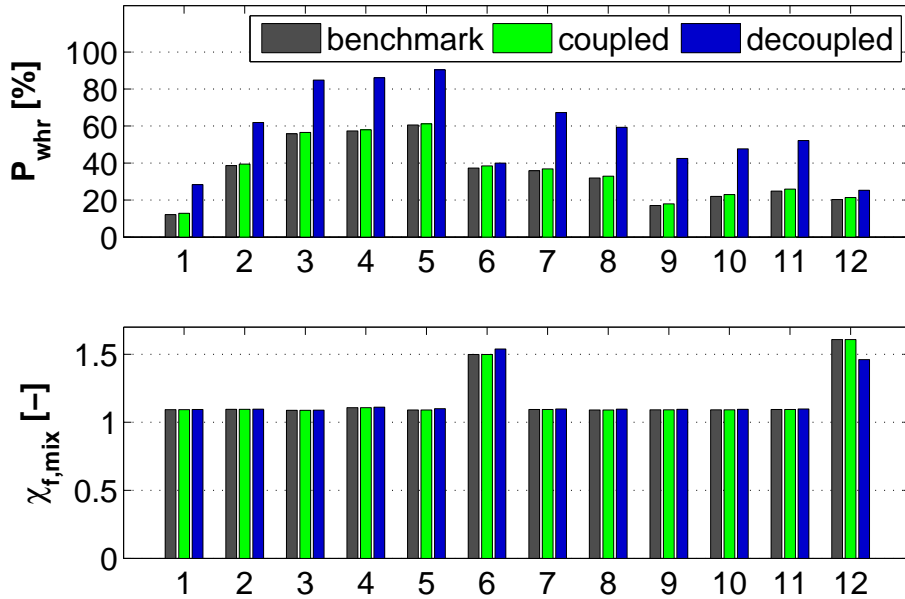


Figure 4.7: Steady-state comparison between different architectures: benchmark (expander and pumps coupled to the engine), coupled (expander coupled, pumps decoupled) and decoupled (expander and pumps decoupled).

points within the WHR system operating area. The output power values are expressed relative to the maximum power. The increase in power is due to the additional degree of freedom given by the expander speed. From the safety point of view, the differences are insignificant for studied cases, as $\chi_{f,mix}$ indicates vapor for all WHR system configurations.

4.6.2 Transient results

To verify the potential of the output power increase during transients, a hot-start WHTC is used. The WHTC is a highly transient cycle that covers typical driving conditions: urban, rural and highway. For the hot-start, the working fluid initial condition before the expander is 200°C. In Fig. 4.8, the disturbances (heat flow rates and engine speed) from hot-start engine conditions and switching signal are shown. Due to a highly dynamic exhaust gas mass flow rate, the engine heat flow rates are subject to sudden changes (response time less than 1 s). However, by using hysteresis, the resulting switching minimum dwell time is 5 s. Note that for this cycle region 3 is not reached. The reason for designing a controller also for region 3 is to cover the situation of high-load engine run, which can lead to operation in region 3 as it can be seen from the steady-state measurements.

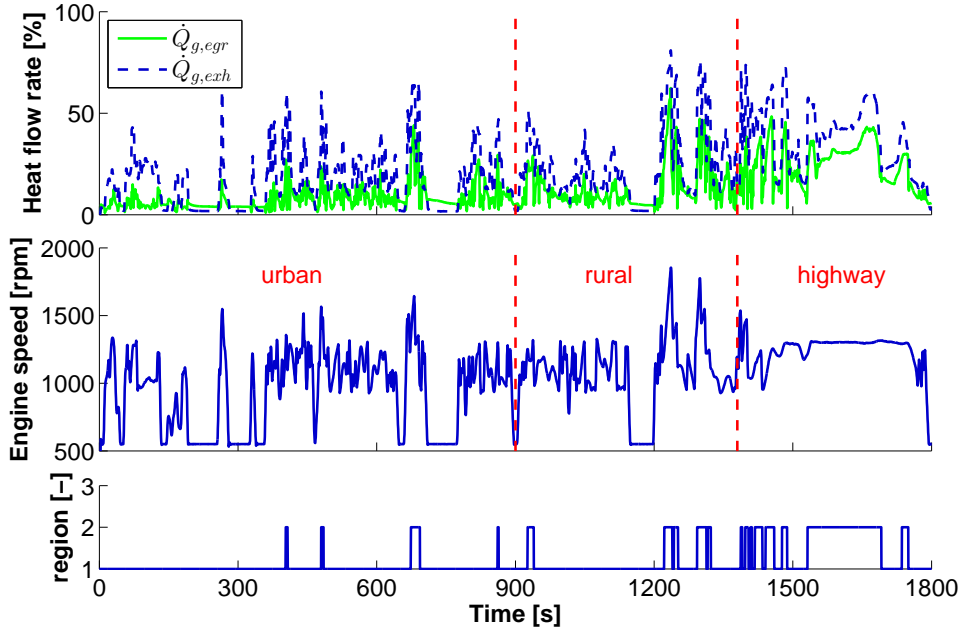


Figure 4.8: Disturbances from a hot-start World Harmonized Transient Cycle (WHTC) and switching signal.

In Fig. 4.9 for clarity, we compare the results for the coupled and the decoupled WHR system architectures, since the output power for the benchmark architecture do not significantly differ from the coupled expander case.

Two output signals are compared: the WHR net output power and the vapor fraction after the mixing junction. The computed control inputs are shown in Fig. 4.10. To quantify the performance of both architectures the following indices are used: the time in vapor t_v , *i.e.*, the cumulated time where $\chi_{f,mix} \geq 1$, and the recovered thermal energy U , where $U = \int_0^{t_v} P_{whr}(t)dt$. For each driving conditions, urban, rural, highway and cumulated, these performance indices are summarized in Table 4.1. The time in vapor is slightly larger for the coupled configuration. Mainly this is because the coupled WHR system operates at a lower pressure. By manipulating the expander speed, the decoupled architecture increases the chance of creating vapor, see Fig. 4.9 between 100 – 400 s. However, due to the slow expander transient behavior, the decoupled architecture can result in a lower output power as compared to the coupled architecture. This can be seen in Fig. 4.9, between 400 – 800 s.

In terms of recovered thermal energy, the decoupled WHR system architecture becomes superior for driving conditions with high heat flow rate. Especially during the highway driving, up to 28% more thermal energy recovery is seen for the decoupled WHR system configuration. The cumulated relative energy potential improvement is up to 29%.

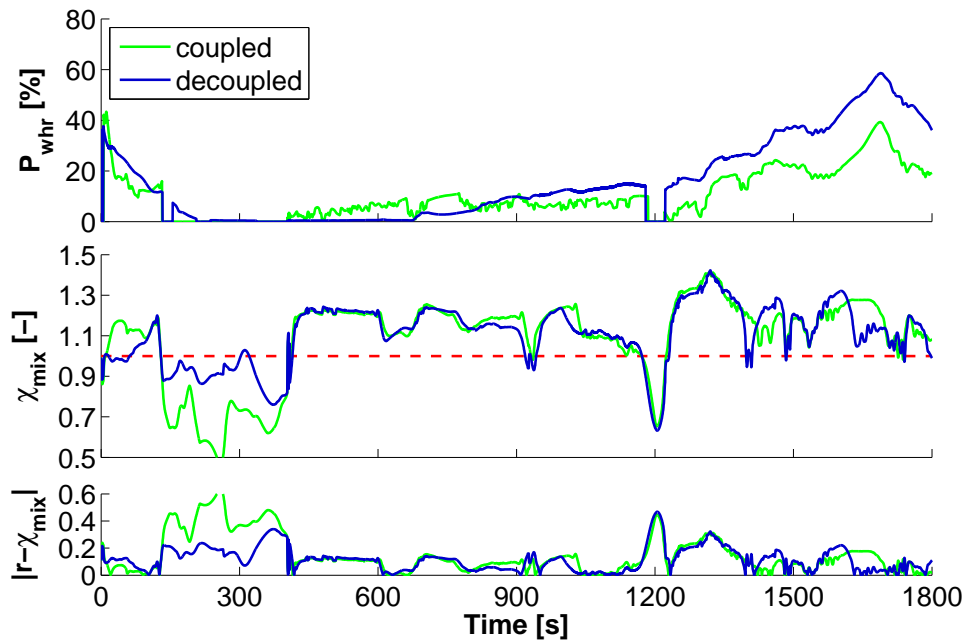


Figure 4.9: Comparison between the coupled and decoupled WHR system for a hot-start WHTC.

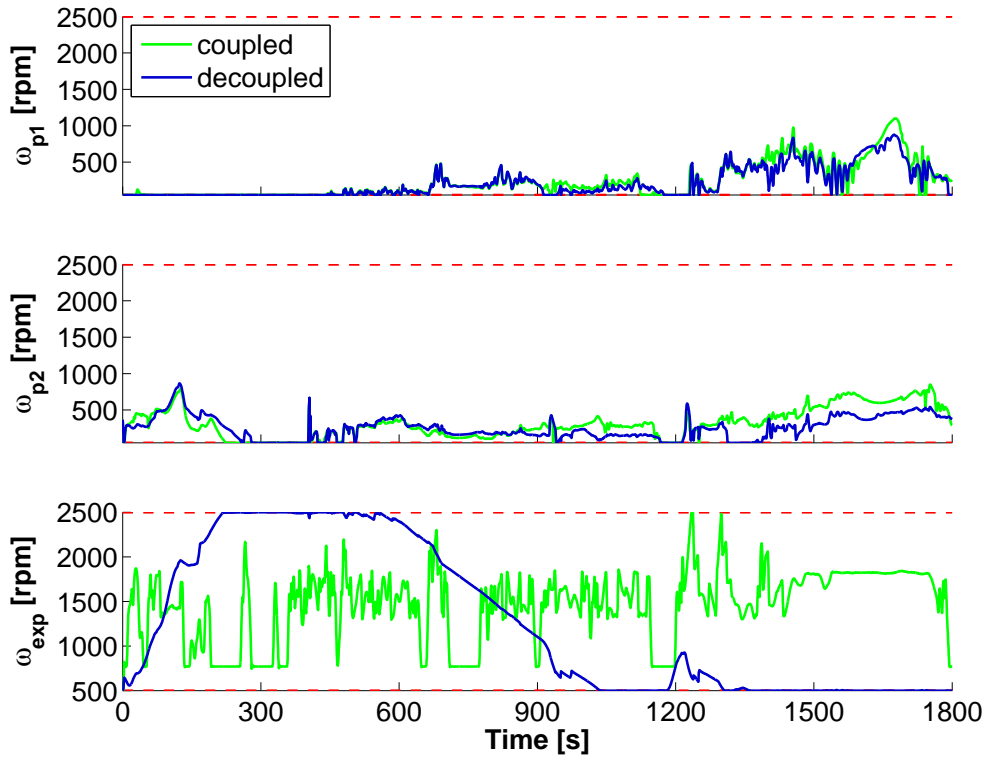


Figure 4.10: Control inputs for a hot-start WHTC.

Table 4.1: Performance indices in terms of vapor time and recovered thermal energy expressed relative to the decoupled system configuration.

	urban time energy	rural time energy	highway time energy	cumulated time energy
coupled	610s 19%	420s 14%	417s 38%	1447s 71%
decoupled	583s 10%	400s 24%	405s 66%	1388s 100%
Gain	-27s -9%	-20s 10%	-12s 28%	-59s 29%

4.7 Conclusions

In this chapter, a Model Predictive Control strategy was presented for a Waste Heat Recovery system for automotive applications. The objective was to maximize WHR system output power while guaranteeing safe operation under highly dynamic engine disturbances. To achieve these objectives over the complete engine operating range, a switching MPC strategy was proposed. The proposed MPC strategy showed good disturbance rejection properties and output constraints satisfaction. The MPC strategy was shown to deal with both coupled and decoupled WHR system designs. The decoupled expander design outperforms the coupled design by 29% in terms of output power for real-world driving conditions from a World Harmonized Transient Cycle.

Future work will focus on combining the supervisory control strategy [32] for the proposed low-level MPC control strategy and decoupled WHR system configuration.

Integrated Powertrain Control¹

Abstract This chapter presents an integrated energy and emission management strategy, called Integrated Powertrain Control (IPC), for a Euro-VI diesel engine with an electrified waste heat recovery system. This strategy optimizes the CO₂-NO_x trade-off by minimizing the operational costs associated with fuel consumption, AdBlue dosage, and active particulate filter regeneration, while satisfying the tailpipe emission constraints. In simulations, the proposed control strategy is applied to different powertrain configurations: with and without waste heat recovery (WHR) system and WHR system equipped with a battery for energy storage. The potential of each studied configuration is evaluated over the World Harmonized Transient Cycle for cold-start and hot-start conditions. Compared to a baseline (Euro VI engine without WHR system), it is shown in simulations that the optimal IPC strategy with an electrified WHR system and battery provides an additional 3.5% CO₂ emissions reduction, while satisfying the NO_x emission constraint.

5.1 Introduction

With the introduction of the new emission standards in Europe, USA and Japan, the tailpipe pollutant emissions (CO, HC, NO_x, PM) of current heavy-duty diesel engines are forced towards near zero impact level. To achieve this goal, several measures have been taken, such as augmenting conventional engines with common rail fuel injection equipment, advanced turbocharging, exhaust gas recirculation and aftertreatment systems. In addition, the automotive industry is focusing on improving the fuel efficiency and, as a result, also reducing CO₂ emissions. However, fuel consumption remained

¹This chapter is based on [45].

nearly unchanged during the last two decades [2]. A promising way for improving fuel economy can be obtained by vehicle hybridization [65–67]. Using this approach, the pollutants need to be analyzed carefully, since a diesel hybrid electric vehicle can improve the fuel economy, but in the same time can emit more pollutants than a conventional vehicle [68]. A way to cope with pollutant constraints is by synthesizing an integrated energy and emission management strategy [69, 70].

Apart from vehicle hybridization, another promising solution to further reduce fuel consumption and to meet future CO₂ emission legislation is to use a Waste Heat Recovery (WHR) system [31, 71, 72]. This system converts the engine exhaust gas heat energy into mechanical energy useful for propulsion or for electrical power generation [51]. The WHR system can be based on the Rankine cycle (RC) or on the organic Rankine Cycle (ORC). The difference between ORC and RC is that the ORC uses instead of water an organic fluid, which is better adapted to low-temperature heat sources.

Most of the studies on engines with WHR system are focused on low-level WHR system control [13, 21, 33]. Only a few studies deal with overall powertrain system performance with WHR systems [10, 32]. In [10], the fuel saving potential for a passenger vehicle with a RC WHR system is presented. The study shows the restrictions on WHR system power output due to the vehicle integration, the on-board electric system architecture, package considerations, increased weight, cooling demand, and exhaust gas backpressure. All these aspects can lead to a reduction of the fuel saving potential that can be achieved using a WHR system.

Optimizing the overall engine-aftertreatment-WHR system performance is a challenging task. This is due to interaction between the subsystems, highly dynamic nature of the driving cycle, different time constants of subsystems, nonlinearities, and constraints. In [32], a cost-based optimization strategy is presented. This strategy integrates energy and emission management, the so-called Integrated Powertrain Control (IPC), by minimizing the total operational cost, while explicitly taking into account the tailpipe emission constraints set by legislation. The operational cost to be optimized consists of the cost for fuel, AdBlue dosage, and the fuel costs associated with active Diesel Particulate Filter regeneration.

In this chapter, we extend the integrated energy and emission management from [32] to a heavy-duty diesel engine with an electrified WHR system. Compared to a non-electrified one, the advantages of an electrified WHR system are:

- (i) the possibility to store energy for latter usage using a battery;

- (ii) increased flexibility for WHR power output manipulation;
- (iii) easy integration within a hybrid electric vehicle to further increase fuel saving potential.

Here, a complete powertrain model is used that consists of the following components: a heavy-duty diesel engine with aftertreatment model [32], a complete WHR system model (see Chapter 3) with decoupled expander configuration, and an electric system (motor, generator and battery). The low-level WHR system control strategy, that is used, has been presented in Chapter 4.

This chapter is organized as follows. In Section 5.2, the studied powertrain is described. Section 5.3 and Section 5.4 present the high-fidelity simulation model and the control model, respectively. In Section 5.5, the control problem is formulated and the proposed IPC strategies are presented. The simulation results are compared with the baseline strategy in Section 5.6. Finally, conclusions are drawn in Section 5.7.

5.2 System description

In Fig. 5.1, a schematic representation of the studied system is illustrated. It is based on a state-of-the-art 12.9 l, 6 cylinder, 375 kW Euro-VI diesel engine. This engine is equipped with a common rail injection system, a turbocharger with Variable Turbine Geometry (VTG), Charge Air Cooling (CAC) and an Exhaust Gas Recirculation (EGR) system. To meet Euro-VI emission legislation, an exhaust gas aftertreatment system is installed. This aftertreatment system consists of a Diesel Oxidation Catalyst (DOC), a Diesel Particulate Filter (DPF) and an urea-based Selective Catalytic Reduction (SCR) system with an Ammonia Oxidation catalyst (AMOX) [73]. The DPF is used to filter out particulates from the exhaust flow. Periodically, the trapped particulates are oxidized by injecting fuel upstream of the DOC. As a result, the exhaust gas temperature is increased. This process is called DPF regeneration. The NO_x emissions downstream of the DPF system are converted into harmless products over the Cu-Zeolite SCR catalyst. This catalytic process requires ammonia (NH_3). The ammonia is formed by decomposing the injected urea solution (AdBlue) in the hot exhaust gases, upstream the SCR. To avoid unacceptable ammonia slip, an AMOX catalyst is used.

In this study, an ORC-based Waste Heat Recovery (WHR) system is added to the engine. This WHR system recovers heat from both the EGR line and the line downstream of the aftertreatment system, where the EGR evaporator replaces the standard EGR cooler. The exhaust gas heat is used to create vapor at the outlet of both

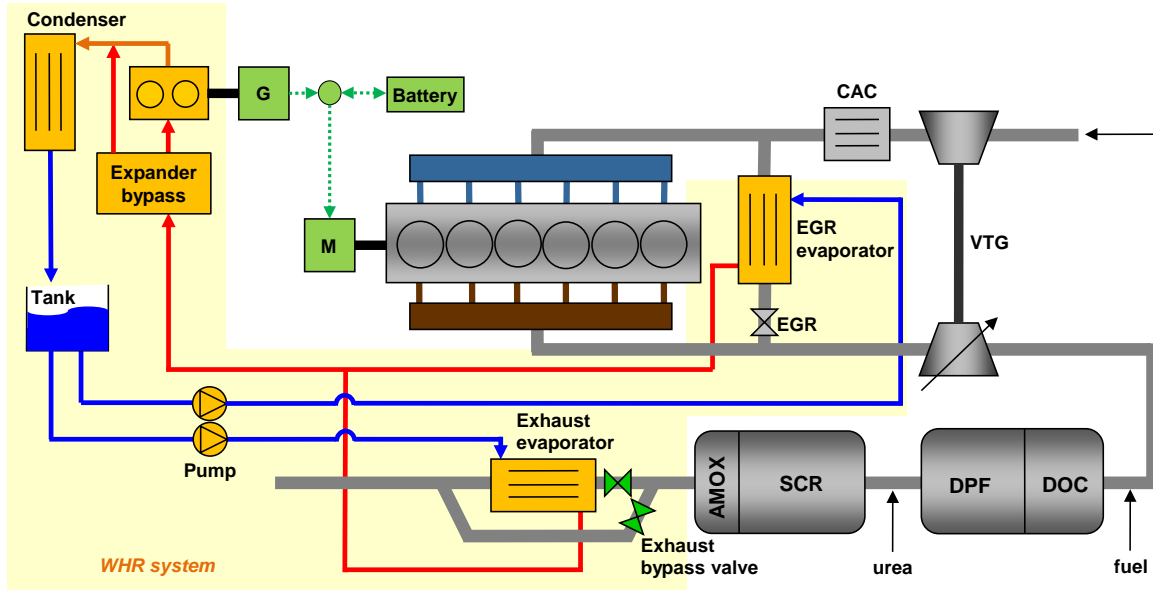


Figure 5.1: Studied Euro-VI engine with aftertreatment and an electrified WHR system. The aftertreatment consists of a Diesel Oxidation Catalyst (DOC), a Diesel Particulate Filter (DPF), Selective Catalytic Reduction (SCR), and an Ammonia Oxidation catalyst (AMOX). The WHR system consists of two parallel evaporators and a two-piston expander to convert the exhaust gas heat into mechanical power. The engine is assisted by a motor (M) that receives electrical power from a generator (G) and a battery.

counter-flow evaporators. The working fluid is pure ethanol due to its thermodynamic properties suitable for this low-temperature application. The ethanol flow through each evaporator is individually manipulated by two electric pumps. A two-piston expander converts the recovered thermal energy into mechanical energy. To close the cycle, a condenser is used that brings the ethanol back to its liquid phase. In case the condenser cooling capacity is exceeded, the exhaust gases before the exhaust evaporator are bypassed using the proportional exhaust bypass valve. The tank is assumed to be ideal, providing ethanol at a constant temperature and pressure. Furthermore, an on/off expander bypass is present for two reasons: first, to avoid liquid flow into the expander cylinders when vapor state cannot be realized (*e.g.* during start-up) and second, to reduce the expander power in case there is no power demand and the battery is fully charged. For safety reasons when the pressure exceeds 60 bar, a pressure relief valve is activated.

The expander mechanical power drives an electric generator (G). The generated electrical energy is then used to charge a battery or to drive an electric motor (M)

which is directly coupled to the engine crank shaft. Note that in order to assess the fuel economy achieved solely by the WHR system, energy recovery during vehicle braking (regenerative braking) is not considered here.

In this chapter, the following six cases are analyzed and compared:

- *Baseline*: engine with aftertreatment system. The control strategy mimics the control of a Euro-VI heavy-duty diesel engine.
- *Recal WHR*: engine with aftertreatment and a WHR system without battery. The engine control parameters are tuned off-line (recalibration).
- *Recal battWHR*: engine with aftertreatment and a WHR system augmented with a battery for energy storage. The engine control parameters are tuned (recalibration). The battery management is realized using a rule based strategy given in Appendix B.1;
- *IEM*: engine with aftertreatment system. The integrated energy management (IEM) uses the baseline hardware platform, for which the engine settings are optimized on-line to meet the tailpipe emission constraints;
- *IPC WHR*: engine with aftertreatment and a WHR system. The integrated powertrain control (IPC) optimizes the engine, aftertreatment and WHR system such that the tailpipe emission constraints are satisfied;
- *IPC battWHR*: engine with aftertreatment and a WHR system equipped with a battery for energy storage. This strategy is based on the IPC WHR, but augmented with an optimized battery energy management system;

5.3 Simulation model

The simulation model represents the complete powertrain model. It contains validated engine, aftertreatment and WHR system models. Furthermore, a battery, a motor and a generator model are included. In what follows, these models are described in detail.

5.3.1 Engine

In this application, the engine is considered to be a static component as compared to the aftertreatment, WHR system and battery. This is motivated by the fact that the engine time constant is much smaller than the time constant of the other mentioned

subsystems. The engine behavior is described by eight static 4D maps, with the engine speed ω_E , engine brake torque τ_E without motor, EGR valve position u_{EGR} , and VTG valve position u_{VTG} as inputs:

$$\begin{aligned} & \{\dot{m}_{fl}, \dot{m}_{EGR}, T_{EGRin}, T_{EGRout}, \dot{m}_{exh}, T_{exh}, \dot{m}_{NO_x}, \dot{m}_{PM}\} \\ & = f_i(\omega_E, \tau_E, u_{EGR}, u_{VTG}), \quad i = 1, \dots, 8, \end{aligned} \quad (5.1)$$

where \dot{m}_{fl} is engine fuel mass flow that realizes the requested brake torque, *i.e.*, $\tau_{req} = \tau_E$, and \dot{m}_{EGR} , T_{EGRin} and T_{EGRout} are EGR mass flow and temperature in and out the EGR evaporator, respectively. Furthermore, \dot{m}_{exh} and T_{exh} are exhaust gas mass flow and temperature, \dot{m}_{NO_x} represents the engine out NO_x mass flow and \dot{m}_{PM} is the engine out particulate matter mass flow. These engine maps are constructed using a validated dynamic mean-value engine model without a WHR system. The effect of changing ambient conditions is not considered, the engine model is derived at an ambient temperature and pressure of 20°C and 1 bar, respectively.

5.3.2 Aftertreatment system

To simulate the DOC, DPF and SCR system a high-fidelity validated aftertreatment model is used. The model consists of one-dimensional submodels of a pipe with urea decomposition, pre-oxidation catalyst (DOC), diesel particulate filter (DPF), SCR catalyst, and ammonia oxidation (AMOX) catalyst. The catalyst models are based on first principle modeling using mass and energy balances. In these models, the catalysts are divided in segments to describe the spatial distribution of pressure, temperature and chemical components. More details about the aftertreatment modeling approach can be found in [73].

5.3.3 Waste Heat Recovery system

The WHR system model is developed using a component-based approach. It consists of a reservoir, pumps, valves, evaporators, condenser, and an expander model. The pumps, valves and expander are modeled as stationary components, while the evaporators and condenser are based on mass and energy conservation principles:

Conservation of mass (working fluid):

$$V_f \frac{\partial \rho_f}{\partial t} + L \frac{\partial \dot{m}_f}{\partial z} = 0. \quad (5.2)$$

Conservation of energy (exhaust gas and working fluid):

$$\rho_g c_{pg} V_g \frac{\partial T_g}{\partial t} = c_{pg} \dot{m}_g L \frac{\partial T_g}{\partial z} - \alpha_g S_g (T_g - T_{wg}) - \dot{Q}_{loss}, \quad (5.3a)$$

$$\rho_f V_f \frac{\partial h_f}{\partial t} = -\dot{m}_f L \frac{\partial h_f}{\partial z} + \alpha_f S_f (T_{wf} - T_f) \quad (5.3b)$$

Conservation of energy (at the wall):

$$\rho_w c_{pw} \gamma_w V_w \frac{\partial T_{wg}}{\partial t} = \alpha_g S_g (T_g - T_{wg}) - \frac{\kappa_w S_w}{\delta_w} (T_{wg} - T_{wf}), \quad (5.4a)$$

$$\rho_w c_{pw} (1 - \gamma_w) V_w \frac{\partial T_{wf}}{\partial t} = -\alpha_f S_f (T_{wf} - T_f) + \frac{\kappa_w S_w}{\delta_w} (T_{wg} - T_{wf}), \quad (5.4b)$$

where z is the space coordinate along the length L of the evaporator, V_f , V_g and V_w are the volumes occupied by the working fluid, by the exhaust gas, and by the wall, respectively. Furthermore, S is the surface area, c_p is the specific heat capacity, κ_w represents the wall thermal conductivity, and δ_w is the wall thickness. A constant factor γ_w is introduced in Eq. (5.4) to separate the mass of the wall, including fins on the exhaust side from the mass of the wall on the working fluid side. In Eq. (5.4), the transversal wall conduction is computed based on two temperature points T_{wg} and T_{wf} , one on the exhaust gas side and one on the working fluid side, respectively. The heat transfer coefficients on the exhaust gas side α_g and working fluid side α_f are based on Nusselt numbers correlations selected from [54]. The working fluid vapor fraction is computed as:

$$\chi_f = \frac{h_f - h_l(p_f)}{h_v(p_f) - h_l(p_f)}, \quad (5.5)$$

where $h_l(p_f)$ and $h_v(p_f)$ denote the specific saturated liquid and vapor enthalpy, respectively, as a function of system pressure p_f .

The piping after the evaporators is considered as a fixed volume. A pressure volume model is introduced to characterize the temperature and pressure dynamics inside the volume, as a function of the inlet and outlet conditions:

$$\frac{dm}{dt} = \dot{m}_{in} - \dot{m}_{out}, \quad (5.6a)$$

$$m \frac{dT}{dt} = b T_{in} + a T, \quad (5.6b)$$

$$m T \frac{dp}{dt} = (b T_{in} + a T) p + m T \frac{R}{V} (\dot{m}_{in} - \dot{m}_{out}), \quad (5.6c)$$

where V is the volume and R is the specific ideal gas constant. The expressions for a and b are defined as:

$$a = -\dot{m}_{in} - \left(\frac{c_p}{c_v} - 1 \right) \dot{m}_{out}, \quad b = \frac{c_p}{c_v} \dot{m}_{in}. \quad (5.7)$$

In (5.6), the working is assumed to be in vapor state. Under highly dynamic engine conditions, the working fluid reaches two-phase state. However, for normal operating conditions (excluding the start-up phase) this is only for short period of time and thus (5.6) still provides acceptable prediction accuracy [41].

The WHR system net power output is calculated by:

$$P_{WHR} = P_{exp} - P_{p1} - P_{p2}, \quad (5.8)$$

where P_{exp} is the expander power and P_{p1}, P_{p2} are the requested power to drive the pumps. More details about the evaporator model development and validation is described in [39], while the complete WHR system model is validated in [41].

5.3.4 Electric system

The motor is connected to the engine crankshaft and can deliver power to the vehicle driveline, while the generator is connected to the expander of the WHR system. The motor and generator can be modeled using affine expressions to account for drag losses [74]. However, here for simplicity, the motor and the generator are modeled using a constant efficiency η_M and η_G , respectively.

The battery pack is modeled as a series connection of n battery cells with an internal resistance R and nominal voltage U_{oc} . By considering quadratic losses, the battery pack power at the terminals P_B can be expressed as [74]:

$$P_B = P_S - \beta P_S^2, \quad \beta = \frac{R}{nU_{oc}^2}. \quad (5.9)$$

The energy in the battery E_B can be written as:

$$\dot{E}_B = -P_S, \quad (5.10)$$

where the internal battery power P_S and energy E_B are limited, i.e.,

$$P_S \in [P_{Smin}, P_{Smax}], \quad (5.11)$$

$$E_B \in [0, E_{Bmax}]. \quad (5.12)$$

The battery state of energy (SOE) is defined as:

$$\text{SOE} = \frac{E_B}{E_{Bmax}}, \quad (5.13)$$

where E_{Bmax} is the maximum battery energy that can be stored in the battery.

The generator, motor, and battery are connected as follows:

$$P_G = \eta_G P_{WHR} \quad (5.14)$$

$$P_M = \eta_M (P_G + P_B), \quad (5.15)$$

where P_{WHR} is the WHR system net power output.

5.4 Control model

In this section, the control model used in the optimal control strategy is presented. The control model for the engine, motor, generator and battery are identical to the simulation model. For the aftertreatment model and WHR system, a simplified representation is used within the control model. The control model dynamic behavior is given by:

$$\dot{T}_{DOC} = c_1 \dot{m}_{exh} (T_{exh} - T_{DOC}), \quad (5.16)$$

$$\dot{T}_{SCR} = c_2 \dot{m}_{exh} (T_{DOC} - T_{SCR}) - c_3 (T_{SCR} - T_{amb}), \quad (5.17)$$

$$\dot{m}_{NO_x tp} = \dot{m}_{NO_x} (1 - \eta_{SCR}), \quad (5.18)$$

$$\dot{P}_{WHR} = \frac{1}{\zeta_{WHR}} \left(\eta_{WHR} (\dot{Q}_{EGR} + \dot{Q}_{exh}) - P_{WHR} \right), \quad (5.19)$$

$$\dot{E}_B = -P_S. \quad (5.20)$$

where, c_1 , c_2 , c_3 are constants specified in Table 5.1 and $\dot{m}_{NO_x tp}$ represents the NO_x emissions at the tailpipe.

The thermal behavior of the aftertreatment system is lumped using two differential equations (5.16) and (5.17), that model the DOC temperature T_{DOC} and the SCR temperature T_{SCR} . In (5.18), the SCR conversion efficiency η_{SCR} is a function of the SCR temperature T_{SCR} , the space velocity v_S and the DOC efficiency η_{DOC} , i.e., $\eta_{SCR} = g(T_{SCR}, v_S, \eta_{DOC})$. The space velocity v_S [1/s] is expressed as:

$$v_S = \frac{\dot{m}_{exh}}{\rho_{exh} V_{SCR}}, \quad (5.21)$$

where ρ_{exh} is the exhaust gas density at ambient conditions and V_{SCR} is the SCR catalyst volume. The DOC efficiency η_{DOC} is shown in Fig. 5.2a as a function of T_{DOC} and v_S . The SCR efficiency η_{SCR} (see Fig. 5.2b) is computed by interpolating between three stationary maps for different DOC efficiencies $\eta_{DOC} = [0, 0.5, 1]$.

The WHR system net power output P_{WHR} is approximated by a first-order model with an average time constant ζ_{WHR} . Fig. 5.3 illustrates the stationary WHR system

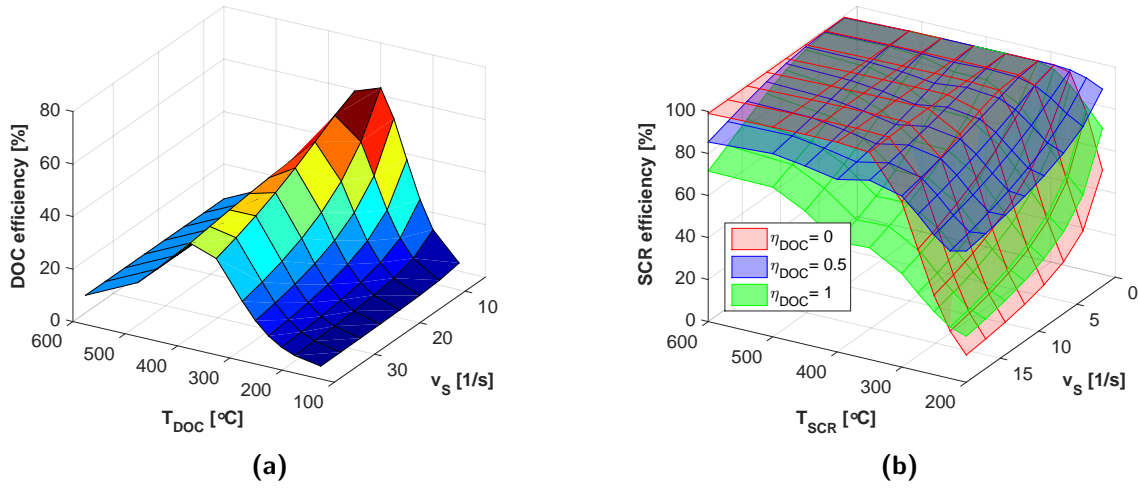


Figure 5.2: (a) DOC efficiency map η_{DOC} . (b) SCR conversion efficiency for three different values of η_{DOC} .

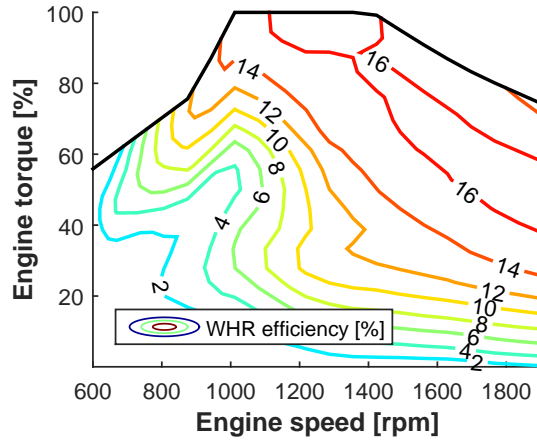


Figure 5.3: Stationary WHR system efficiency map η_{WHR} , obtained by running the simulation model for 20 by 20 grid points, distributed over the complete engine speed and torque values. For the WHR system, the pumps and expander speed settings are realized by the low-level WHR system control.

efficiency map η_{WHR} , obtained using the high-fidelity validated simulation model. The average time constant ζ_{WHR} is obtained by fitting (5.19) to the simulation model output over a representative real-world diving cycle. The EGR and exhaust heat flow rates are

given by:

$$\dot{Q}_{EGR} = \dot{m}_{EGR} c_{pEGR} (T_{EGRin} - T_{EGRout}), \quad (5.22a)$$

$$\dot{Q}_{exh} = \dot{m}_{exh} c_{pexh} (T_{SCR} - T_{tp}), \quad (5.22b)$$

where \dot{m}_{EGR} , T_{EGRin} , T_{EGRout} and \dot{m}_{exh} are from (5.1) and T_{tp} is taken as the ambient temperature, *i.e.*, $T_{tp} = T_{amb}$.

5.5 Control strategy

In Fig. 5.4, a schematic representation of the proposed engine control system is shown. It consists of the engine maps for fueling, two low-level controllers and a supervisory control strategy. The low-level controllers are: the urea dosing control strategy and the WHR control system. The supervisory control strategy objective is to determine the settings for the u_{EGR} , u_{VTG} , and P_S , such that operational costs are minimized subject to input, state and emission constraints. For this control strategy, we assume that the cooling capacity of the WHR system is not exceeded. Therefore, the exhaust bypass valve u_{g2} is always fully closed ($u_{g2} = 0\%$).

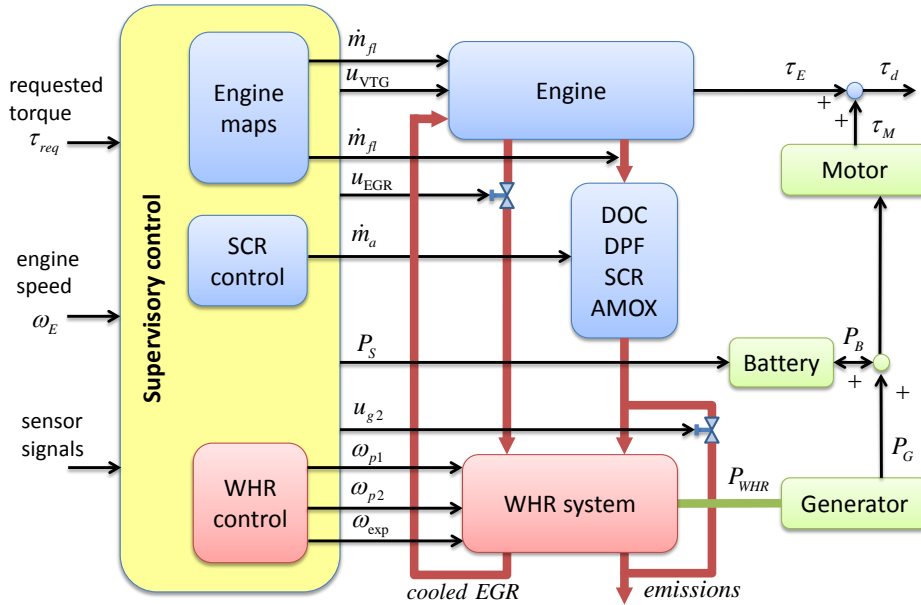


Figure 5.4: Schematic representation of the integrated powertrain control with an electrified WHR system. The supervisory strategy computes the engine settings u_{EGR} and u_{VTG} and the internal battery power P_S .

By assuming ideal torque management, the mechanical torque balance reads:

$$\tau_E = \tau_{req} - \tau_M, \quad \tau_M = \frac{P_M}{\omega_E}, \quad (5.23)$$

where τ_{req} is the requested torque and τ_M is the torque delivered by the electric motor.

5.5.1 Low-level SCR control

The low-level SCR controller determines the required AdBlue dosing \dot{m}_a . To this end, a model-based ammonia storage controller is used. An SCR catalyst model is used to estimate in real-time the ammonia storage θ from the SCR catalyst temperature T_{SCR} and pre-SCR NO_x emissions \dot{m}_{NO_x} . This estimated value is compared with a reference value θ_{ref} , calibrated for the standard Euro-VI engine. The difference between θ_{ref} and θ is fed to a PID controller. By controlling θ , we aim to achieve high NO_x conversion efficiency and avoid excessive NH_3 slip in case of a sudden temperature increase. A detailed description of this low-level SCR control can be found in [75].

5.5.2 Low-level WHR control

The low-level WHR system control computes the pumps speed ω_{p1} and ω_{p2} and the expander speed ω_{exp} . The objective is to maximize the WHR system net output power P_{WHR} , while satisfying the safety requirements in the presence of highly dynamic engine disturbances. These disturbances are known represented by the engine heat flow rates \dot{Q}_{EGR} and \dot{Q}_{exh} defined in (5.22). The system operates safely if the WHR system produces vapor, *i.e.*, $\chi_f \geq 1$ from (5.5). The presence of droplets after the heat exchangers can lead to liquid flow into the expander cylinders and eventually damage of the system. In order to avoid these critical situations, a switching model predictive control (MPC) strategy is implemented. The switching is performed using three different models, each linearized around a representative engine operating point. More details can be found in [44].

5.5.3 Optimal IPC strategy

The main focus of this section is to design a supervisory controller that optimizes the complete powertrain. To formulate the optimization problem, let us write the control

model using the general form:

$$\dot{x} = f(x, u, t), \text{ with } u = \begin{bmatrix} u_{EGR} \\ u_{VTG} \\ P_S \end{bmatrix}, \text{ and } x = \begin{bmatrix} T_{DOC} \\ T_{SCR} \\ m_{NO_{x,tp}} \\ P_{WHR} \\ E_B \end{bmatrix}. \quad (5.24)$$

Note that by introducing an electrified WHR system, the torque delivered by the engine τ_E becomes a function of the motor torque τ_M . Furthermore, substituting (5.14) and (5.15) in (5.23), the engine torque τ_E becomes a function of the current WHR system power P_{WHR} and the input battery power P_S . Then, the dependencies in the control model can be written as:

$$\dot{x} = \begin{bmatrix} c_1 \dot{m}_{exh}(x_4, u) (T_{exh}(x_4, u) - x_1) \\ c_2 \dot{m}_{exh}(x_4, u) (x_1 - x_2) - c_3 (x_2 - T_{amb}) \\ \dot{m}_{NO_x}(x_4, u) (1 - \eta_{SCR}(x_1, x_2, x_4, u)) \\ \frac{1}{\zeta_{WHR}} \left(\eta_{WHR} \left(\dot{Q}_{EGR}(x_4, u) + \dot{Q}_{exh}(x_2, x_4, u) \right) - x_4 \right) \\ -u_3 \end{bmatrix} \quad (5.25)$$

The cost function to be optimized consists of a weighted sum between the fuel consumption \dot{m}_{fl} , the AdBlue mass flow \dot{m}_a and an equivalent cost associated with the fuel consumption for active DPF regeneration \dot{m}_{PM} . The AdBlue mass flow \dot{m}_a is obtained by assuming that all injected urea decomposes in ammonia and is available for NO_x conversion. Therefore, the desired AdBlue dosage \dot{m}_a is expressed as:

$$\dot{m}_a = c_4 \eta_{SCR} \dot{m}_{NO_x}. \quad (5.26)$$

The engine-out NO_x emissions \dot{m}_{NO_x} and the fuel mass flow \dot{m}_f are determined from the engine steady-state maps (5.1). The weights denoted with π_{fl} , π_a and π_{PM} are the diesel price, AdBlue price and fuel cost for accumulated soot, respectively. Hence, the optimization problem can be formulated as follows:

Problem 5.5.1.

$$\min_u \int_0^{t_f} (\pi_{fl} \dot{m}_{fl}(x, u, t) + \pi_a \dot{m}_a(x, u, t) + \pi_{PM} \dot{m}_{PM}(x, u, t)) dt \quad (5.27)$$

$$s.t. (\forall t \in [0, t_f]), (5.1) \text{ and } (5.25) \quad (5.28a)$$

$$\tau_d = \tau_E + \tau_M, \quad \tau_M = \frac{P_M}{\omega_E} \quad (5.28b)$$

$$P_M = \eta_M(P_G + P_B) \quad (5.28c)$$

$$P_G = \eta_G P_{WHR} \quad (5.28d)$$

$$P_B = P_S - \beta P_S^2 \quad (5.28e)$$

$$P_S \in [P_{Smin}, P_{Smax}] \quad (5.28f)$$

$$E_B \in [0, E_{Bmax}] \quad (5.28g)$$

$$E_B(0) = E_B(t_f) = E_{B0} \quad (\text{battery charge sustaining constraint}) \quad (5.28h)$$

$$P_M \in [P_{Mmin}, P_{Mmax}] \quad (5.28i)$$

$$\tau_E \in [0, \tau_{Emax}(\omega_E)] \quad (5.28j)$$

$$m_{NO_{x,tp}}(t_f) \leq Z_{NO_x} \int_0^{t_f} P_d dt \quad (\text{tailpipe limit for WHTC}) \quad (5.28k)$$

A solution of Problem 5.5.1 can be obtained by using Pontryagin's minimum principle [76, 77]. The principle is based on minimization of the Hamiltonian:

$$H(x, \lambda, u, t) = \pi_{fl} \dot{m}_{fl}(x_4, u, t) + \pi_a \dot{m}_a(x_1, x_2, x_4, u, t) \\ + \pi_{PM} \dot{m}_{PM}(x_4, u, t) + \lambda^\top f(x, u, t). \quad (5.29)$$

The Hamiltonian entails the objective function from Problem 5.5.1 augmented with Lagrange multipliers λ and the state dynamics $f(x, u, t)$ from (5.25).

Pontryagin's minimum principle states the following: if $u^* \in \mathcal{U}$ is the optimal control input and x^* is the optimal state trajectory, then:

$$H(x^*, \lambda^*, u^*, t) \leq H(x^*, \lambda^*, u, t), \quad \forall u \in \mathcal{U}, \quad t \in [t_0, t_f], \quad (5.30)$$

where λ^* is the optimal trajectory of the Lagrange multipliers. At any optimal solution u^* , it holds:

$$\dot{\lambda}^* = - \left(\frac{\partial H(\cdot)}{\partial x} \right)^*. \quad (5.31)$$

This is a necessary condition at any local/global optimum, where the above mentioned derivatives are defined. Hence, the solution of Problem 5.5.1 can also be obtained by minimizing the Hamiltonian, *i.e.*,

$$\min_u H(\cdot) \quad (5.32)$$

$$s.t.: (5.28) \text{ and } \dot{\lambda} = - \frac{\partial H(\cdot)}{\partial x}. \quad (5.33)$$

The WHR system power is significantly less than the power delivered by the engine, *i.e.*, $P_{WHR} < 0.1P_E$. Thus, the derivatives with respect to WHR system power P_{WHR} of the engine temperature T_{exh} , exhaust gas flow \dot{m}_{exh} and NO_x emission flow \dot{m}_{NO_x} can be neglected. Then, the solutions of λ have to satisfy:

$$\dot{\lambda}_1 = (c_1\lambda_1 - c_2\lambda_2)\dot{m}_{exh}(x_4, u) + \frac{\partial\eta_{SCR}(x_1, x_2, x_4, u)}{\partial x_1}\dot{m}_{NO_x}(x_4, u)(\lambda_3 - c_4\pi_a) \quad (5.34a)$$

$$\dot{\lambda}_2 = (c_2\dot{m}_{exh}(x_4, u) + c_3)\lambda_2 + \frac{\partial\eta_{SCR}(x_1, x_2, x_4, u)}{\partial x_2}\dot{m}_{NO_x}(x_4, u)(\lambda_3 - c_4\pi_a) \quad (5.34b)$$

$$- \eta_{WHR}\frac{\partial\dot{Q}_{exh}(x_2, x_4, u)}{\partial x_2}\frac{1}{\zeta_{WHR}}\lambda_4$$

$$\dot{\lambda}_3 = 0 \quad (5.34c)$$

$$\dot{\lambda}_4 = \frac{1}{\zeta_{WHR}}\lambda_4 - \frac{\partial\dot{m}_f(x_4, u)}{\partial x_4}\pi_{fl} - \frac{\partial\dot{m}_a(x_1, x_2, x_4, u)}{\partial x_4}\pi_a - \frac{\partial\dot{m}_{PM}(x_4, u)}{\partial x_4}\pi_{PM} \quad (5.34d)$$

$$\dot{\lambda}_5 = 0 \quad (5.34e)$$

In (5.34a), (5.34b) and (5.34d), the coefficients of λ_1 , λ_2 and λ_4 , respectively, are positive. This is true for all engine operating conditions, since c_1 , c_2 , c_3 , \dot{m}_{exh} and ζ_{WHR} are positive. Hence, the dynamics of λ_1 , λ_2 and λ_4 are unstable. This makes the solution of the optimal control problem difficult to implement in practice, because it requires to integrate (5.34a), (5.34b) and (5.34d) backwards in time over the entire driving cycle. To overcome this, in what follows we present an approximation for the Lagrange multipliers, which can be easily implemented in practice.

5.5.4 Real-time IPC strategy

In this section, a real-time implementable solution is presented by approximating (5.34), such that it can be computed in real-time.

First, (5.34a) and (5.34b) are replaced by a heuristic rule that was proposed in [78]. This rule is illustrated in Fig. 5.5. It is parametrized by three constants λ_T , ΔT_1 and ΔT_2 , where $\Delta T = T_{DOC} - T_{SCR}$. The principle follows from the fact that the effort to heat up the aftertreatment system is proportional to SCR catalyst NO_x conversion inefficiency. When the DOC temperature is lower than the SCR temperature, it seems better to invest in raising the engine-out exhaust temperature rather than promoting the heat convection from DOC to SCR (which corresponds to a large λ_1). The converse holds

when the DOC temperature is higher than the SCR temperature (which corresponds to a large λ_2). To account for the WHR system dynamics, the Lagrange multiplier λ_4 in (5.34d) can be approximated by a constant [77]. This constant is tuned by numerical optimization over the considered cycle.

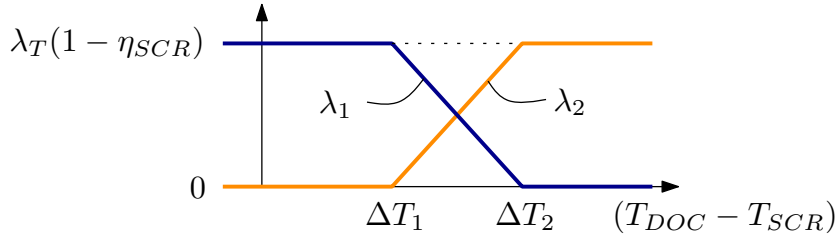


Figure 5.5: Heuristic rule for λ_1 and λ_2 [78].

Second, it should be noted that λ_3 and λ_5 have constant values along the driving cycle where derivative (5.33) is defined. Since the $m_{NO_{x,tp}}$ is monotonically increasing in time, the constraint (5.28k) is not activated intermittently. Hence, it is possible to obtain a single constant value for λ_3 . However, the battery state constraint (5.28h) may be activated several times along the driving cycle. Therefore, the optimal λ_5 is in fact a piecewise constant function with potentially different value after each time the battery constraint is activated. Operating with a constant Lagrange multiplier may activate the battery SOE limits, which leads to a suboptimal solution [79]. Therefore, λ_5 is allowed to deviate slightly from a reference λ_{5ref} as the battery SOE gets close to the limits. A typical approach to control λ_5 , is to apply a closed loop controller, such that the state value is kept in its feasible region [80, 81]. Based on a tangent function, here a proportional controller is used, defined as:

$$\lambda_5 = \lambda_0 - d_3 \tan(d_2 + d_1 \cdot \text{SOE}), \quad \text{where } \lambda_0 = \lambda_{5ref} + d_3 \tan(d_2 + d_1 \cdot \text{SOE}_{ref}), \quad (5.35)$$

and

$$d_1 = -\frac{\pi}{(\text{SOE}_{max} - \text{SOE}_{min})}, \quad (5.36a)$$

$$d_2 = \frac{\pi}{2} - d_1 \cdot \text{SOE}_{min}, \quad (5.36b)$$

$$d_3 = -Kp(\cos(d_2 + d_1 \cdot \text{SOE}_{ref}))^{\frac{2}{d_1}}. \quad (5.36c)$$

The auto-calibration problem of the engine with an electrified WHR system is approached by gridding the feasible sets for u_{EGR} , u_{VTG} and P_S and minimizing the Hamiltonian (5.29). The gridding is performed by initially dividing each variable into 5

equal-value intervals. A centroid is defined which locates the minimum grid point. The search involves multiple passes, which shrinks the multidimensional grid around the optimum. The search stops if at least one of the following three conditions is satisfied: the change in the Hamiltonian is less than 10^{-5} , the grid interval is less than 10^{-4} , or the maximum of 300 iterations is reached. The method outputs the global optimum. This is verified by choosing a dense initial gridding and a loose stopping criteria.

The parameters of the IPC strategy, *i.e.*, λ_T , ΔT_1 , ΔT_2 , λ_3 , λ_4 and λ_{5ref} , are tuned using the nonlinear optimization routine *fmincon* from Matlab. The objective is to minimize the operational costs (5.27), while meeting the specified NO_x target (5.28k) over the weighted WHTC for cold-start and hot-start conditions. According to the legislation, the NO_x target emissions for the cold-start and hot-start cycle are weighted by 16% and 84%, respectively.

5.5.5 Battery bounds

During normal operation, the battery power P_S needs to be bounded in order to avoid infeasible battery power requests. There are two infeasible situations: during charging, when the battery power at the terminals is less than the generated power, *i.e.*, $P_B < P_G$; and during motoring, when the motor power is greater than the power needed to be delivered, *i.e.*, $P_M > P_d$. To avoid these infeasible regions, the requested battery power needs to be bounded as:

$$P_S \in [P_{Smin}^{dyn}, P_{Smax}^{dyn}]. \quad (5.37)$$

Using (5.9), (5.11) and (5.14) for the lower battery bound and (5.9), (5.11) and (5.15) for the upper battery bound, yields:

$$P_{Smin}^{dyn} = \max \left(P_{Smin}, \min \left(P_{Smax}, \frac{1 - \sqrt{1 + 4\beta P_G}}{2\beta} \right) \right), \quad (5.38a)$$

$$P_{Smax}^{dyn} = \min \left(P_{Smax}, \max \left(P_{Smin}, \frac{\eta_M - \sqrt{\eta_M^2 - 4\eta_M\beta(P_d^{lim} - \eta_M P_G)}}{2\eta_M\beta} \right) \right). \quad (5.38b)$$

To ensure a physically meaningful solution in (5.38b), the desired power upper is limited, *i.e.*:

$$P_d^{lim} = \max \left(0, \min \left(P_d, \frac{\eta_M}{4\beta} + \eta_M P_G \right) \right). \quad (5.39)$$

Since the regenerative braking is not considered here, Eq (5.39) implies that all the negative requested power is dissipated using the vehicle braking system.

5.5.6 Baseline strategy

For comparison, a baseline strategy [32] is proposed that mimics a state-of-the-art air management strategy for a standard Euro-VI engine without WHR system. The baseline strategy consists of two control modes:

- **M1: Thermal management mode** for rapid heat-up of the aftertreatment system ($T_{SCR} < 200^\circ\text{C}$);
- **M2: Low NO_x mode** for normal operation ($T_{SCR} \geq 250^\circ\text{C}$).

The baseline strategy relies on fixed control settings (u_{EGR}, u_{VTG}) for each engine operating point (ω_E, τ_E). For both modes, these settings are determined in an off-line optimization. The optimization is performed over a set of representative engine speed and torque operating points from a certain driving cycle, *e.g.*, the WHTC. The obtained values for the control settings (u_{EGR}, u_{VTG}) remain fixed also for other cycles.

As we want to use the same control framework for all strategies in simulations, for each control mode M1 and M2, a different constant λ_1 is used, $\lambda_{1,M1}$ and $\lambda_{1,M2}$, respectively (see Table 5.2). Since the engine calibration is performed using steady-state measurements, anticipated steady-state T_{DOC} and T_{SCR} values from the engine maps are used in the Hamiltonian to evaluate the SCR efficiency.

5.6 Simulation results

In this section, the performance of the proposed controllers is evaluated. Here, we focus on the results of the IPC strategy. All the presented cases are compared with the baseline strategy (the standard Euro-VI engine without WHR system). Simulations are performed for stationary conditions and for transient conditions from the World Harmonized Transient Cycle (WHTC) (see Fig. 5.6). The simulations for stationary conditions are done to assess the engine efficiency improvement due to a WHR system over the complete speed-torque engine operating region. The simulations for transient conditions are performed to determine the best powertrain configuration for different real-world driving conditions.

5.6.1 Stationary conditions

First, we analyze the benefit of an IPC strategy with WHR system (IPC WHR) for stationary conditions. The battery effect on fuel conversion efficiency is not studied

Table 5.1: Powertrain parameters: engine, aftertreatment, WHR system, electric system.

Symbol	Value	Measure Unit	Description
c_1	0.1163	kg^{-1}	constant defined as $c_1 = \frac{c_{p,exh}}{C_{DOC}}$
c_2	0.0512	kg^{-1}	constant defined as $c_2 = \frac{c_{p,exh}}{C_{SCR}}$
c_3	$7.692 \cdot 10^{-4}$	$\text{s} \cdot \text{kg}^{-1}$	constant defined as $c_3 = \frac{h}{C_{SCR}}$
c_4	2.0067	–	AdBlue dosage constant
π_{fl}	$1.34 \cdot 10^{-3}$	€/g	diesel price
π_a	$0.50 \cdot 10^{-3}$	€/g	AdBlue price
π_{PM}	$7.10 \cdot 10^{-2}$	€/g	DPF regeneration price
n	70	–	number of battery cells
Q	8280	A · s	battery cell capacity
R	0.01	Ω	battery cell internal resistance
U_{oc}	3.3	V	battery cell voltage
I_{max}	± 35	A	battery maximum current
P_{Smin}	–8.08	kW	minimum battery pack power
P_{Smax}	8.08	kW	maximum battery pack power
E_{Bmax}	1912	kJ	maximum battery pack energy
SOE_{min}	0.2	–	minimum battery SOE
SOE_{max}	0.8	–	maximum battery SOE
SOE_{ref}	0.5	–	reference battery SOE
K_p	$0.7 \cdot 10^{-4}$	–	proportional term for the battery
P_{Mmax}	20	kW	maximum motor power
η_M	0.95	–	motor efficiency
η_G	0.95	–	generator efficiency
ζ_{WHR}	80	s	WHR system time constant
Z_{NO_x}	$0.41/(3.6 \cdot 10^6)$	kg/Ws	NO _x emission limit (0.41 g/kWh)

here, since this is relevant for transient conditions. From Fig. 5.7a, we can see that the motor power output increases for high speed-torque engine conditions. For low speed-torque engine conditions, the motor power is limited due to the low engine heat flow rates that lead to a reduced WHR system power output.

The absolute stationary fuel conversion efficiency improvement due to a WHR system, is defined as:

$$\Delta\eta = \frac{P_d}{(P_{fl})_{IPC\ WHR}} - \frac{P_d}{(P_{fl})_{baseline}}, \quad (5.40)$$

where P_{fl} is the fuel chemical power. In Fig. 5.7b, the absolute efficiency improvement of the IPC strategy with a WHR system is shown over the complete engine map. Up

Table 5.2: Selected control parameters.

Control strategy	Control parameters					
	$\lambda_{1,M1} \cdot 10^{-3}$	$\lambda_{1,M2}$	λ_2	$\lambda_3 \cdot 10^{-3}$	$\lambda_4 \cdot 10^{-6}$	$\lambda_{5ref} \cdot 10^{-5}$
Baseline	-2.68	0	0	3.23		
Recal WHR	-1.72	0	0	2.98		
Recal battWHR	-1.84	0	0	2.95		
	ΔT_1	ΔT_2	$\lambda_T \cdot 10^{-3}$	$\lambda_3 \cdot 10^{-3}$	$\lambda_4 \cdot 10^{-6}$	$\lambda_{5ref} \cdot 10^{-5}$
IEM	116	184	-2.05	2.71	-	-
IPC WHR	106	190	-2.36	2.62	-2.97	-
IPC battWHR	100	192	-1.57	2.49	-2.86	-5.88

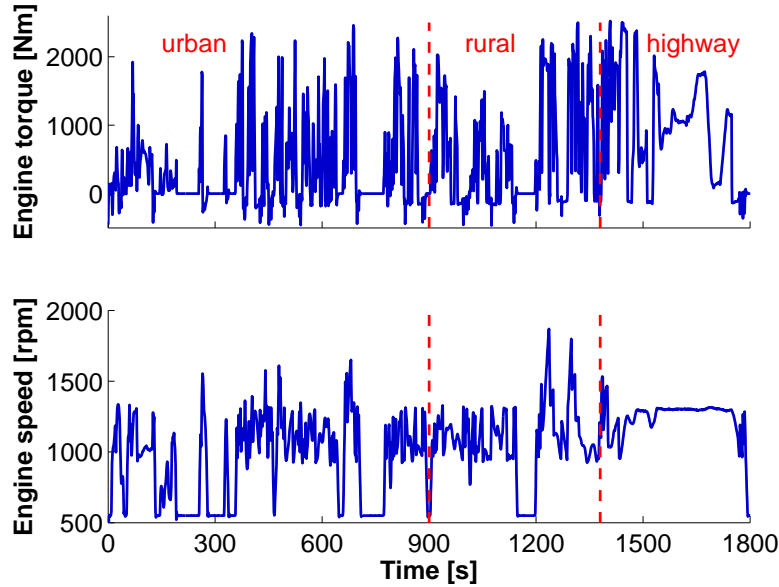


Figure 5.6: Engine torque and speed requested from the World Harmonized Transient Cycle. Three different parts can be distinguished: urban, rural and highway driving.

to 4% fuel conversion efficiency improvement is obtained by optimizing the complete powertrain.

5.6.2 World Harmonized Transient Cycle

Second, the proposed control strategies are tested over the WHTC cycle. This is a highly dynamical cycle representative for real-world driving conditions: urban (0-900 s), rural (901-1380 s) and highway (1381-1800 s), as illustrated in Fig. 5.6. Since we focus

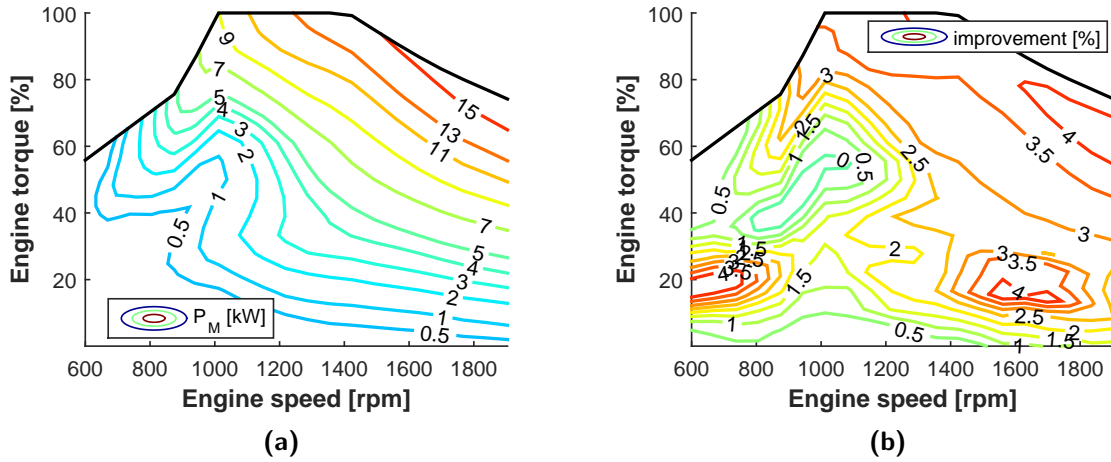


Figure 5.7: (a) The net electric motor power output P_M . (b) Absolute fuel conversion efficiency improvement for the IPC strategy with an electrified WHR system as compared to the baseline strategy.

on Euro-VI legislation, results have to be generated for cold-start as well as hot-start conditions. In case of cold-start (hot-start) cycle, the initial SCR catalyst temperature and WHR system working fluid temperature are both set to 20°C (200°C) whereas the initial WHR pressure is set to 1 bar (30 bar). The engine heat-up model is not available in this study.

By assuming a linear relationship with slope one between the CO₂ emissions and fuel consumption, the NO_x-CO₂ trade-off is shown in Fig. 5.8 for the studied six cases. All results are compared with the baseline strategy. The Integrated Emission Management (IEM) strategy gives a 1.5% CO₂ emissions reduction. By only adding a WHR system to the existing engine, the CO₂ emissions are reduced by 1.7% compared to the baseline, while additional margin is created in the NO_x emissions. Due the NO_x-CO₂ trade-off, the NO_x margin can be exploited to reduce the CO₂ further by recalibrating the baseline strategy (*i.e.*, re-parameterizing λ_1 and λ_3). This results in a total of 2% CO₂ emissions reduction for the recalibrated baseline with WHR system. By using a WHR system equipped with a battery (battWHR), a 2.25% CO₂ emissions reduction is achieved as compared to the baseline. This result is obtained using a simple rule-based battery management. With an optimal battery management, the reduction in CO₂ emissions can go up to 2.5%. This is demonstrated by comparing the IPC WHR system with IPC battWHR system that give a 3% and a 3.5% CO₂ emissions reduction, respectively. All results are shown to satisfy the Euro-VI NO_x emissions standard.

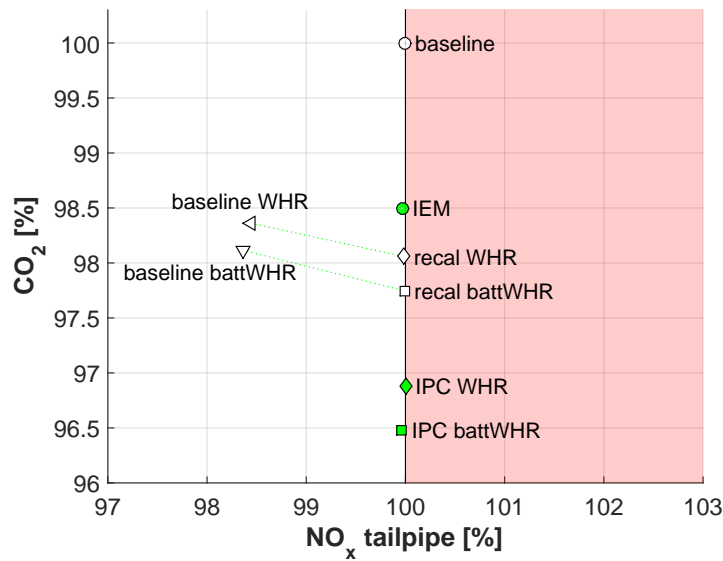


Figure 5.8: $\text{CO}_2\text{-NO}_{x,tp}$ trade-off for weighted WHTC, *i.e.*, $\text{NO}_{x,tp} = 0.16 \cdot \text{NO}_{x,tp}^{\text{cold}} + 0.84 \cdot \text{NO}_{x,tp}^{\text{hot}}$. The shaded red area expresses the Euro-VI NO_x emissions constraint violation.

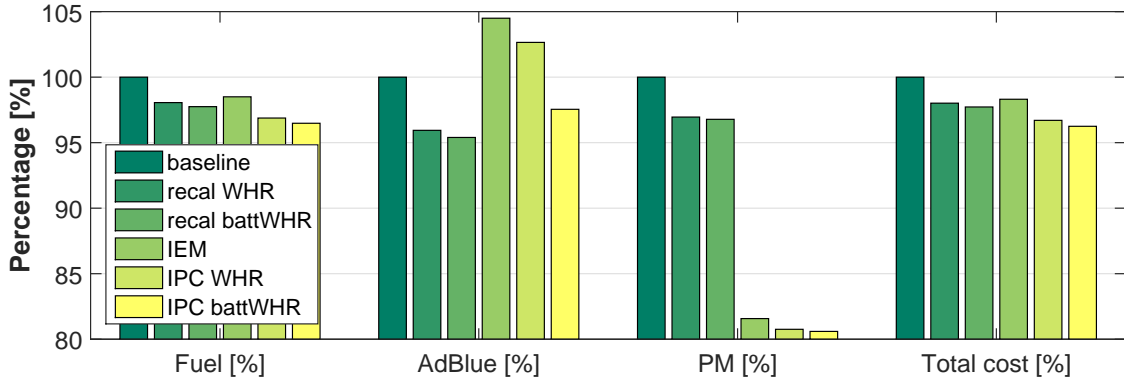


Figure 5.9: The total fuel and AdBlue consumption, PM reduction and operational cost for WHTC cold-stat and hot-start.

Fig. 5.9 shows the fuel consumption, AdBlue dosage, PM and total operational cost for each of the studied case. Due to EGR-SCR balancing, the AdBlue dosage is increased for the optimized strategies IEM, IPC WHR and IPC battWHR as compared to the baseline, recal WHR and recal battWHR, respectively. In contrast, PM emissions related cost is significantly reduced for the optimized strategies. For the IPC battWHR, the AdBlue dosage is reduced by 2.5%, the PM is lowered by 19%, and the total operational cost is decreased by 4% as compared to the baseline strategy.

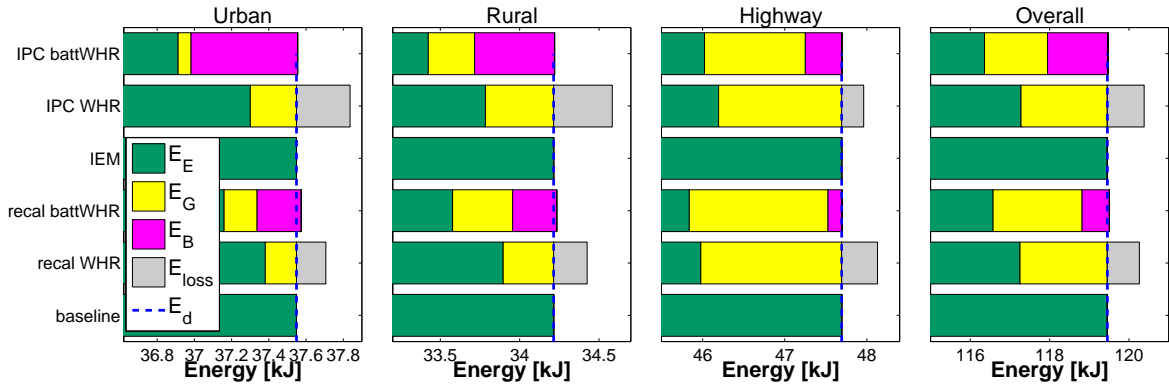


Figure 5.10: Traction energy flows for different driving conditions from the hot-start WHTC.

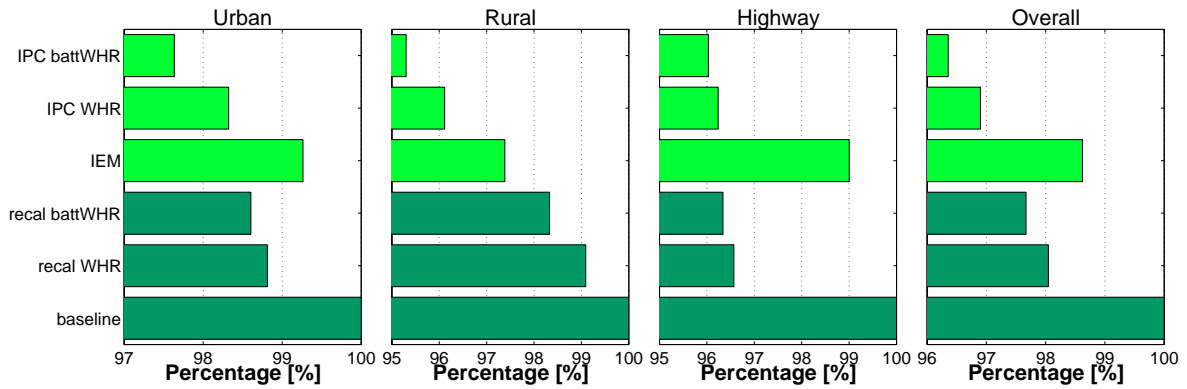


Figure 5.11: The fuel consumption for different driving condition from the hot-start WHTC.

Next, Fig. 5.10 illustrates the traction energy flows for the proposed control strategies. The traction energy flow is computed as $E = \int_0^{t_f} P_+(t)dt$, where P_+ is the positive instantaneous power. For the baseline and IEM strategy the whole desired energy E_d is provided by the engine. In case of the recal WHR and IPC WHR, E_{loss} indicates the lost traction energy. This energy is the WHR system energy that cannot be delivered to the powertrain, *e.g.*, during vehicle braking. Since there is no storage device on a recal WHR and IPC WHR configurations, E_{loss} is discarded by activating the expander bypass valve. For the recal battWHR and IPC battWHR configurations, it should be noted that energy storage is beneficial during the urban and rural driving conditions, while during the highway driving the battery usage is attenuated. This clearly indicates that an electrified WHR system equipped with a battery is suited for city type of driving conditions. During the highway driving, typical for long-haul applications, the battery usage is minor. From a cost-benefit point of view, we consider that a battery is not

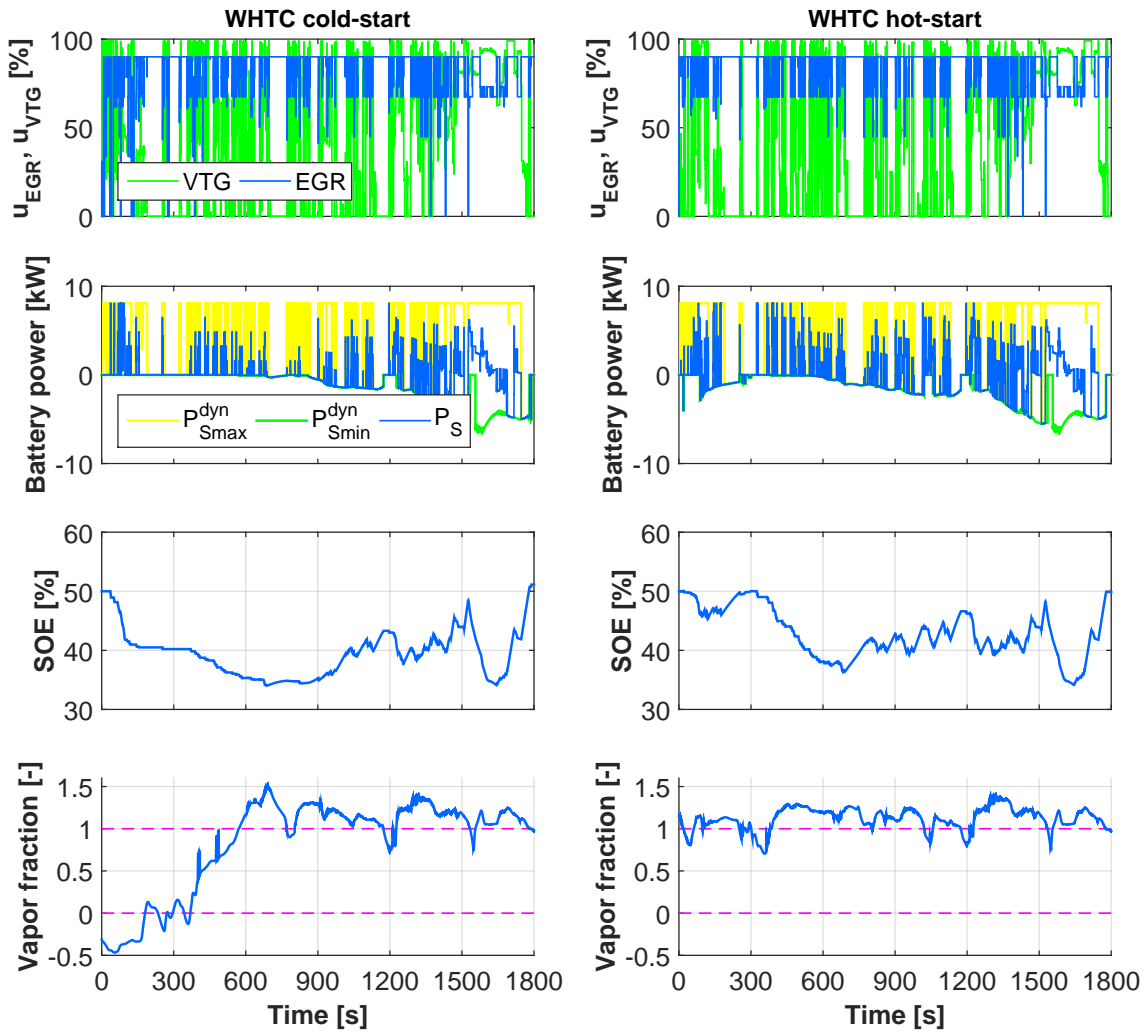


Figure 5.12: Computed control inputs, battery SOE and WHR system vapor production for WHTC cold-start and hot-start conditions. According to the convention, $P_S > 0$ and $P_S < 0$ indicates that the battery is discharging and charging, respectively.

suitable for WHR long-haul applications. However, note that regenerative braking and hilly terrain driving has not been studied, which may increase the battery usage also for highway driving conditions.

The total fuel consumption for each of the driving condition is illustrated in Fig. 5.11. During the urban and rural driving, typically dominated by highly transient engine behavior, the improvement EGR appears to be due to the proposed optimized control strategy in combination with WHR system. However, during the highway driving, the used control method has smaller effect to fuel improvement as compared to the cases with

WHR system. All the studied cases with WHR system show fuel economy improvement of more than 3.5% during highway driving. The best result is obtained for the IPC battWHR configuration, which shows 4% fuel economy improvement during highway driving.

Finally, Fig. 5.12 shows the computed control inputs u_{EGR} , u_{VTG} , P_S and the battery state of energy (SOE) for the IPC strategy with WHR system and battery. As seen also from Fig. 5.10, the battery power usage is more pronounced for urban and rural driving, corresponding to the beginning of the cycle. At the end of the cycle the battery SOE reaches the initial value. As such, the charge sustaining constraint is satisfied for both cold-start and hot start conditions. The control actuation appears to be highly transient. This behavior is due to the highly transient nature of the test cycle.

The bottom graphs of Fig. 5.12 show the vapor production of the WHR system. From the cold-start cycle, it can be seen that up to 600 s are necessary to heat-up the WHR system and produce power. The regulation problem of maintaining vapor is realized by the low-level WHR system control.

5.7 Conclusions

Optimal control of Euro-VI diesel engines with Waste Heat Recovery system is challenging due to the large number of subsystems, strong interactions and emission requirements set by legislation. In this chapter, an optimized supervisory control strategy is presented, that minimizes the total operational costs while complying with the tailpipe NO_x emissions constraint. Based on the Pontryagin's Minimum Principle, a real-time implementable strategy is proposed. Different powertrain configurations are analyzed, with focus on electrified WHR system. This analysis is done for both stationary conditions and dynamic conditions from the World Harmonized Transient Cycle. From the simulation results, it is concluded that an electrified WHR system is most suitable for urban and rural driving conditions. For highway driving conditions on flat terrains, energy storage usage is minor. Thus, from a cost-benefit point of view, we consider that a battery is not suited for long-haul applications. For the complete WHTC, it is shown that the optimal IPC strategy with an electrified WHR system and battery outperforms the current baseline strategy. Within the tailpipe NO_x limit, the proposed strategy shows an additional 3.5% CO_2 emission reduction while the AdBlue dosage is attenuated by 2.5% and particulate matter is reduced by 19%.

Discussion, conclusions and recommendations

Abstract This thesis will close with some discussions regarding the main contributions of this research and with some directions that require careful attention. Furthermore, the conclusions will be presented and recommendations for future research will be drawn.

6.1 Discussion

Recovering heat energy from exhaust gas is a promising technology to improve fuel economy. The objective of this research is the development of an integrated energy and emission management strategy, which on-line optimizes the performance of a vehicle with a WHR system. To this end, a model-based control strategy is adopted.

6.1.1 WHR system modeling

For understanding heat recovery and for designing control algorithms, dynamic models in a physics-based mathematical framework are presented in this thesis. The modeling of these type of systems is very challenging mainly due to the highly non-linear boiling phenomena. Despite the large number of studies on boiling heat transfer, the prediction of heat transfer coefficients is still based on empirical or semi-empirical relations. The reason is the lack of a coherent description of the complex interactions between various heat and mass transport processes involved in boiling heat transfer. This usually brings complications and creates confusion in selecting the most appropriate mathematical framework for boiling.

For waste heat recovery systems based on the Rankine Cycle, the evaporator and expander are the most difficult to model. For control, capturing the phase transitions within the evaporator is crucial. The evaporator is usually modeled using a moving boundary (MB) approach, a finite volume (FV) or finite difference (FD) formulation. In choosing which method to apply, there is a trade-off between computation intensity and accuracy. Furthermore, for a good accuracy of the model, the heat transfer coefficient needs to be appropriately chosen according to the evaporator geometry, construction material and type of working fluids.

The expander is modeled as a stationary component, since the expander power changes much faster than the relevant thermal phenomena within the evaporators. In this model, the effect of power change in the presence of droplets at the expander inlet is not considered. Thus, the expander is bypassed for two-phase inlet conditions. However, it is known that some expander technologies, such as piston or screw expanders, are more robust for inlet droplets than for *e.g.*, turbine expanders. Modeling the two-phase effect on expander power will allow studying power generation in the presence of inlet droplets, a phenomena which is quite often encountered in automotive applications. This is due to highly dynamic engine conditions in real-world situations.

The complete WHR system model was identified and validated on dynamometer measurements from a Euro-VI heavy-duty diesel engine. For validation, knowledge of the sensors error and uncertainty is essential. For instance, a systematic error can occur when measuring the exhaust gas temperature due to the radiation from the exhaust pipe on the thermocouple, and due to non-uniform temperature distribution over the pipe cross section. To increase the measurement quality, it is important to appropriately choose the sensor positions. Moreover, by using multiple temperature sensors in one location the measurement errors are reduced.

6.1.2 Control

Using the developed model, a switching model predictive control (MPC) strategy is developed to guarantee safe system operation. Safety is associated with the avoidance of droplets flow into the expander. For WHR systems with two evaporators, the mixed working fluid before the expander is required to be in vapor state. To realize this, the proposed control strategy is designed to guarantee vapor at the outlet of each evaporator. One can exploit the complete mixing region to improve disturbance rejection, by considering the nonlinear mixing effects.

The developed WHR system control strategy, together with the control strategies for

fueling and AdBlue dosage represent the low-level engine control system. To minimize operational costs within the emission constraints, an integrated powertrain control (IPC) strategy is developed on top of the low-level control strategies. The IPC control method is applied to different powertrain configurations to assess the improvement in fuel economy and cost reduction due to the WHR system. For urban, rural and highway driving conditions, the effect of WHR system energy storage is studied.

Based on the obtained results in terms of fuel economy, a business case example is formulated. The WHR system return of investment time is less than two years. This demonstrates the feasibility of WHR systems for heavy-duty applications.

6.2 Conclusions

This thesis contributes to the development of an integrated powertrain control strategy for a diesel engine with WHR system. The goal is to optimize the complete powertrain by minimizing the fuel and AdBlue consumption, while satisfying the tailpipe emission constraints. To this end, a model-based control design approach is used.

Dynamic WHR system modeling. First, a heat exchanger model is developed based on state-of-the-art empirical or semi-empirical methods for flow boiling. The modeling of a modular heat exchanger, characterized by multiple phase transitions in a single pipe flow, is not straight forward. In Chapter 2 it has been presented a heat exchanger modeling approach that combines the FD method with a moving boundary approach. Thus, the dynamics of multiple phase transition caused by the modular heat exchanger design are captured. The model was validated on data from a state-of-the-art Euro-VI heavy-duty diesel engine. The validation was performed on a highly dynamic cycle typical for real-world driving conditions. From the simulation results, the model predicts the working fluid vapor fraction and exhaust gas temperature dynamics with average error below 4%, adequate accuracy for control-oriented purposes.

Second, a complete WHR system model with two parallel evaporators is developed and validated. Based on the Organic Rankine Cycle (ORC) for low-grade heat sources, this thesis considers pure ethanol as working fluid. The ethanol thermodynamic properties were fitted off-line. The resulting expressions were used on-line, to reduce the memory usage of the look-up table methods. The proposed WHR system model combines first principle modeling with stationary component models. The resulting average model prediction errors over a dynamic cycle are: 2% for the heat flow rate, 3% for the mass flow rate, 2% for the WHR system pressure and 4% for the working fluid temperature.

These accuracies are typical for automotive WHR systems. Thus, the model is suitable for analysis, prediction and control design purposes.

Low-level control design. For the low-level WHR system control design, a switching linear model predictive control (MPC) strategy was designed to guarantee safe operation while maximizing the WHR system power output. The performance of the proposed control strategy was demonstrated on a highly dynamic World Harmonized Transient Cycle. Compared to a classical PI controller, simulation results showed up to 15% more vapor time and recovered thermal energy for the proposed linear MPC strategy. Using a nonlinear MPC, the control performance can be improved further by up to 10% as compared to the linear MPC. However, this requires more computational power, while it comes at the cost of developing an accurate nonlinear model. As a result, the switching linear MPC strategy appears favorable for real-time implementation. A direction to improve the control performance is to increase the number of switching regions within the switching linear MPC strategy. Another alternative is to use feedback linearization techniques from [82]. This approach retains all the properties of the classical linear MPC strategy.

Integrated control approach. This addresses the optimal control design of a complete truck powertrain with an electrified WHR system. The considered truck powertrain consists of a heavy-duty diesel engine, an aftertreatment system and an electrified WHR system. The WHR system is augmented with a battery to allow electrical energy storage. Considering the increasing powertrain complexity and the up-coming emission legislation, for further CO₂ emission reduction, an integrated powertrain control (IPC) approach is essential. In this thesis, an optimized control strategy is presented, that minimizes the total operational costs (fuel and AdBlue dosing) while complying with the tailpipe NO_x emissions constraint. Compared to the traditional engine calibration, the proposed control strategy optimizes the engine settings and requested battery power on-line (auto-calibration). Different powertrain configurations are analyzed, for both stationary conditions and real-world driving conditions from a World Harmonized Transient Cycle. From the simulation results, it is seen that for urban and rural driving conditions, the generated power is limited due to the highly transient engine heat flow rate. Thus, the motor is driven almost entirely by the battery power. For highway driving conditions, the opposite situation occurs. The battery energy usage is moderate, while the motor power is mostly driven by the generator power. From a cost-benefit point of view, an electrified WHR system without battery is the most suitable for highway driving conditions, with 3.8% CO₂ emission reduction as compared to a baseline engine. For a combination of urban, rural

and highway driving, an electrified WHR system with battery appears to be favorable, realizing 3.5% CO₂ emission reduction within the tailpipe NO_x limit.

System architecture. Initially, the WHR system was mechanically coupled to the engine crankshaft. However, this leads to some limitations. First, the system pressure cannot be manipulated, which can impact safety, associated with vapor production. Second, since the expander speed is dictated by the engine, the WHR system does not operate at the optimum speed, reducing the power output. In Chapter 4, a WHR system with the expander and pumps decoupled from the engine is considered. For real-world driving conditions, we have shown that the net power output at the expander shaft increases by up to 29% for a decoupled WHR system configuration.

Furthermore, the decoupled WHR system was electrified using a generator, a motor and a battery. From simulations, it follows that an electrified WHR system equipped with a battery is the most suitable configuration for urban and rural driving, dominated by a highly transient behavior. For highway driving conditions, the fuel consumption reduction due to the battery usage is insignificant. Thus, an electrified WHR system without a battery is the most suited architecture for highway driving.

Business case. To compute the return of investment for a truck with a WHR system, we consider a simple business case example. First, assume a traditional 42 tonne truck with an average fuel consumption of 35 l/100 km, that covers 150 000 km per year. Second, consider that the same truck is equipped with an electrified WHR system that provides in average 3.5% fuel consumption reduction. The additional cost associated with the WHR system, are estimated to be around 4 000 €, excluding the battery which is already present in a hybrid electric vehicle. With a diesel price of 1.34 €/l, the traditional truck fuel cost per year is 70 350 €. On the other hand, for a truck with WHR system the fuel cost reduces to 67 887 €. The cost saving per year due to the WHR system is 2 463 €. Hence, the return on investment for a truck with WHR system is approximately 1.6 years. Note that this business case example does not consider maintenance costs for the truck nor for the WHR system.

6.3 Recommendations for future research

The methods and developments presented in this thesis open directions for further exploration. These directions are in the area of modeling, control and experimental validation. In what follows, the future research directions are presented in more detail.

Extending the WHR system model. A high-fidelity WHR system model has been developed and validated in this thesis. However, since the focus was on low-level control and assessment of the WHR system potential, the cooling in the condenser has not been studied. A simplified condenser model [42] has been used to obtain a rough estimation of the cooling demand. The condenser model can therefore be extended using a similar mathematical framework as presented for the evaporator. Special attention needs to be given in the area of capturing the condensation phenomena by appropriately selecting the heat transfer coefficients. Using the condenser model, the performance of a closed Rankine Cycle and impact on vehicle cooling system can be investigated.

System design and sizing. The power generation from automotive waste heat can be improved by a better system design, *e.g.*, finding the best evaporator geometry and choosing a suitable expander technology. Furthermore, to maximize the efficiency and power output while minimizing the losses, system weight, cost and fuel consumption, optimal component sizing is an important future step towards series production of WHR systems. Critical components in a conventional WHR system configuration are: the pumps, evaporators, condenser and expander. Additionally, in case of an electrified WHR system, the sizing of the battery, motor and generator is of interest for optimization.

Experimental testing of the low-level control strategy. The performance of the proposed Model Predictive Control strategy has been demonstrated in simulations. Next step is to validate the results on an experimental setup. First, the MPC control strategy uses the vapor fraction information for control. In a real-world application, these sensors are very expensive and usually require a lot of hardware equipment. Thus, for the two-phase region, a vapor fraction estimator needs to be developed. Second, the MPC algorithm has to be implemented in a real-time. The current MPC toolkits, such as the *Model Predictive Control Toolbox* from Matlab or the *Multi-Parametric Toolbox* [83], produce ready-to-run C/C++ code. Thus, it is possible to quickly implement MPC algorithms on computers and rapid control prototyping (RCP) equipments.

Extending the supervisory control strategy. In this thesis an integrated control strategy has been proposed for a truck with aftertreatment and electrified WHR system. Firstly, the current approach does not study the effect of the WHR system on the vehicle cooling capacity. Therefore, the control strategy can be extended to account for the cooling demand of the vehicle. Furthermore, optimality and robustness of the control method has to be verified in the presence of climate change and for different driving cycles. Secondly, the proposed approach solves a nonlinear constrained

optimization problem. Often, these problems require significant computational power to be solved. An effective way to reduce computational complexity, with guarantees on global solution, is to formulate the problem as a convex optimization problem. However, further investigations need to be carried out to verify the convexity of the problem or possibilities for problem relaxation.

Performing vehicle experimental validation. The complete proposed control scheme needs to be experimentally tested and validated. The implementation of the high-level control strategy is recommended, for assessing fuel economy and vehicle drivability. Moreover, the robustness of the control method needs to be verified for a different driving cycles and in the presence of climate change.

Fluid properties

A.1 Working fluid properties

The normalized saturation temperature as a function of normalized pressure is shown in Fig. A.1. The saturation temperature is the temperature for a corresponding pressure at which a liquid boils into its vapor phase. A mathematical relation to describe the saturation temperature is given in [84]:

$$T_{sat}^* = \frac{1}{T_c} \left(\frac{b_s}{a_s - (\log_{10} p_f - 5)} - c_s \right), \quad (\text{A.1})$$

where p_f is the working fluid pressure. For ethanol the constants a_s , b_s and c_s are taken from [84].

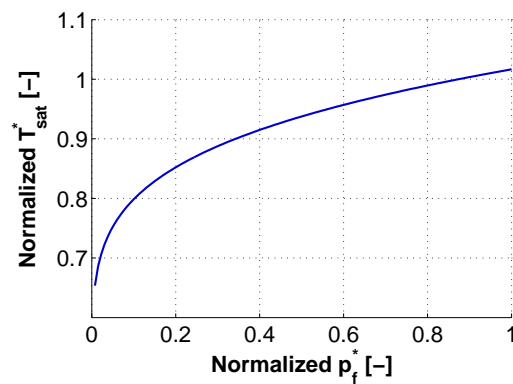


Figure A.1: Normalized working fluid saturation temperature as a function of pressure.

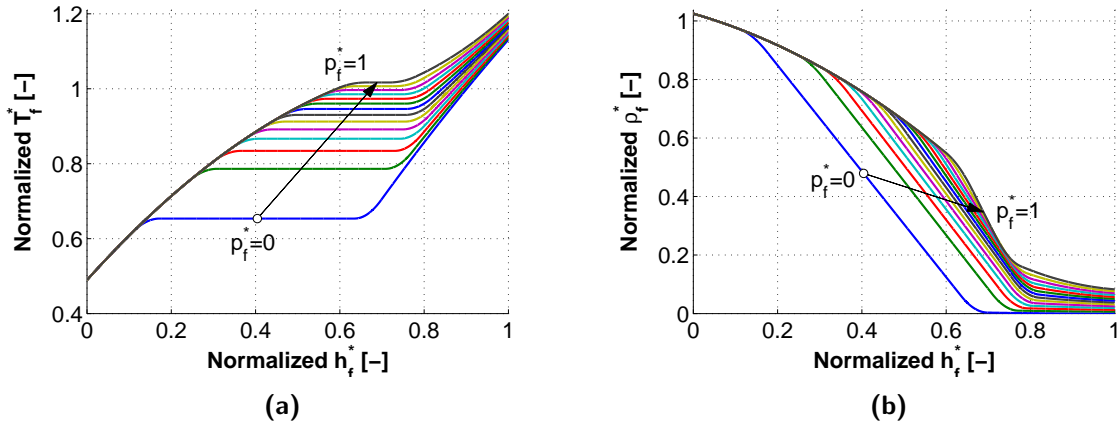


Figure A.2: (a) Normalized working fluid temperature as a function of specific enthalpy and pressure. (b) Normalized working fluid density as a function of specific enthalpy and pressure.

In Fig. A.2a the normalized temperature-enthalpy characteristic of the working fluid for different values of the pressure is presented. The working fluid temperature can be approximated as follows:

$$T_f^* = \begin{cases} a_l h_f^{*2} + b_l h_f^* + c_l & \text{if } h_f^* \leq h_{l_1}^* \\ a_{sl} h_f^{*3} + b_{sl} h_f^{*2} + c_{sl} h_{*f} + d_{sl} & \text{if } h_{l_1}^* < h_f^* < h_{l_2}^* \\ T_{sat}^* & \text{if } h_{l_2}^* \leq h_f^* \leq h_{v_1}^* \\ a_{sv} h_f^{*3} + b_{sv} h_f^{*2} + c_{sv} h_{*f} + d_{sv} & \text{if } h_{v_1}^* < h_f^* < h_{v_2}^* \\ a_v h_f^{*2} + b_v h_f^* + c_v & \text{if } h_f^* \geq h_{v_2}^* \end{cases}, \quad (\text{A.2})$$

where a_l , b_l , c_l are constants used for the temperature-enthalpy characteristic on the liquid region. In the two-phase region the normalized working fluid temperature is constant and equal to the normalized saturation temperature T_{sat}^* . The vapor region is approximated using pressure dependent coefficients:

$$a_v = a_{v_1} p_f^* + a_{v_0}, \quad b_v = b_{v_1} p_f^* + b_{v_0}, \quad c_v = c_{v_1} p_f^* + c_{v_0}. \quad (\text{A.3})$$

Let us define the normalized saturated liquid enthalpy $h_{l_1}^*$ and vapor enthalpy $h_{v_1}^*$ as a function of T_{sat}^* :

$$h_{l_1}^* = \frac{-b_l + \sqrt{b_l^2 - 4a_l(c_l - T_{sat}^*)}}{2a_l}, \quad (\text{A.4a})$$

$$h_{v_1}^* = \frac{-b_v + \sqrt{b_v^2 - 4a_v(c_v - T_{sat}^*)}}{2a_v}. \quad (\text{A.4b})$$

In (A.2), two cubic functions are introduced to impose a smooth transition from liquid to two-phase and from two-phase to vapor. The coefficients of these cubic functions are obtained by solving a set of four linear equations at a specified normalized pressure p_f^* . The four linear equations follow by enforcing continuity and imposing the same slope at each of the chosen thresholds $h_{l_1}^*$ and $h_{l_2}^*$. Around the liquid and vapor saturation point, a similar procedure is employed.

The thresholds used in (A.2) are defined as:

$$\begin{aligned} h_{l_1}^* &= h_l^* - \Delta h^*, & h_{l_2}^* &= h_l^* + \Delta h^*, \\ h_{v_1}^* &= h_v^* - \Delta h^*, & h_{v_2}^* &= h_v^* + \Delta h^*, \end{aligned} \quad (\text{A.5})$$

where Δh^* is a positive value, upper limited by the critical pressure such that $h_{l_2}^*$ does not become larger than $h_{v_1}^*$.

In Fig. A.2b the normalized working fluid density as a function of enthalpy and pressure is illustrated. The expression which describes the density is

$$\rho_f^* = \begin{cases} a_{\rho_l} h_f^{*2} + b_{\rho_l} h_f^* + c_{\rho_l} & \text{if } h_f^* \leq h_{l_1}^* \\ a_{\rho_{sl}} h_f^{*3} + b_{\rho_{sl}} h_f^{*2} + c_{\rho_{sl}} h_f^* + d_{\rho_{sl}} & \text{if } h_{l_1}^* < h_f^* < h_{l_2}^* \\ \frac{\rho_v^* - \rho_l^*}{h_v^* - h_l^*} h_f^* + \frac{h_v^* \rho_l^* - h_l^* \rho_v^*}{h_v^* - h_l^*} & \text{if } h_{l_2}^* \leq h_f^* \leq h_{v_1}^* \\ a_{\rho_{sv}} h_f^{*3} + b_{\rho_{sv}} h_f^{*2} + c_{\rho_{sv}} h_f^* + d_{\rho_{sv}} & \text{if } h_{v_1}^* < h_f^* < h_{v_2}^* \\ a_{\rho_v} h_f^{*2} + b_{\rho_v} h_f^* + c_{\rho_v} & \text{if } h_f^* \geq h_{v_2}^* \end{cases} \quad (\text{A.6})$$

where a_{ρ_l} , b_{ρ_l} , c_{ρ_l} are constants used to approximate the density-enthalpy characteristic for the liquid region. In the vapor region the polynomial coefficients are quadratic expressions of the form

$$a_{\rho_v} = a_{\rho_{v2}} p_f^{*2} + a_{\rho_{v1}} p_f^* + a_{\rho_{v0}}, \quad (\text{A.7a})$$

$$b_{\rho_v} = b_{\rho_{v2}} p_f^{*2} + b_{\rho_{v1}} p_f^* + b_{\rho_{v0}}, \quad (\text{A.7b})$$

$$c_{\rho_v} = c_{\rho_{v2}} p_f^{*2} + c_{\rho_{v1}} p_f^* + c_{\rho_{v0}}, \quad (\text{A.7c})$$

since linear expressions are inaccurate approximations of the real characteristic given in Fig. A.2b. The saturated liquid and vapor density are given by

$$\rho_l^* = a_{\rho_l} h_l^{*2} + b_{\rho_l} h_l^* + c_{\rho_l}, \quad (\text{A.8a})$$

$$\rho_v^* = a_{\rho_v} h_v^{*2} + b_{\rho_v} h_v^* + c_{\rho_v}. \quad (\text{A.8b})$$

As for the temperature-enthalpy characteristic also for the density-enthalpy characteristic a set of four linear equations are solved to find the cubic function coefficients. The reason for smoothing the working fluid properties is to avoid discontinuities in the working fluid enthalpy derivative around the liquid and vapor saturation curves, which can cause the phenomenon of chattering. Due to this phenomenon, the computed variables can exceed acceptable boundaries, causing simulation failures.

Battery management

B.1 Rule-based battery management

The rule-based battery management presented in this section is used for the baseline strategy with WHR system equipped with a battery. We distinguish three cases for the battery power P_S : case 1 is when requested torque τ_{req} is greater than the maximum motor torque τ_{Mmax} ; case 2 is when requested torque τ_{req} is positive but less than the maximum motor torque τ_{Mmax} ; case 3 is when requested torque τ_{req} is negative. These three cases are mathematically presented as what follows.

Let us define the maximum motor torque τ_{Mmax} at the current time instant as:

$$\tau_{Mmax} = \frac{P_{Mmax}}{\omega_E}, \quad (\text{B.1})$$

then the battery management cases are:

Case 1: $\tau_{req} \geq \tau_{Mmax}$

$$P_S = P_{Smax} \quad (\text{B.2})$$

Case 2: $0 < \tau_{req} < \tau_{Mmax}$

if $\tau_{req}\omega_E \geq \eta_M P_G$

$$P_S = \min \left(P_{Smax}, \frac{1 + \sqrt{1 - 4\beta C}}{2\beta} \right) \quad (\text{B.3})$$

if $\tau_{req}\omega_E < \eta_M P_G$

$$P_S = \max \left(P_{Smin}, \frac{1 - \sqrt{1 - 4\beta C}}{2\beta} \right) \quad (\text{B.4})$$

where

$$C = \frac{1}{\eta_M} \tau_{req} \omega_E - P_G \quad (\text{B.5})$$

Case 3: $\tau_{req} \leq 0$

$$P_S = \max \left(P_{Smin}, \frac{1 - \sqrt{1 + 4\beta P_G}}{2\beta} \right) \quad (\text{B.6})$$

Note that this rule-based battery management does not guarantee that the requested torque is exactly followed for the situations when the battery power is at the minimum or the maximum limit. In these situations, how well the drive cycle is followed depends on the engine torque controller.

Bibliography

- [1] BP. BP Statistical Review of World Energy. Technical report, June 2014.
- [2] ACEA. Commercial vehicles and CO₂. Technical report, 2011.
- [3] U. Zink. MD/HD CO₂ Reduction by Hybridization & WHR. Technical report, Corning Incorporated, 2011.
- [4] D.T. Hountalas, C.O. Katsanos, D.A. Kouremenos, and E.D. Rogdakis. Study of available exhaust gas heat recovery technologies for HD diesel engine applications. *International Journal of Alternative Propulsion*, 1(2):228–249, 2007.
- [5] W.M.S.R. Weerasinghe, R.K. Stobart, and S.M. Hounsham. Thermal efficiency improvement in high output diesel engines a comparison of Rankine cycle with turbo-compounding. *Journal of Applied Thermal Engineering*, 30(14-15):2253–2256, 2010.
- [6] G. Xiaolong, Y. Suwen, X. Heng, and O. Qiang. A dynamic model for thermoelectric generator applied in waste heat recovery. *Energy*, 52:201–209, 2013.
- [7] M. Badami and M. Mura. Preliminary design and controlling strategies of a small-scale wood waste Rankine Cycle (RC) with reciprocating steam engine (SE). *Energy*, 34(9):1315–1324, 2009.
- [8] F. Kupper. Integrated Powertrain Control for an Euro-VI heavy-duty Diesel engine with Waste Heat Recovery system. Technical report, *Master's Thesis*, Eindhoven University of Technology, 2012.
- [9] D. Jung, S. Park, and K. Min. Selection of appropriate working fluids for Rankine cycles used for recovery of heat from exhaust gases of ICE in heavy-duty series hybrid electric vehicles. *Applied Thermal Engineering*, 81:338–345, 2015.

- [10] T.A. Horst, W. Tegethoff, P. Eilts, and J. Koehler. Prediction of dynamic Rankine Cycle waste heat recovery performance and fuel saving potential in passenger car applications considering interactions with vehicles energy management. *Energy Conversion and Management*, 78:438–451, 2014.
- [11] M. Allain, D. Atherton, I. Gruden, S. Singh, and K. Sissen. Daimler’s Super Truck Program; 50% Brake Thermal Efficiency. Technical report, Directions in Engine-Efficiency and Emissions Research (DEER) Conference, 2012.
- [12] W. Eckerle. Cummins: High Efficiency HD Engine. Technical report, SAE 2014 High Efficiency IC Engine Symposium, 2014.
- [13] D. Luong and T.C. Tsao. Linear Quadratic Integral Control of an Organic Rankine Cycle for Waste Heat Recovery in Heavy-Duty Diesel Powertrain. In *American Control Conference*, pages 3147–3152, Portland, USA, 2014.
- [14] D. Wei, X. Lu, Z. Lu, and J. Gu. Dynamic modeling and simulation of an Organic Rankine Cycle (ORC) system for waste heat recovery. *Journal of Applied Thermal Engineering*, 28(10):1216–1224, 2008.
- [15] K. Craig. Mechatronic Modeling Reins in HVAC Power Consumption. Technical report, Marquette University, 2011.
- [16] M. Willatzen, N.B.O.L. Pettit, and L. Ploug-Sørensen. A general dynamic simulation model for evaporators and condensers in refrigeration. Part I-II. *International Journal of Refrigeration*, 21(5):398–414, 1998.
- [17] T. McKinley and A. Alleyne. An advanced nonlinear switched heat exchanger model for vapor compression cycles using the moving-boundary method. *International Journal of Refrigeration*, 31(7):1253–1264, 2008.
- [18] R. Shah, A. Alleyne, C.W. Bullard, B. P. Rasmussen, and P.S. Hrnjak. *Dynamic Modeling And Control of Single and Multi-Evaporator Subcritical Vapor Compression Systems*. University of Illinois, 2003.
- [19] J.W. MacArthur and E.W. Grald. Unsteady compressible two-phase flow model for predicting cyclic heat pump performance and a comparison with experimental data. *International Journal of Refrigeration*, 12:29–41, 1989.
- [20] J. M. Jensen. *Dynamic Modeling of Thermo-Fluid Systems, Ph.D. Thesis*. Technical University of Denmark, 2003.

- [21] S. Quoilin, R. Aumann, A. Grill, A. Schuster, V. Lemort, and H. Spliethoff. Dynamic modeling and optimal control strategy of waste heat recovery Organic Rankine Cycles. *Journal of Applied Energy*, 88(6):2183–2190, 2011.
- [22] G.D. Mandrusiak and V.P. Carey. A finite difference computational model of annular film-flow boiling and two-phase flow in vertical channels with offset strip fins. *International Journal of Multiphase Flow*, 16(6):1071–1096, 1990.
- [23] V. Lo Brano, G. Ciulla, A. Piacentino, and F. Cardona. Finite difference thermal model of a latent heat storage system coupled with a photovoltaic device: Description and experimental validation. *Journal of Renewable Energy*, 68:181–193, 2014.
- [24] P. Colonna and H. van Putten. Dynamic modeling of steam power cycles. Part I - Modeling paradigm and validation. *Applied Thermal Engineering*, 27(2-3):467–480, 2007.
- [25] H. van Putten and P. Colonna. Dynamic modeling of steam power cycles. Part II - Simulation of a small simple Rankine cycle system. *Applied Thermal Engineering*, 27(14-15):2566–2582, 2007.
- [26] S. Quoilin. *Sustainable Energy Conversion Through the Use of Organic Rankine Cycles for Waste Heat Recovery and Solar Applications*, Ph.D. Thesis. University of Liege, 2011.
- [27] P. Tona, J. Peralez, and A. Sciarretta. Supervision and control prototyping for an engine exhaust gas heat recovery system based on a steam Rankine cycle. In *The 2012 IEEE/ASME International Conference on Advanced Intelligent Mechatronics*, pages 695–701, Kaohsiung, Taiwan, 2012.
- [28] T.A. Horst, H.S. Rottengruber, M. Seifert, and J. Ringler. Dynamic heat exchanger model for performance prediction and control system design of automotive waste heat recovery systems. *Journal of Applied Energy*, 105:293–303, 2013.
- [29] T. Endo, S. Kawajiri, Y. Kojima, K. Takahashi, T. Baba, S. Ibaraki, T. Takahashi, and M. Shinohara. Study on Maximizing Exergy in Automotive Engines. In *SAE International*, Detroit, Michigan, 2007. SAE paper: 2007-01-0257.
- [30] S. Hounsham, R. Stobart, A. Cooke, and P. Childs. Energy Recovery Systems for Engines. In *SAE International*, Detroit, Michigan, 2008. SAE paper: 2008-01-0309.

- [31] H. Xie and C. Yang. Dynamic behavior of Rankine cycle system for waste heat recovery of heavy duty diesel engines under driving cycle. *Journal of Applied Energy*, 112:130–141, 2013.
- [32] F. Willems, F. Kupper, G. Rascanu, and E. Feru. Integrated Energy and Emission Management for Diesel Engines with Waste Heat Recovery Using Dynamic Models. *Oil Gas Sci. Technol. - Rev. IFP Energies nouvelles*, 70(1):143–158, 2014.
- [33] J. Peralez, P. Tona, O. Lepreux, A. Sciarretta, L. Voise, P. Dufour, and M. Nadri. Improving the Control Performance of an Organic Rankine Cycle System for Waste Heat Recovery from a Heavy-Duty Diesel Engine using a Model-Based Approach. In *52nd IEEE Conference on Decision and Control*, pages 6830–6836, Florence, Italy, 2013.
- [34] G. Hou, G. Hu, and J. Zhang. Supervisory Predictive Control of Evaporator in Organic Rankine Cycle (ORC) System for Waste Heat Recovery. In *2011 International Conference on Advanced Mechatronic Systems*, pages 306–311, Zhengzhou, China, 2011.
- [35] J. Zhang, Y. Zhou, H. Guolian, and F. Fang. Generalized predictive control applied in waste heat recovery power plants. *Journal of Applied Energy*, 102:320–326, 2013.
- [36] M. Wallace, B. Das, P. Mhaskar, J. House, and T. Salsbury. Offset-free model predictive control of a vapor compression cycle. *Journal of Process Control*, 22(7):1374–1386, 2012.
- [37] F. Willems and D. Foster. Integrated Powertrain Control to meet future CO₂ and Euro-6 emissions targets for a diesel hybrid with SCR-deNO_x system. In *Proceedings of the American Control Conference*, pages 3944–3949, St. Louis, MO, USA, 2009.
- [38] H. Langouët, L. Métivier, D. Sinoquet, and Q.H. Tran. Optimization for engine calibration. In *International Conference on Engineering Optimization*, pages 1–10, Rio de Janeiro, Brazil, 2008.
- [39] E. Feru, B. de Jager, F. Willems, and M. Steinbuch. Two-phase plate-fin heat exchanger modeling for waste heat recovery systems in diesel engines. *Journal of Applied Energy*, 133:183–196, 2014.
- [40] E. Feru, F. Willems, C. Rojer, B. de Jager, and M. Steinbuch. Heat Exchanger Modeling and Identification for Control of Waste Heat Recovery Systems in Diesel

- Engines. In *Proceedings of the American Control Conference*, pages 2860–2865, Washington DC, USA, 2013.
- [41] E. Feru, F. Willems, B. de Jager, and M. Steinbuch. Modeling and Control of a Parallel Waste Heat Recovery System for Euro-VI Heavy-Duty Diesel Engines. *Journal Energies*, 7(10):6571–6592, 2014.
- [42] E. Feru, F. Kupper, C. Rojer, X.L.J. Seykens, F. Scappin, F. Willems, J. Smits, B. de Jager, and M. Steinbuch. Experimental validation of a dynamic waste heat recovery system model for control purposes. In *SAE International*, Detroit, Michigan, 2013. SAE paper: 2013-01-1647.
- [43] E. Feru, F. Willems, G. Rascanu, B. de Jager, and M. Steinbuch. Control of Automotive Waste Heat Recovery Systems with Parallel Evaporators. In *FISITA*, Maastricht, The Netherlands, 2014. FISITA paper: F2014-CET-015.
- [44] E. Feru, F. Willems, B. de Jager, and M. Steinbuch. Control of a Waste Heat Recovery System with Decoupled Expander for Improved Diesel Engine Efficiency. In *Proceedings of the European Control Conference*, pages 148–153, Linz, Austria, 2015.
- [45] E. Feru, N. Murgovski, B. de Jager, and F. Willems. Supervisory control of a heavy-duty diesel engine with an electrified waste heat recovery system. *Submitted to Control Engineering Practice*, 2015.
- [46] S. Charles and D. Christopher. Review of organic Rankine cycles for internal combustion engine exhaust waste heat recovery. *Journal of Applied Thermal Engineering*, 51(1–2):711–722, 2013.
- [47] A. Schuster, S. Karellas, and R. Aumann. Efficiency optimization potential in supercritical Organic Rankine Cycles. *Energy*, 35(2):1033–1039, 2010.
- [48] W. Gao, J. Zhai, G. Li, Q. Bian, and L. Feng. Performance evaluation and experiment system for waste heat recovery of diesel engine. *Energy*, 55:226–235, 2013.
- [49] V. Dolz, R. Novella, A. Garcia, and J. Sanchez. HD Diesel engine equipped with a bottoming Rankine cycle as a waste heat recovery system. Part 1: Study and analysis of the waste heat energy. *Journal of Applied Thermal Engineering*, 36:269–278, 2012.

- [50] C.O. Katsanos, D.T. Hountalas, and E.G. Pariotis. Thermodynamic analysis of a Rankine cycle applied on a diesel truck engine using steam and organic medium. *Journal of Energy Conversion and Management*, 60:68–76, 2012.
- [51] D. Ziviani, A. Beyene, and M. Venturini. Advances and challenges in ORC systems modeling for low grade thermal energy recovery. *Journal of Applied Energy*, 121:79–95, 2014.
- [52] J. Zhang, W. Zhang, H. Guolian, and F. Fang. Dynamic modeling and multivariable control of organic Rankine cycles in waste heat utilizing processes. *Journal of Computers and Mathematics with Applications*, 64:908–921, 2012.
- [53] M. V. Pham, F. Plourde, and S. K. Doan. Large-Eddy Simulations of Staggered Parallel-Plate Fin Heat Exchangers: Effect of Reynolds Number on Flow Topology. *Journal of Numerical Heat Transfer, Part A: Applications*, 53(4):354–376, 2008.
- [54] VDI-Gesellschaft Verfahrenstechnik und Chemieingenieurwesen. *VDI Heat Atlas*. Springer, Berlin, Germany, 2010.
- [55] Thome, John R. *Engineering Data Book III*. Wolverine Tube, Inc., Lausanne, Switzerland, 2010.
- [56] S.M. Kim and I. Mudawar. Universal approach to predicting saturated flow boiling heat transfer in mini/micro-channels Part II. Two-phase heat transfer coefficient. *International Journal of Heat and Mass Transfer*, 64:1239–1256, 2013.
- [57] M. J. Bagajewicz and E. Cabrera. Data reconciliation in gas pipeline systems. *Journal of Ind. Eng. Chem. Res.*, 42(22):5596–5606, 2003.
- [58] Steven Heinz. Development of a Worldwide Harmonised Heavy-duty Engine Emissions Test Cycle. Technical Report TRANS/WP29/GRPE/2001/2, United Nations, April 2001.
- [59] K. Yang, H. Zhang, S. Song, J. Zhang, Y. Wu, Y. Zhang, H. Wang, Y. Chang, and C. Bei. Performance Analysis of the Vehicle Diesel Engine-ORC Combined System Based on a Screw Expander. *Energies*, 7(5):3400–3419, 2014.
- [60] G. Hou, S. Bi, M. Lin, J. Zhang, and J. Xu. Minimum variance control of organic Rankine cycle based waste heat recovery. *Journal of Energy Conversion and Management*, 86:576–586, 2014.

- [61] E. Feru, F. Willems, B. de Jager, and M. Steinbuch. Model Predictive Control of a Waste Heat Recovery System for Automotive Diesel Engines. In *System Theory, Control and Computing, 18th International Conference*, pages 658–663, Sinaia, Romania, 2014.
- [62] Lewis, F. *Optimal Estimation*. John Wiley & Sons, Inc., 1986.
- [63] M. Hatami, D.D. Ganji, and M. Gorji-Bandpy. A review of different heat exchangers designs for increasing the diesel exhaust waste heat recovery. *Journal of Renewable and Sustainable Energy Reviews*, 37:168–181, 2014.
- [64] F. Cataldo, R. Mastrullo, A.W. Mauro, and G.P. Vanoli. Fluid selection of Organic Rankine Cycle for low-temperature waste heat recovery based on thermal optimization. *Energy*, 72:159–167, 2010.
- [65] S.E. Lyshevski. Energy conversion and optimal energy management in dieselelectric drivetrains of hybrid-electric vehicles. *Energy Conversion and Management*, 41(1):13–24, 2000.
- [66] J.T.B.A. Kessels, F. Willems, W.J. Schoot, and P.P.J. van den Bosch. Integrated energy & emission management for hybrid electric truck with SCR aftertreatment. In *Vehicle Power and Propulsion Conference (VPPC)*, Lille, France, 2010.
- [67] T. Nüesch, M. Wang, P. Isenegger, C.H. Onder, R. Steiner, P. Macri-Lassus, and L. Guzzella. Optimal energy management for a diesel hybrid electric vehicle considering transient PM and quasi-static NOx emissions. *Control Engineering Practice*, 29:266–276, 2014.
- [68] Z. Filipi, H. Fathy, J. Hagen, A. Knaf, R. Ahlawat, J. Liu, D. Jung, D. Assanis, H. Peng, and J. Stein. Engine-in-the-Loop Testing for Evaluating Hybrid Propulsion Concepts and Transient Emissions - HMMWV Case Study. In *SAE International*, Detroit, Michigan, 2006. SAE paper: 2006-01-0443.
- [69] M. Grahn, K. Johansson, and T. McKelvey. Model-based diesel Engine Management System optimization for transient engine operation. *Control Engineering Practice*, 29:103–114, 2014.
- [70] P. Chen and J. Wang. Control-oriented model for integrated diesel engine and aftertreatment systems thermal management. *Control Engineering Practice*, 22:81–93, 2014.

- [71] F. Will. Fuel conservation and emission reduction through novel waste heat recovery for internal combustion engines. *Fuel*, 102:247–255, 2012.
- [72] F. Yang, X. Dong, H. Zhang, Z. Wang, K. Yang, J. Zhang, E. Wang, H. Liu, and G. Zhao. Performance analysis of waste heat recovery with a dual loop organic Rankine cycle (ORC) system for diesel engine under various operating conditions. *Energy Conversion and Management*, 80:243–255, 2014.
- [73] R. Cloudt, J. Saenen, E. Eijnden, and C. Rojer. Virtual Exhaust Line for Model-based Diesel Aftertreatment Development. In *SAE International*, Detroit, Michigan, 2010. SAE paper: 2010-01-0888.
- [74] B. de Jager, T. van Keulen, and J. Kessels. *Optimal Control of Hybrid Vehicles*. Springer-Verlag, London, 2013.
- [75] F. Willems and R. Cloudt. Experimental demonstration of a new model-based SCR control strategy for cleaner heavy-duty diesel engines. *IEEE Transactions on Control Systems Technology*, 19(5):1305–1313, 2011.
- [76] Bertsekas, D. *Dynamic programming and optimal control*. Athena Scientific, Belmont, 2007.
- [77] F. Willems, M.C.F. Donkers, and F. Kupper. *Optimization and Optimal Control in Automotive Systems*, chapter Optimal Control of Diesel Engines with Waste Heat Recovery System. Springer International Publishing, Switzerland, 2014.
- [78] R. Cloudt and F. Willems. Integrated emission management strategy for cost-optimal engine-aftertreatment operation. In *SAE International*, Detroit, Michigan, 2011. SAE journal: 2011-01-1310.
- [79] N. Murgovski, M. Grahn, L.M. Johannesson, and T. McKelvey. Automated engine calibration of hybrid electric vehicles. *IEEE Transactions on Control Systems Technology*, 23(3):1063–1074, 2015.
- [80] A. Sciarretta and L. Guzzella. Control of hybrid electric vehicles. *IEEE Control Systems*, 27(2):60–70, 2007.
- [81] P. Rutquist, C. Breitholtz, and T. Wik. On the infinite time solution to state-constrained stochastic optimal control problems. *Automatica*, 44(7):1800–1805, 2008.
- [82] L.C. To and M.O. Tadó and M. Kraetzl. *Robust Nonlinear Control of Industrial Evaporation Systems*. World Scientific, River Edge, New Jersey, 1999.

-
- [83] M. Herceg, M. Kvasnica, C.N. Jones, and M. Morari. Multi-Parametric Toolbox 3.0. In *Proc. of the European Control Conference*, pages 502–510, Zürich, Switzerland, July 17–19 2013.
- [84] D. Ambrose, C. H. S. Sprake, and R. Townsend. Thermodynamic Properties of Organic Oxygen Compounds. XXXVII. Vapour Pressures of Methanol, Ethanol, Pentan-1-ol, and Octan-1-ol from the Normal Boiling Temperature to the Critical Temperature. *Journal of Chemical Thermodynamics*, 7(2):185–190, 1975.

Summary

Auto-calibration for Efficient Diesel Engines with a Waste Heat Recovery System

Driven by CO₂ legislation, fuel costs, and concerns about energy security, the automotive industry is forced to develop highly efficient powertrains. In an internal combustion engine, approximately 60% of the fuel energy is lost through the coolant and exhaust. With a potential of 4-8% fuel consumption reduction, engine exhaust gas heat recovery is very promising, especially for long-haul truck applications. To recover the exhaust gas energy, a Waste Heat Recovery (WHR) system is used. The WHR system allows the conversion of the exhaust gas energy into mechanical power, which can be used for the engine drivetrain or to drive an electric generator. For heavy-duty applications, one of the most attractive technology for heat recovery is based on the Organic Rankine Cycle (ORC) due to the low temperature heat sources. To optimize the efficiency of the WHR system, and to cope with engine-out emissions imposed by legislation, a control design is necessary. Control of truck engines with WHR system is challenging. This is due to the highly dynamic engine conditions, to coupling between engine-WHR system, and to safety and emission constraints. The objective of this thesis is to optimize the performance of a diesel engine with a WHR system, subject to emission constraints. The powertrain performance is quantified in terms of fuel and AdBlue consumption. To this end, an optimization strategy that adapts the engine settings on-line (auto-calibration) is adopted.

This research resulted in the following main developments.

The first new development is in the area of modular plate-fin heat exchanger modeling. The heat exchanger is a key component within the WHR system, contributing the most to the overall system dynamic behavior. The heat exchanger model is developed based on a procedure that combines the finite difference modeling approach with a moving

boundary one. We show that this is a suitable solution to capture multiple phase transitions along a single pipe flow, which are very likely to occur in a modular heat exchanger. The model is validated on a highly dynamic World Harmonized Transient Cycle, which is representative for real driving conditions. As a result, the model can be used for prediction, for real-time implementation as well as for control design.

The second new development concerns the modeling and validation of a complete WHR system for a heavy-duty truck engine. The considered WHR system consists of two parallel evaporators with expander and pumps mechanically coupled to the engine crankshaft. The complete WHR system is modeled component by component and validated on a wide range of engine operating conditions. Over a dynamic cycle, the maximum prediction error is as follows: 4% for the working heat flow rate, 7% for the mass flow rate, 3% for the WHR system pressure and 13% for the working fluid temperature.

Furthermore, a linear model predictive control (MPC) strategy is designed. To benchmark the MPC strategy performance, a classical proportional-integral (PI) strategy is used. Due to the nonlinear system behavior, a switching control strategy is adopted based on three representative engine operating points. The performance of both control strategies is verified on a World Harmonized Transient Cycle. The linear MPC strategy provides up to 15% more energy recovery potential as compared to the PI control strategy. The system performance can be furthermore improved using a nonlinear MPC. However, the computational complexity of a nonlinear MPC strategy is significant, which may not be suitable for real-time implementation.

The third development addresses the control of a WHR system with expander decoupled from the engine crankshaft. By making the expander speed variable, the system can be operated at a higher pressure, which increases the WHR system output power by a maximum of 29%. This design requires additional components, such as a generator and power electronics. However, the advantage is that the generated power can now be stored in a battery for latter usage. This increases the flexibility for WHR system power manipulation. Furthermore, the proposed WHR system design can be easily fitted in a hybrid electric vehicle architecture.

Finally, the optimal control problem of a diesel engine is extended for a powertrain with an electrically assisted WHR system. To this end, an integrated energy and emission management strategy is presented. This strategy optimizes the engine setting, by minimizing the operational cost associated with fuel and AdBlue consumption, while satisfying the tailpipe emission constraints set by the legislation. We demonstrate the potential of the integrated energy and emission management strategy on both the cold-

start and the hot-start World Harmonized Transient Cycle. For various powertrain configurations, engine with and without WHR system, the effect of the battery is studied. Within the NO_x emission limit, the electrified WHR system with battery shows the best performance, reducing the CO₂ emissions by 3.5% as compared to the Euro-VI baseline strategy.

Acknowledgements

I would like to express my sincere gratitude to many people who contributed and gave me the opportunity to write this thesis. First, I am extremely grateful to my first copromotor dr.ir. Frank Willems. Thank you for your assistance and suggestions throughout my project. Without your view on my work, valuable comments and support, this thesis would have not been possible. I need to thank you not only from a technical but also from a personal point of view. You helped me and encouraged me whenever I had difficulties, which I will never forget. Second, I would like to thank to my second copromotor dr.ir. Bram de Jager for the valuable remarks, critical view, explanations and advises in my work. Thank you for your availability and for hosting most of the meetings in your office. I really enjoyed the discussions with you and Frank, on the project but also on different subjects. Third, I am very grateful to my promotor prof.dr.ir. Maarten Steinbuch for his support, encouragement and understanding. Your positive thinking, inspiration and enthusiasm have been always boosting my motivation.

I would like to thank to all the members of the committee, prof.dr.ir. David Smeulders, prof.dr.ir. Luigi del Re, prof.dr. Philip de Goey, dr.ir. Vincent Lemort and prof.dr.ir. Zoran Filipi, for reading the thesis and providing interesting suggestions. Moreover, I want to acknowledge dr.ir. Rick de Lange and dr.ir. Henk Ouwerkerk for the interesting discussions on a more practical level regarding the Waste Heat Recovery system setup. Furthermore, I want to thank to Nikolce Murgovski and Tijs Donkers for the helpful discussions on integrated powertrain control strategy.

I am grateful to TNO Automotive for the financial support of my project. I want to thank to numerous people from TNO Automotive, Chepa Rojer, Erik Dosje, Fabio Scappin, Frank Kupper, Robbert Jan and Xander Seykens, for the help and discussions on the Waste Heat Recovery system modeling, validation and experimental measurements. Furthermore, I would like to thank to Andreea Balau, Armando Indrajana, Bogdan Rosca, Frank Engels, Paul Mentink and all the people who made

every Tuesday an enjoyable day at TNO. I will continue enjoying the time with you also as a new colleague. I would also like to thank to Jeroen Smits from DAF who verified and approved most of the papers before publication.

I would like to specially thank to Mircea Lazar for guiding me during my Master's project and being a large part of the reason for me to start a PhD. Furthermore, I want to thank for your suggestions and assistance together with Veaceslav Spinu, on the European Control Conference student competition.

I want to thank to my BSc students Michiel Oom, Roy Reinders, Ruud Salama and Sjoerd Koopmans and MSc student George Rascanu for their effort and contributions.

Thanks to my office mates Behnam Assadi, Xi Luo, Victor Dolk, Nick Bauer, Menno Lauret and Chris Criens for the very nice time spent together inside but also outside the office. Special thanks to Sava Marinkov and Emilia Silvas, for the interesting conversations, laughs and great times. Thanks to Matthijs van Berkel, Tom Gommans, Niek Borgers, Duarte Antunes, Joost Bolder, Cesar Lopez Martinez, Robert Voorhoeve and to all of my TU/e colleagues, for the very enjoyable days at work. Last but not least, I would like to thank also to our secretaries Petra Aspers and Geertje Janssen for the administrative work and for organizing very nice events.

Pe această cale vreau să mulțumesc în special familiei mele, tăticu, mămica și Emilia. Ați fost lângă mine și m-ați susținut de fiecare dată când aveam nevoie. Dacă mă întorceam acasa, dacă plecam, voi erați mereu acolo... pentru mine. Vă mulțumesc pentru că mi-ați fost alături, datorită vouă am ajuns și sunt ce vedeți acum. Sper cândva să vă pot oferi măcar o parte din ce mi-ați oferit voi pentru mine. Vă mulțumesc pentru că existați.

În final, vreau să mulțumesc viitoarei mele soții Cristina. Ai apărut în viața mea când nu mă așteptam, dar când aveam cel mai mult nevoie de tine. Am găsit la tine liniștea, dragostea și încrederea de care aveam nevoie. Îți mulțumesc.

Emanuel Feru
September 2015

Curriculum Vitae



Emanuel Feru was born on December 27, 1986 in Onești, Romania.

He received his Bachelor of Science and Master of Science degrees (graduated with First Class Honors) from the Faculty of Computer Science and Automatic Control at the Gheorghe Asachi University of Iasi, Romania, in 2009 and 2011, respectively. During his Master of Science study, he worked as an intern at Continental Automotive Romania SRL and served as laboratory assistant for the Automatic Control discipline. During the last five months of his Master of Science study, he visited the Eindhoven University of Technology, The Netherlands, to carry out his master project.

In September 2011 he started his PhD project within the Control Systems Technology group of the department of Mechanical Engineering at the Eindhoven University of Technology, The Netherlands, under the guidance of Maarten Steinbuch, Frank Willems, and Bram de Jager. His research project was financially supported by TNO Automotive, The Netherlands. The results of his research are presented in this thesis.

In July 2015, he won the European Control Conference (ECC) 2015 Student Competition award with the paper "*Towards Constrained Optimal Control of Spark Ignition Engines*".

From August 2015, he works as a Research Scientist at TNO Automotive, Powertrains group in Helmond, The Netherlands.

